MECHANICAL PROPERTIES OF NON-CRIMP FABRIC (NCF) FIBERGLASS REINFORCED COMPOSITE MATERIALS MANUFACTURED BY USING VACUUM INFUSION PROCESS

by

Serkan Çalışkan

B.S., in M.E., Boğaziçi University, 2003

Submitted to the Institute for Graduate Studies in
Science and Engineering in partial fulfillment of
the requirements for the degree of
Master of Science

Graduate Program in Mechanical Engineering
Boğaziçi University

2009

ACKNOWLEDGEMENTS

Firstly, I would like to express my gratitude to my advisor, Assist. Prof. Nuri Ersoy for all his support, patience and encouragement during the completion of my thesis.

Besides, I would also like to acknowledge the helps of Osman Ersoy from Arçelik Çayırova facility and Kenan Çınar, PhD student at Boğaziçi University.

Last but not least, no words would suffice to express my appreciation for the love and support provided by my family without whom this thesis could not have been finished.

ABSTRACT

MECHANICAL PROPERTIES OF NON-CRIMP FABRIC (NCF) FIBERGLASS REINFORCED COMPOSITE MATERIALS MANUFACTURED BY USING VACUUM INFUSION PROCESS

Non-crimp fabric (NCF) fiber reinforced composite materials that are composed of textile preforms consisting of multiaxial layers of straight fiber bundles with different orientations stitched together by knitting yarns, manufactured by using vacuum infusion process (VIP) have recently gained attraction in primary engineering applications as they offer large potential for aerospace, marine and automotive industries due to their excellent performance and relatively low production cost.

In this study, mechanical properties of NCF composites made from polyester resin and fiberglass reinforcement that have distinct fiber orientations, fiber volume fractions and stacking sequences are assessed by mechanical tension testing where a total of 75 specimens are subjected to tests.

Besides, theoretical predictions for the engineering strengths, stiffnesses and strains of the manufactured laminates are obtained through micromechanics and classical lamination theory (CLT), these results are compared with corresponding experimental data. Possible causes of discrepancies between experimental data and theoretically predicted data are also discussed.

ÖZET

VAKUM İNFÜZYON İŞLEMİ KULLANILARAK ÜRETİLEN KIVRIMSIZ CAM ELYAFI TAKVİYELİ KOMPOZİT MALZEMELERİN MEKANİK ÖZELLİKLERİ

Örme iplikleriyle dikilmiş farklı yönlerdeki düz elyaf bağlarından oluşan çok eksenli dokuma önyapılarını içeren, vakum infüzyon işlemi kullanılarak üretilen kıvrımsız elyaf takviyeli kompozit malzemeler, üstün performansları ve göreceli olarak ucuz üretim maliyetleri sayesinde havacılık ve uzay, deniz taşıtları ve otomotiv endüstrileri gibi başlıca mühendislik uygulamalarında kullanılmaya başlanmıştır.

Bu çalışmada, farklı elyaf yönü, elyaf hacim oranı ve istif dizilişleri içeren ve takviye olarak cam elyafı, reçine olarak polyester kullanılmış kıvrımsız kompozit malzemeler çekme testine tabi tutulmuş ve bu malzemelerin mekanik özellikleri değerlendirilmiştir. Deneyler esnasında toplam olarak 75 numune test edilmiştir.

Ek olarak, üretilmiş plakaların dayanım, rijitlik ve uzamaları, mikromekanik ve klasik laminasyon teorisi (CLT) yardımıyla, teorik olarak hesaplanmış, elde edilen değerler deneysel değerlerle kıyaslanmış ve aradaki farkların olası nedenleri irdelenmiştir.

TABLE OF CONTENTS

LIST OF FIGURES

LIST OF TABLES

LIST OF SYMBOLS/ABBREVIATIONS

A	Extensional stiffness matrix
A'	Inverse of extensional stiffness matrix
$A^{(n)}$	Modified extensional stiffness matrix
A_{ij}	Components of extensional stiffness matrix
B	Bending-extension coupling stiffness matrix
B_{ij}	Components of bending-extension coupling stiffness matrix
$B^{(n)}$	Modified bending-extension coupling stiffness matrix
D	Bending stiffness matrix
D_{ij}	Components of bending stiffness stiffness matrix
$D^{(n)}$	Modified bending stiffness matrix
d_f	Fiber density
d_m	Matrix density
d_s	Specimen density
E_f	Fiber modulus
E_m	Matrix modulus
E_k	Knee point elastic modulus
E_u	Young's modulus after knee point till breakage
E_x	Composite longitudinal modulus
E_y	Composite transverse modulus
F	Strain concentration factor
F_u	Predicted ultimate load
G_f	Fiber shear modulus
G_m	Matrix shear modulus
G_{xy}	Composite shear modulus
M	Moment vector
m_c	Crucible mass
m_{cf}	Crucible mass with fibers after burnoff
m_f	Fibers' mass
m_m	Matrix mass
m_s	Specimen mass

M_x	Moment per unit length
N	In-plane forces vector
n	Number of layers of the repeating sequence in each side with respect to the middle surface
N_x	Force per unit length
Q_{ij}	Components of the lamina stiffness matrix
$\overline{Q}_{ij}$	Components of the transformed lamina stiffness matrix
s	Symmetric
t	Thickness
u	Displacement in x direction
u^o	Middle surfaces tangential displacement along the x-direction
v	Displacement in y direction
v^o	Middle surfaces tangential displacement along the y-direction
V_f	Volume fraction per cent of fibers
V_f^{-45}	Fiber volume fraction of laminae containing -45^o fibers
V_f^{+45}	Fiber volume fraction of laminae containing +45^o fibers
V_f^{0}	Fiber volume fraction of laminae containing 0^o fibers
V_f^{90}	Fiber volume fraction of laminae containing 90^o fibers
V_m	Volume fraction per cent of matrix
V_v	Volume fraction per cent of void
V_s	Specimen volume
w	Displacement in z direction
w	Width

γ_{xy}	Shear strain along x-y directions
γ_{xz}	Shear strain along x-z directions
γ_{yz}	Shear strain along y-z directions
γ^o_{xy}	Middle surface shear strain along x-y directions
ε_{fl}	Failure strain in uniaxial tension of the fiber
ε_k	Knee tensile strain
ε_L	Ultimate longitudinal strain
ε_{LT}	Ultimate shear strain
ε_m	Failure strain in uniaxial tension of the matrix

ε_T	Ultimate transverse strain
ε_u	Ultimate tensile strain
ε_x	Strain along *x* direction
ε^o_x	Middle surface strain along *x* direction
ε_y	Strain along *y* direction
ε^o_y	Middle surface strain along *y* direction
θ	Lamina orientation angle
κ_x	Bending curvature for bending of the middle surface *xz*
κ_y	Bending curvature for bending of the middle surface *yz*
κ_{xy}	Out-of-plane twisting curvature for the middle surface
ν_{xy}	Poisson's ratio for *x*-*y* directions
ν_f	Fiber Poisson's ratio
ν_f	Matrix Poisson's ratio
ξ	A measure of fiber reinforcement
σ_1	Transformed longitudinal strength
σ_2	Transformed transverse strength
σ_{fl}	Ultimate longitudinal strength of fibers
σ_k	Knee tensile stress
σ_L	Ultimate longitudinal strength of lamina
σ_m	Ultimate strength of the matrix
σ_{mf}	Strength of the matrix corresponding to ε_{fl}
σ_T	The predicted transverse strength
σ_u	Ultimate tensile stress
σ_x	Uniaxial tensile stress
σ_x	Uniaxial transverse stress
τ_{12}	Transformed shear strength
τ_{LT}	Predicted shear strength
τ_m	Matrix shear strength
τ_{xy}	Shear stress along *x*-*y* directions
τ_{xz}	Shear stress along *x*-*z* directions
τ_{yz}	Shear stress along *y*-*z* directions

CLT	Classical lamination theory
CV	Coefficient of variation
DCBD	1,4-dichloro-2,3-butanediol
FE	Finite elements
MEKP	Methyl ethyl ketone peroxide
NCF	Non-crimp fabric
PEEK	Polyetheretherketone
PET	Polyethylene terephthalate
PI	Polyimide
PPS	Polyphenylene sulfide
PS	Polysulfone
RIFT	Resin injection under flexible tooling
RTM	Resin transfer moulding
RVE	Representative volume element
SCRIMP	Seemann composites resin infusion moulding process
SD	Standard Deviation
UDPT	Unidirectional pre-preg laminate
VARI	Vacuum assisted resin injection
VARTM	Vacuum assisted resin transfer moulding
VBRTM	Vacuum bag resin transfer moulding
VIP	Vacuum infusion process
WF	Woven fabric

1. INTRODUCTION

In this chapter, composite materials, their classification, manufacturing methods and application areas are discussed with a focus on non-crimp fabric (NCF) fiber reinforced plastic composite materials which are in the main scope of this work.

1.1. Composite Materials

Structural materials are mainly divided into four basic categories: metals, polymers, ceramics and composites. Composites, which consist of two or more separate materials combined in a macroscopic structural unit to yield a beneficial third material, are made from various combinations of the other three type of materials [1].

There are some main points in a definition of an acceptable composite material for use in structural applications:

- The structural unit is formed at the macroscopic level rather than at the microscopic level
- The resultant material is distinguished by the naked eye [2].
- It consists of two or more physically distinct and separable materials.
- It can be made by mixing the separate materials in such a way that the dispersion of one material in the other can be done in a controlled way to achieve optimum properties.
- The properties are superior, and possibly unique in some specific respects, to the properties of the individual components [3].

Consequently, many man-made materials that have two or more constituents such as metallic alloys and polymer blends are usually not classified as composite materials.

Composite materials have the advantage over other aforesaid materials that when designed well, they usually exhibit the best qualities of their components or constituents, and often some qualities that neither constituent originally possess. Some of the properties that can be improved by forming a composite material are strength, stiffness, strength-to-density ratio, stiffness-to-density ratio, corrosion resistance, wear resistance, attractiveness, weight, fatigue life, temperature-dependent behavior, thermal insulation, thermal conductivity and acoustical insulation while keeping fabrication and assembly costs less than those of ordinary materials [2].

1.2. Classification of Composite Materials

There are four commonly accepted types of composite materials which are the following: fibrous composite materials that consist of fibers in a matrix, laminated composite materials that consist of various materials, particulate composite materials that are composed of particles in a matrix, combinations of some or all of the first three types. Only fibrous type of composite materials will be explained thoroughly because this type of composites is the main focus of this study.

1.2.1. Fibrous Composite Materials

Long fibers in various forms are inherently much stiffer and stronger compared to the same material in bulk form. For instance, ordinary glass have tensile strength of 0.02 GPa whereas fiberglass have tensile strength of 2.8 GPa to 4.0 GPa. In commercially available forms or laboratory-prepared forms, the tensile strength reaches up to 7.0 GPa [2]. Therefore, the geometry and physical makeup of a fiber are somewhat crucial to the evaluation of its strength and need to be taken into consideration in structural applications. Furthermore, the reason why fibers have different properties from the bulk form is due to the more perfect structure of a fiber. In fibers, the crystals are aligned along the fiber axis. Moreover, there are fewer internal defects in fibers than in bulk material, e.g., fiber form is the least dislocation containing structure in materials having dislocations.

To form the fibrous composite, the fibers are embedded in a matrix material which binds the fibers together, transfer load to the fibers and protect them from environmental

attack and damage due to handling. Reinforcement in form of fibers can be arranged in a number of ways both in the form of bundles or homogenously dispersed fibers depending on the application of the final composite material [4].

Traditional pre-preg (pre-impregnated) 2D-fiber reinforced polymer composites have been used in the industries like marine, aircraft and automobile for many years for reasons such as their excellent stiffness-to-density ratio and resistance to corrosion. Pre-preg laminates give excellent in-plane mechanical properties in terms of stiffness and strength due to well-aligned fibers with high volume fraction in the composite. However, they have the disadvantages that their post-impact mechanical properties are severely degraded due to their poor interlaminar fracture toughness and they have high costs associated with their manufacturing techniques.

The drawbacks found in pre-preg laminates can be avoided by using some other type of reinforcement such as woven preforms. This reinforcement type is produced by the weaving of fiber bundles into a blanket which creates reinforcement with bidirectional orientation. The main driving force for the development of woven reinforcement is the reduced manufacturing costs and its enhanced fracture toughness compared to pre-preg composites. The reduction in manufacturing cost is related to a decrease in both labour and material cost. However, since waviness in the out-of plane direction is introduced in the fiber bundles in the manufacturing stage, the in-plane material properties of woven composites become inferior to the properties found in pre-preg composites.

The shortcomings associated with both the pre-pregs and the woven composites calls for new types of reinforcements which combine the excellent in-plane properties of pre-preg composites with the relatively good fracture toughness properties and lower manufacturing costs found in woven composites. One relatively new type of reinforcement, which has the possibility to combine the benefits found in both types of reinforcements, is the non-crimp fabric (NCF).

As can be seen in Figure 1.1, the internal structure of these three reinforcement types differs quite significantly. Figure 1.1 (a) shows an example of the internal structure of a cross-ply pre-preg laminate which has an internal structure consisting of homogenously

dispersed fibers in layers with a certain orientation. Figure 1.1 (b) shows an example of the internal structure of a woven preform. The bundles out-of plane orientation introduced in the interlaced regions between two bundles with different orientation are dependent on the weaving pattern. A number of blankets with various orientations are normally stacked together in a mould to meet the design criteria in terms of mechanical properties before consolidation into the final composite.

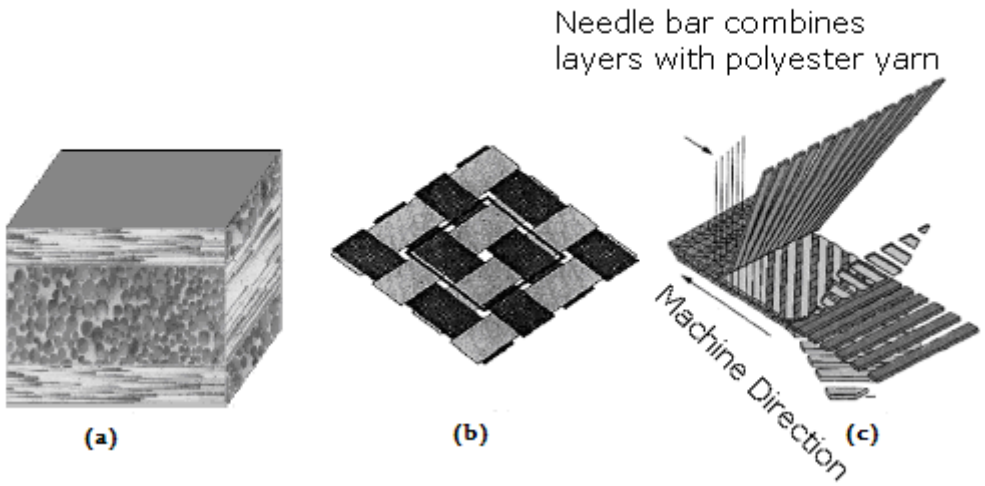

Figure 1.1. Internal structure of (a) pre-preg cross-ply laminate, (b) woven preform and (c) schematic picture of the non-crimp fabric perform [4].

A schematic figure over the internal structure of a NCF reinforcement is displayed in Figure 1.1 (c) and it can be observed that this material represents a combination of the two reinforcement types previously described. In this case, the fibers in each layer are gathered in bundles with a well-defined geometry in a fashion which is very similar to that for the woven composites. However, in this case the bundles are kept together by a knitting yarn instead of weaving the bundles together as described for the woven composites which theoretically should produce a fabric without out-of plane waviness in the fiber bundles. This manufacturing technique creates a dry fabric which is easily formed into complicated shapes before it is consolidated into the final composite.

1.2.1.1. Properties of Fibers. A fiber is characterized geometrically not only by its very high length-to-diameter ratio but also its near-crystal-sized diameter. Strengths and modulus of some selected fiber materials along with a few common structural metallic

elements are listed in Table 1.1. A direct comparison between fibers and structural metals is not valid because fibers need to have a surrounding matrix to perform in a structural member while structural metals are ready-to-use. Densities are also tabulated in Table 1.1 since the strength-to-density and stiffness-to-density ratios are commonly used as indicators of effectiveness of a fiber, especially in applications sensitive to weight such as spaceships. Properties of glass fibers will be discussed in more detail as they are the type of fibers used in this study.

Table 1.1. Properties of selected fibers and bulk metals [1], [2] and [3]

Material	Density (g/cm^3)	Poisson's Ratio	Tensile Strength (MPa)	Tensile Modulus (GPa)
Aluminium	2.80	0,33	310	69
Titanium	4.61	0,33	1900	115
Steel	7.83	0,27 – 0,3	1034	200
E-glass fibers	2.56	0,22	1900 – 3400	72
S-glass fibers	2.49	0,24	4482	86
PAN based Carbon type I	1.95	0,20	2200	390
PAN based Carbon type II	1.75	0,20	2700	250
Kevlar 29	1.44	0,34	3792	62
Kevlar 49	1.47	0,31	3792	131
Beryllium	1.82	0,28	1700	300
Boron	2.52	0,21	3400	400
Copper	8,92	0,34	220	120
Silicon Carbide	3.04	0,18	3448	427

1.2.1.2. Glass Fibers. Glass fibers/fiberglasses (both are used interchangeably) consist primarily of silica (silicon dioxide) and metallic oxide-modifying elements. These glasses are usually amorphous although some crystallisation may occur after prolonged heating at

high temperatures. This generally leads to a reduction in strength properties [1], [3]. E-glass (named for its electrical properties) is the most commonly used glass because it draws well and has good strength, stiffness, electrical and weathering properties. C-glass (C for corrosion) has a higher resistance to chemical corrosion than E glass but is more expensive and has lower strength properties. S-glass (S for high-strength) is the most expensive of all with higher Young's modulus and is more temperature resistant. It is used in special applications such as the aircraft industry where the higher modulus may justify the extra cost. Fiberglass/epoxy and fiberglass/polyester composites are used extensively in applications ranging from fishing rods to storage tanks and aircraft parts.

The strength and modulus of glass are determined primarily by the three-dimensional structure of the constituent oxides. Figure 1.2 shows a two-dimensional representation of the three-dimensional network of linked polyhedron units in a simple sodium silicate glass. Each polyhedron is a combination of oxygen atoms around a silicon atom and they are bonded to each other by strong covalent bonds. The sodium ions form ionic bonds with oxygen atoms and are not linked directly to the network.

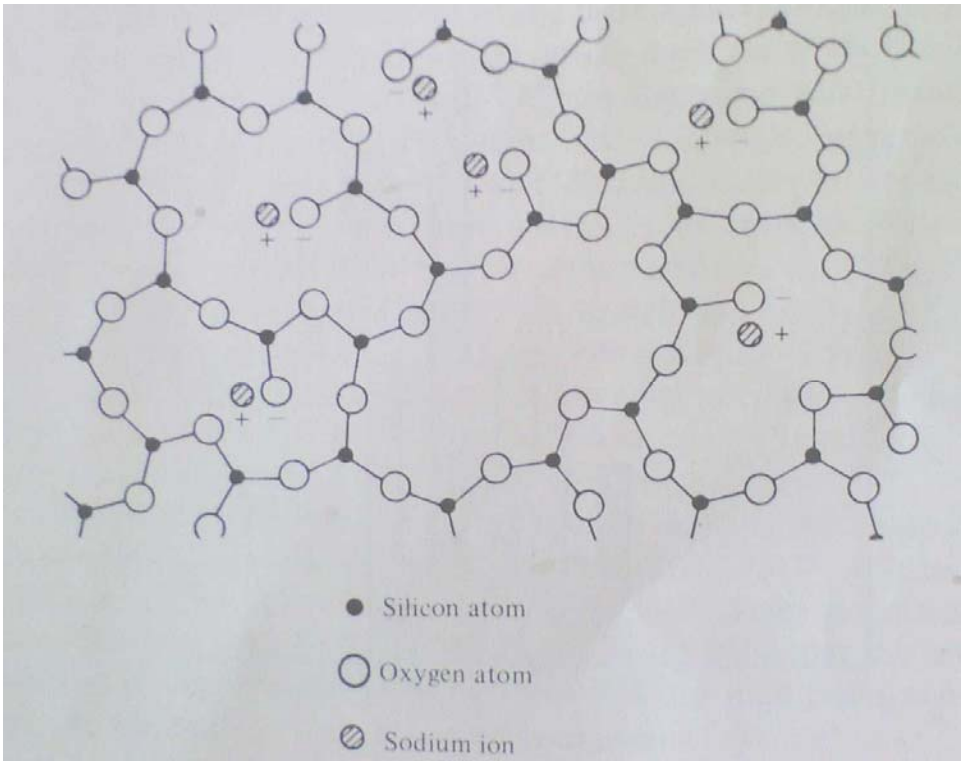

Figure 1.2. Two-dimensional representation of the polyhedron network structure of sodium silicate glass. [3]

1.2.1.3. Properties Of Matrix Materials. Naturally, fibers are of little use unless they are bonded together to take the form of a structural element that can carry loads. The binder material is usually called the matrix (or resin). The purpose of the matrix is manifold; support the fibers, protection of the fibers, stress transfer between broken fibers, in many cases contribute some needed property such as ductility, toughness, or electrical insulation, etc. [1], [2], [3]. Typically, the matrix is of considerably lower density, stiffness, and strength than the fibers. However, the combination of fibers and a matrix can have very high strength and stiffness, yet still have low density. Matrix materials can be polymers, metals, ceramics or carbon where the cost of each matrix escalates in that order as does the temperature resistance.

Polymers (poly - many and mer - unit or molecule) are the most widely used matrix materials in modern composites. They exist in at least three major forms: linear, branched, or cross-linked. A linear polymer is merely a chain of mers. A branched polymer consists of a primary chain of mers with other chains that are attached in three dimensions just like three branches as shown in Figure 1.3. Finally, a cross-linked polymer has a large number of three-dimensional highly interconnected chains as in figure. Linear polymers have the least strength and stiffness, whereas cross-linked polymers have the most because of their inherently stiffer and stronger structure.

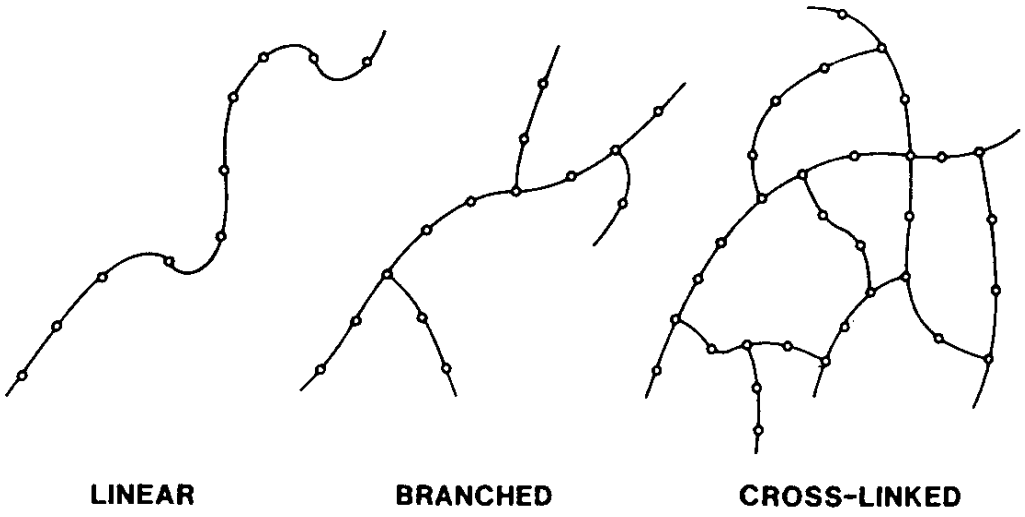

Figure 1.3. Polymer structures [2]

There are mainly three classes of structural polymers:

- Rubbers are cross-linked polymers that have a semicrystalline state well below room temperature but act as rubber above room temperature. Thus, they are not used as matrix materials in composites.

- Thermoplastics are made up of linear molecular chains. They derive their strength from the high concentration of molecular entanglements. When thermoplastics are heated, disentanglement and a change from a rigid solid to a viscous liquid occur. Thermoplastics have anisotropic properties depending on the conditions during solidification. They derive strength and stiffness from the inherent properties of the monomer units and the very high molecular weight. Examples of thermoplastics that are used in composites are polyimide (PI), polysulfone (PS), polyetheretherketone (PEEK), polyphenylene sulfide (PPS).

- In thermosetting polymers, the liquid resins are converted into hard brittle solids by chemical cross-linking which leads to the formation of a tightly bound three-dimensional network of polymer chains. The mechanical properties depend on the molecular units making up the network and on the length and the density of the cross-links. Curing primarily refers to the process of solidification of polymer matrix materials. In thermoset-matrix composites, heat is usually added as a catalyst to speed up the natural chemical reaction of polymerization. Polymers are often added chemical catalysts (hardeners) in order for the matrix to get hardened faster [2]. Curing can be achieved at room temperature as well as higher temperatures to achieve optimum cross-linking and hence optimum properties. A relatively high temperature final post-cure treatment is often given to minimize any further cure and change in properties during service

The properties of the cured resins can be determined from specimens prepared by casting the uncured resin into moulds. A set of typical properties of epoxy and polyester resins is given in Table 1.2. Thermosetting resins are usually isotropic. Their most characteristic property is in response to heat since, unlike thermoplastics, they do not melt on heating. However, they lose their stiffness properties at the heat distortion temperature

and this defines an effective upper limit for their use in structural components. Epoxy resins are generally superior to polyester resins in this respect. Furthermore, epoxy resins have superior strength and elastic properties with a lower shrinkage on curing and a lower coefficient of thermal expansion. The strength of the interface bond between resin and fiber is also higher for epoxy resins. However, they have the disadvantage of a higher viscosity before curing and they are more expensive.

Table 1.2. Comparison of typical properties of epoxy and polyester resins [5]

Property	Units	Epoxy	Polyester
Density	g/cm^3	1.1 – 1.4	1.2 – 1.5
Young's modulus	GPa	3 – 6	2 – 4.5
Poisson's ratio		0.38 – 0.4	0.37 – 0.39
Tensile strength	MPa	35 – 100	40 - 90
Compressive strength	MPa	100 – 200	90 – 250
Elongation to break (tensile)	%	1 – 6	2
Thermal conductivity	$W\ m^{-1}\ ^oC$	0.1	0.2
Coefficient of thermal expansion	$10^{-6}\ ^oC^{-1}$	60	100 – 200
Heat distortion temperature	^oC	50 – 300	50 – 100

1.3. Manufacturing of Fiber Reinforced Composite Materials

There are mainly two types of manufacturing of fiber reinforced composite materials: open mould processes and closed mould processes. Open mould processes contain hand lay-up, spray-up, vacuum bag, pressure bag, autoclave, filament winding, centrifugal casting. Closed mould processes contain hot press moulding, compression moulding, injection moulding, transfer moulding, pultrusion, cold press moulding, reinforced reaction injection moulding, resin injection (resin transfer moulding) and finally vacuum infusion

process which is the technique used in this work and will be explained in more detail. Fabrication processes and their applicability to various types of fiber reinforcement are shown in Table 1.3.

Table 1.3. Fabrication processes for polymer matrix composites [1], [3]

Process	Type of fiber reinforcement			
	Continuous	Chopped	Woven/NCF	Hybrid
Hand lay-up		x	x	
Spray-up		x		
Vacuum bag / autoclave	x		x	
Filament winding	x			
Centrifugal casting	x			
Compression moulding	x	x	x	x
Injection moulding	x	x	x	x
Pultrusion	x		x	
Cold press moulding	x	x	x	x
Resin transfer moulding	x	x	x	x
RRIM		x		

1.4. Structural Applications of Composite Materials

There has been a rapid growth in the use of fiber reinforced materials in engineering applications recently such as marine and aircraft industry, and there is sufficient evidence that this will continue. This swift change has been achieved mainly by the substitution of traditional materials, primarily metals materials by composite materials due to their superior specific modulus (the modulus per unit weight) and specific strength (strength per unit weight) compared to those of metals, hence resulting in lighter and less expensive final products.

Composite structural elements are currently used in a variety of components for automotive, aerospace, marine, architectural, chemical and electrical structures in addition to consumer products such as skis, golf clubs, surf boards and tennis rackets [1], [3], [4].

Table 1.4 lists general applications for fiber reinforced composite materials based on plastics.

Table 1.4. Applications of fiber reinforced composite materials [3]

Industry	Examples
Aircraft	Wings, fuselages, landing gear, helicopter blades
Automobile	Body parts, lamp-housings, front-end panels, bumpers, leaf springs, seat housings, drive shafts
Boat	Hulls, decks, masts
Chemical	Pipes, tanks, pressure vessels
Furniture and equipment	Panels, housings, chairs, tables, ladders
Electrical	Panels, switchgear, insulators
Sport	Fishing rods, golf clubs, swimming pools, skis, canoes
Buildings	Seismic retrofitting of reinforced concrete buildings

1.5. NCF Fiber Reinforced Composites

The exploitation of traditional textile technology to organize high performance fibers for composite materials applications has provided a route to combining highly tailored materials with enhanced processability. Braiding, weaving and knitting technologies have allowed fibers to be arranged locally in optimized configurations and globally into preforms for conversion processes such as resin transfer moulding and pultrusion.

Although weaving has been utilized for some considerable time to produce high performance fabrics, this process has the disadvantage of introducing a degree of fiber crimp, thereby reducing the in-plane properties of a composite compared with the optimum for a composite with straight fibers (nominally represented by laminates produced via a pre-preg process). Furthermore, laminates produced from woven fabrics still suffer to a large extent from the problem of weak interlaminar strengths due to the absence of reinforcement in the out-of-plane direction. Various alternative textile processes such as 3D braiding and knitting can introduce reinforcement in the out-of-plane direction but this

is usually at the expense of in-plane properties. A small number of fibers in the through-thickness direction can raise the interlaminar toughness considerably and there have been some attempts made to introduce such reinforcement via stitching together of woven fabric layers. This can, however, damage the fabric locally and may lead to local strength losses in-plane.

A textile process that is now available has the potential to overcome both deficiencies of woven fabric without introducing any apparent additional property reductions. NCFs are a relatively new class of textiles in which a fabric is constructed of layers of tow aligned in specific directions. The layers of fibers are produced by laying tows next to each other in a specified direction and subsequently employing a secondary fine yarn knitted around the tows to hold the fabric in place. In its simplest form for use in composite reinforcement, the fiber tows could be glass and the knitting yarn a fine thermoplastic polyester [6].

NCF composites can trace their early steps to the marine industry and it was first manufactured in 1983 in terms of a +45° ply knitted together with a -45° ply to form a double bias fabric [4]. Since then, they have been regarded as one of the most promising next generation composite materials for they offer large potential for application in primary structures while yielding excellent performance at low production costs [7].

In a previous study which was conducted on finding out comparison of production costs of traditional pre-preg type composites and NCF composites making use of a rectangular plate, for pre-preg composite materials manufactured with autoclave technique it was shown that labour costs are responsible for almost half of the final cost of which material cost is 25 per cent. Labour cost contains mainly the continuous debulking and laying down the material, which can be curtailed in large amounts by converting to NCFs and resin transfer technique. On the other hand, since one layer in the NCF composite corresponds to approximately 7 pre-preg layers, deposition rates are much higher in the NCF composites compared to pre-preg composites. Finally, conclusion was that NCF composite production requires nearly 35 per cent less final cost than pre-preg types [8].

1.5.1. Production of NCF Fiber Preforms

The preforms are made from layers of non-crimped fiber tows stacked in the desired orientation and bounded together by a warp-knitting procedure in which the binder yarns are inserted through the thickness of the perform. A schematic figure of the production of NCF performs with Liba system is presented in Figure 1.4.

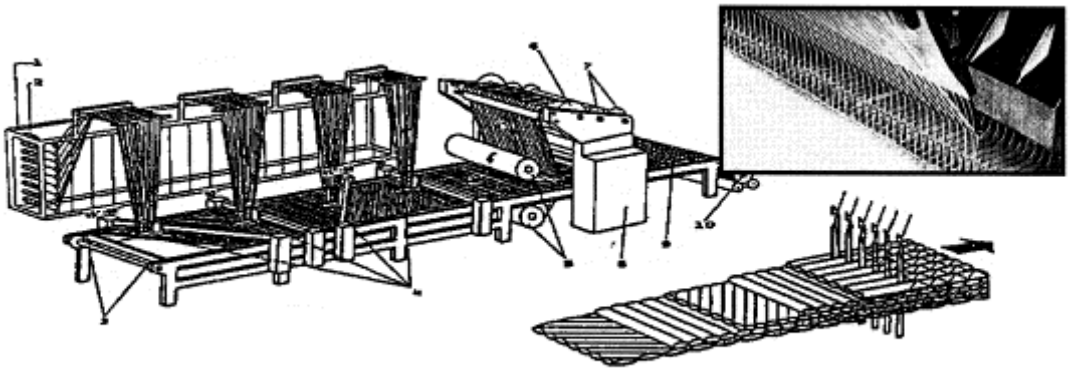

Figure 1.4. A schematic figure of production of NCF fiber preforms [4].

Figure 1.4 illustrates a four weft insertion system machine, but higher numbers are possible with larger machines which can also incorporate layers of fleeces or chopped strand mats. With the Liba system, reinforcing fibers are drawn from creels and then deposited in the required orientation via a weft insertion mechanism. The weft insertion mechanism comprises yarn carriers that oscillate between the width of the machine during which the fiber yarns are laid down and secured before they are all finally fixed together by means of a warp-knit structure. Apart from 0^o and 90^0, the orientation of the fiber sheets can be laid down at off-axis angles of 30^o-45^o-60^o. The warp knitting needles are inserted in the thickness direction of the fabric thus exposing the straight fiber yarns to impalement and consequently fiber damage and misalignment.

Typically this production technique is used to produce bi, tri and quadriaxial fabrics of carbon or glass fiber using polyester or aramid warp knitting yarns. In order to minimize damage and fiber tow crimp, the amount of binder yarn is usually kept small but sufficient

to hold the bundles in the layers during handling of the fabric. Several preforms are normally stacked together creating a dry fabric thick enough for structural applications. This manufacturing technique creates dry performs which easily can be shaped into a desired structure before consolidation with composite matrix and it is attractive due to small amounts of material wastage, reduced production time and virtually unlimited shelf life resulting in lower production costs. Important parameters for the preform production are, besides the type of the fibers used in the tows, the inter-tow gap, stitch tension, stitch type, stitch density and stitch material.

1.5.2. Production of NCF Fiber Reinforced Composites

NCF composites can be manufactured using hand lay-up, vacuum bag/autoclave, compression moulding, injection moulding, pultrusion, cold press moulding, resin transfer moulding and vacuum infusion processes which have been explained earlier. Composites used in this thesis have been produced using vacuum infusion process which will be examined thoroughly later.

1.5.3. Internal Structure of NCF Fiber Reinforced Composites

NCF composites are an inherently multiscale material since the layers due to the knitting procedure are divided into fiber bundles. On the microscale, each bundle can be described as a pre-preg composite with a certain fiber content. On the mesoscale, the bundle can be considered as homogeneous transversely isotropic material surrounded by matrix and other bundles of the same or different orientation. An important mesoscale characteristic of the NCF composite is the bundle content in the composite. Figure 1.5 is a micrograph that shows the structure of a typical NCF composite.

The geometrical shape of the bundles (cross-section and axial alignment) is complex and depends on bundle orientation in the blanket, surface compression during production, resin pockets etc. This configuration determines the properties of NCF composite materials on macroscale.

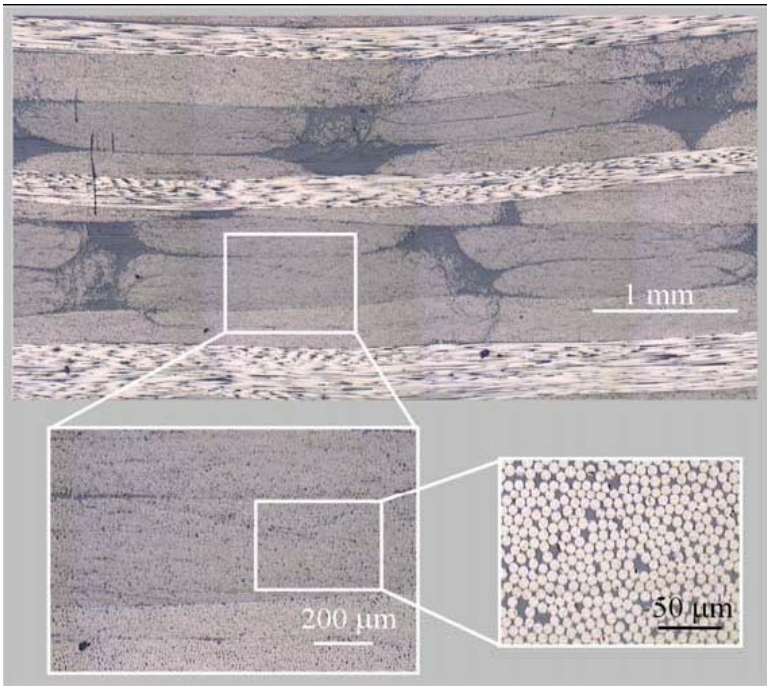

Figure 1.5. Internal structure of NCF composites [4]

The term non-crimp implies that the fibers in each lamina are straight and have no waviness perpendicular to the general fiber direction [7]. However, Drapier and Wisnom have shown in their studies that outer layers of the composites contain waviness to some extent due to nesting of the fibers into the gaps in the complementary direction [9] and this waviness is a key factor in predicting the mechanical properties of NCF composites [10].

Figure 1.6 shows fiber waviness schematically and Figure 1.7 is a micrograph of NCF composites produced during this study demonstrating fiber waviness clearly.

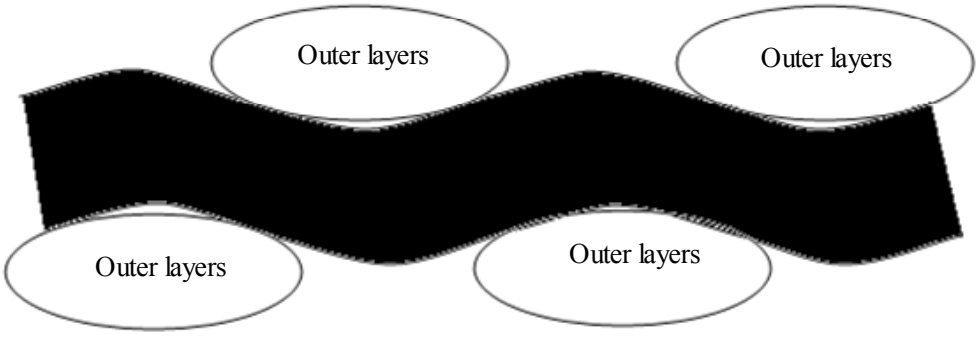

Figure 1.6. Nesting of the layers defining the waviness

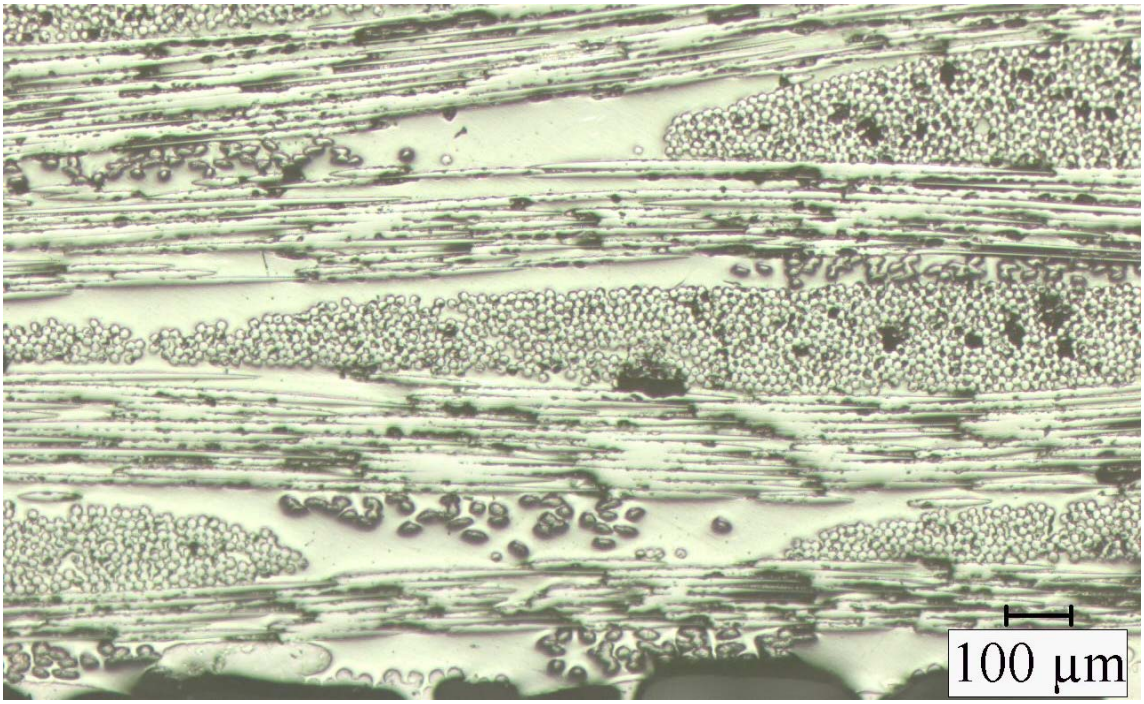

Figure 1.7. Micrograph showing waviness (crimp) in the outer layers

The mesoscale waviness in NCF composites are in some cases induced by the stitching tread in the sense that the tread separates the 0°-bundle from the adjacent bundles in the area closest to the tread as shown in Figure 1.8. This phenomenon can introduce waviness both in the in-plane and out-of plane direction.

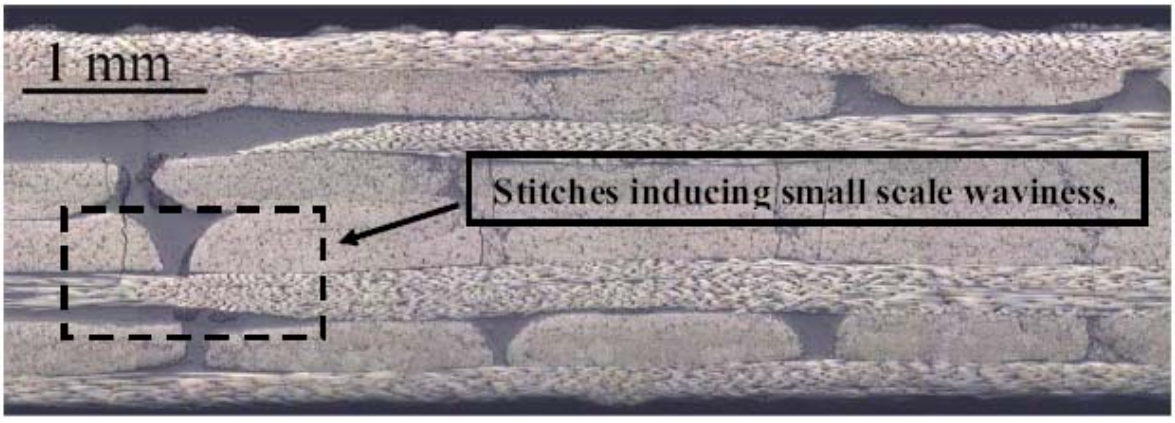

Figure 1.8. Micrograph showing stitches inducing waviness [4]

1.6. Literature Review on Mechanical Properties of NCF Composites

This section presents an overview of previous experimental and numerical findings on mechanical properties of NCF fabric reinforced composite materials which mainly cover tensile, compressive and flexural behaviour along with their comparison with those of other types of composites such as pre-pregs and woven composites.

Hogg, Ahmadnia and Guild [6] examined mechanical properties of biaxial angle-ply ± 45^o fabrics and quadriaxial fabrics with a 0^o, ± 45^o, 90^o, -45^o ply sequence as a function of weight and in relation to alternative composite forms by the use of tensile tests. For biaxial laminates, properties were assessed along the 0^o, +45^o and -45^o directions relative to the fabric axis (90^o direction is not listed as it is basically the same as 0^o direction for fibers oriented in +45^o and -45^o directions are literally the same) whereas quadriaxial fabric was evaluated along the directions, 0^o, +45^o, 90^o and -45^o. Representative stress/strain curves are demonstrated in Figure 1.9.

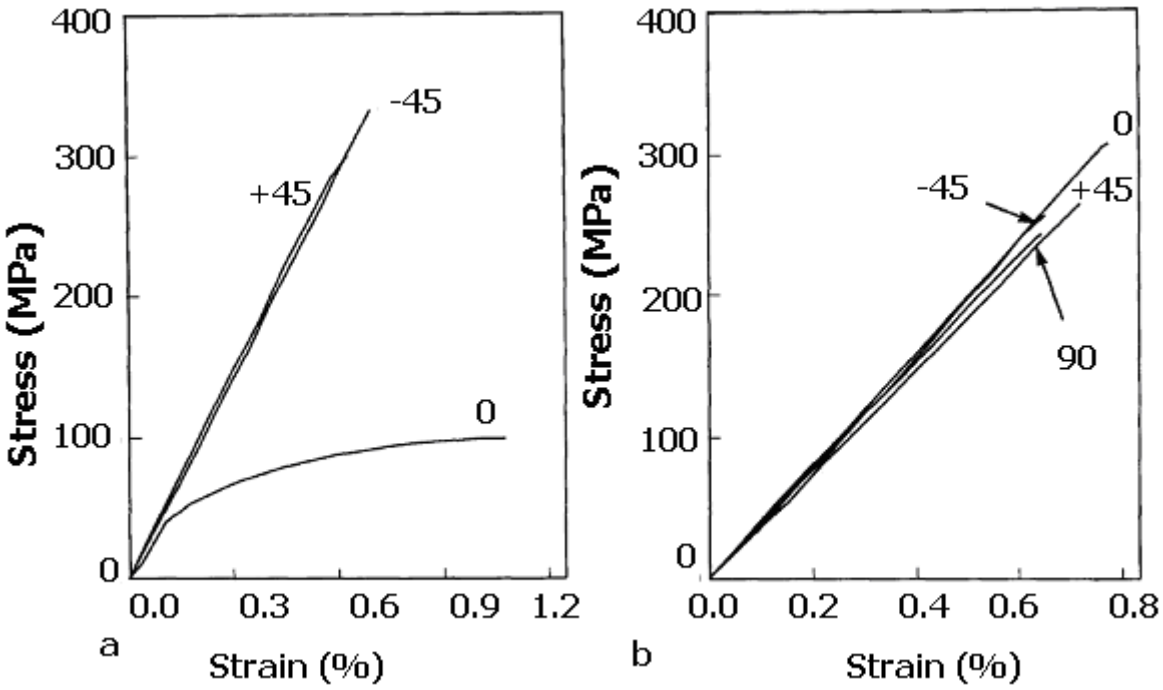

Figure 1.9. Representative stress/strain curves for (a) biaxial and (b) quadriaxial fabric laminates tested at various orientations [6]

Looking into Figure 1.9 (a) in detail, in biaxial laminates, considerable differences are apparent in the behaviour of the biaxial fabrics tested along the 0^o direction and along the $+45^o$ and -45^o directions, as would have been expected. The stress/strain curves in the $+45^o$ and -45^o direction, parallel to one of the fiber directions, are linear to fracture whereas in the 0^o direction non-linear behaviour is observed. In Figure 1.9 (b), it can be seen that the properties of the quadriaxial composites are consistent along the principal orientations. This behaviour is characterized as quasi-isotropic. A quasi-isotropic laminate is a planar isotropic laminate in the sense that it appears isotropic but it has bending extension coupling as well as a varying bending response as the laminate is rotated in plane.

In the studies of Hogg *et al* [6], it was also discovered that laminates produced from biaxial NCFs exhibit superior properties for a given volume fraction of reinforcement compared with similar laminates produced using woven rovings. Additionally to that, the properties of the biaxial NCF laminates were superior to those predicted for laminates of continuous fiber composites typified by pre-preg constructions of the same fiber and matrix. Quadriaxial NCF laminates exhibited equivalent properties to woven laminates at favourable orientations, but retained their properties when rotated through $+45^o$ whereas woven laminates suffer a significant reduction in properties at such orientations. In general, the properties of NCF laminates decreases slightly as the areal weight of the fabric used to produce the composite increases. NCFs and particularly biaxial NCFs loaded at $+45^o$ to the fiber and quadriaxial fabrics produce composites with superior properties to those predicted using finite element and laminate analysis for idealized laminated composites based on the same constituent materials.

Bibo *et al* [8] predicted macromechanical behaviour of unidirectional pre-preg (UDPT), NCF fiber reinforced and satin woven (WF) composites satisfactorily by using classical lamination theory (CLT). The fiber-glass laminates constructed in their work from unidirectional pre-preg tape consisted of 18 plies, those from eight-harness satin woven eight layers and those from the non-crimp fabric four blankets, all of which were laid up in such a way that each was compatible with another. They conducted tensile and compression tests on coupons cut in both 0^o and 90^o fiber orientations. Results obtained by these tests are presented in Figure 1.10 and Figure 1.11 for tension and compression respectively.

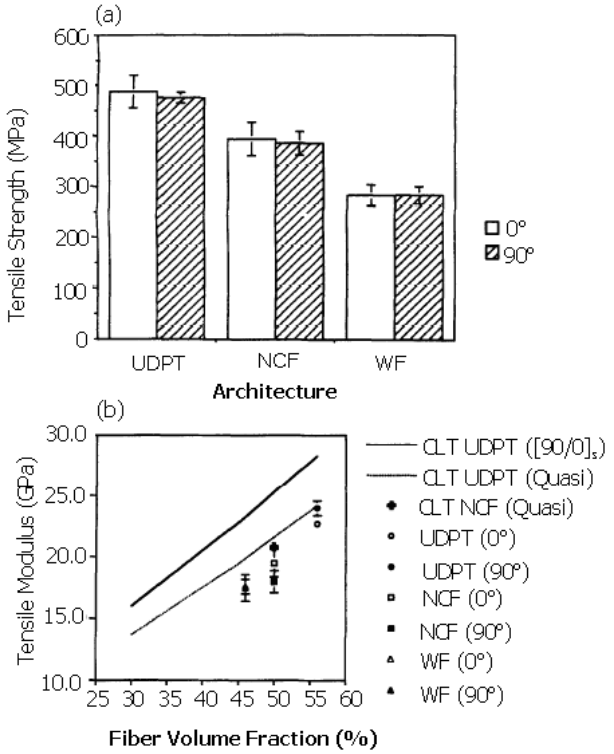

Figure 1.10. (a) Mean tensile strength values for composites, (b) Mean tensile moduli plotted vs. predicted values for laminate moduli calculated using CLT [8]

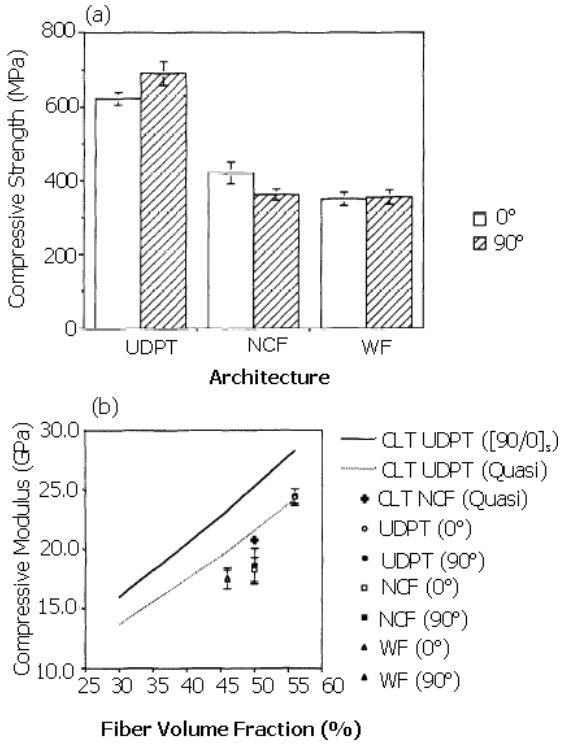

Figure 1.11. (a) Mean compressive strength values comparison for composites, (b) mean compressive moduli plotted vs. predicted values for moduli calculated using CLT [8]

Analyzing Figure 1.10 thoroughly, it is seen that the tensile strength and stiffness decrease in the following sequence: unidirectional pre-preg tape, NCF and eight-harness satin woven. A similar trend is observed in compression, but the individual behaviour of the unidirectional pre-preg tape and NCF appears to be dependent on orientation as shown in Figure 1.11. That is, the NCF is superior in the 0^o direction while the unidirectional pre-preg tape is stronger in the 90^o direction within their own material form. This orientation dependency is not observed in the case of the eight-harness satin woven composite.

Bibo *et al* [8] found out that the superiority of the unidirectional pre-preg tape in mechanical property terms was partly a consequence of differences in fiber volume fraction and did not appear to be so significant when plotted as a function of fiber volume fraction as Figure 1.10 (a) and (b) demonstrate. Figures 1.10 (b) and Figure 1.11 (b) show a comparison of modulus for the NCF and unidirectional pre-preg tape, respectively, with predicted modulus from the CLT. Also included in the figures are the experimental data for the eight-harness satin woven composites. The measured modulus for the unidirectional pre-preg tape shows very good correlation with theory while the NCF, experimentally, exhibits approximately a 10% reduction on the theoretically derived modulus. They attributed this reduction to a degree of fiber crimping or undulation, particularly in the surface layers of the blanket for compression and to the level of crimp and more importantly premature fracture of longitudinal fibers which has a knock effect for tension.

Wang, Li and Do [11] performed uniaxial tension and flexural tests on NCF composites, compared the results with CLT predictions and observed good agreements. They also found out that upon examination of the test results and inspections of failed specimens, NCF composites laminates behaved like their pre-preg counterparts. They used biaxial, triaxial and quadriaxial NCF fiberglass reinforced epoxy laminates in their work where they neglected the knitting yarns in their calculations as knitting yarns made up of about one per cent of the fabric weight. In Table 1.6, the ply orientation, unit weight of the plies and fiber layups of the laminates they studied are summarized. It can be seen from Table 1.5 that $0^o/90^o$ layups from $+45^o/-45^o$ biaxial fabrics (EBX 2400) are made from fabric pieces cut along the fabric's two diagonal directions ($+45^o$ and -45^o degrees) and stacked alternatively together.

Table 1.5. Fabrics used in the studies of Wang *et al* [11]

Code	Fabric	Areal Weight (g/m^2)	Plies	Layup
A1	EBX 2400	820	45/-45	$[90/0/0/90]_3$
A2	ELT 2400	814	0/90	$[0/90/90/0]_3$
A3	ELT 1200	445	0/90	$[0/90/90/0]_6$
B1	EBX 2400	820	45/-45	$[45/-45/-45/45]_3$
C1	ETTX 2400	805	45/0/-45	$[45/90/-45/-45/0/45]_3$
C2	EQX 2600	865	0/45/90/-45	$[90/-45/0/45/45/90/-45/0]_3$

Figure 1.12 (a) and Figure 1.13 (a) present experiment results and CLT predictions on tensile modulus and flexural modulus respectively, Figure 1.12 (b) and Figure 1.13 (b) present typical tensile and flexure stress-strain curves respectively.

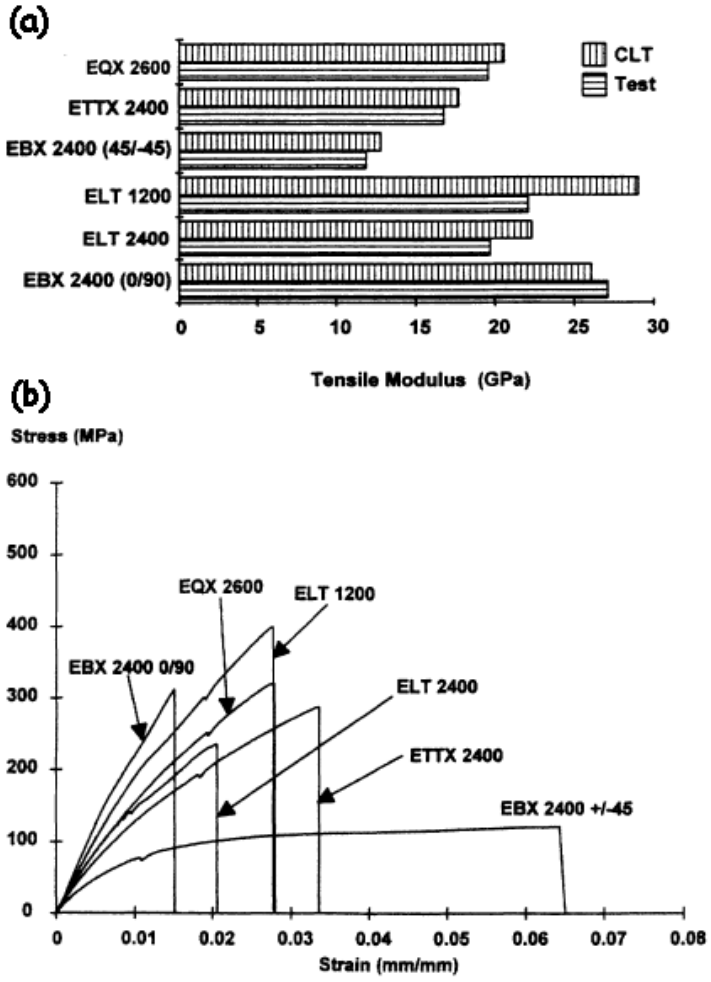

Figure 1.12. (a) Experiment results and CLT predictions on tensile modulus, (b) typical tensile stress-strain curves [11]

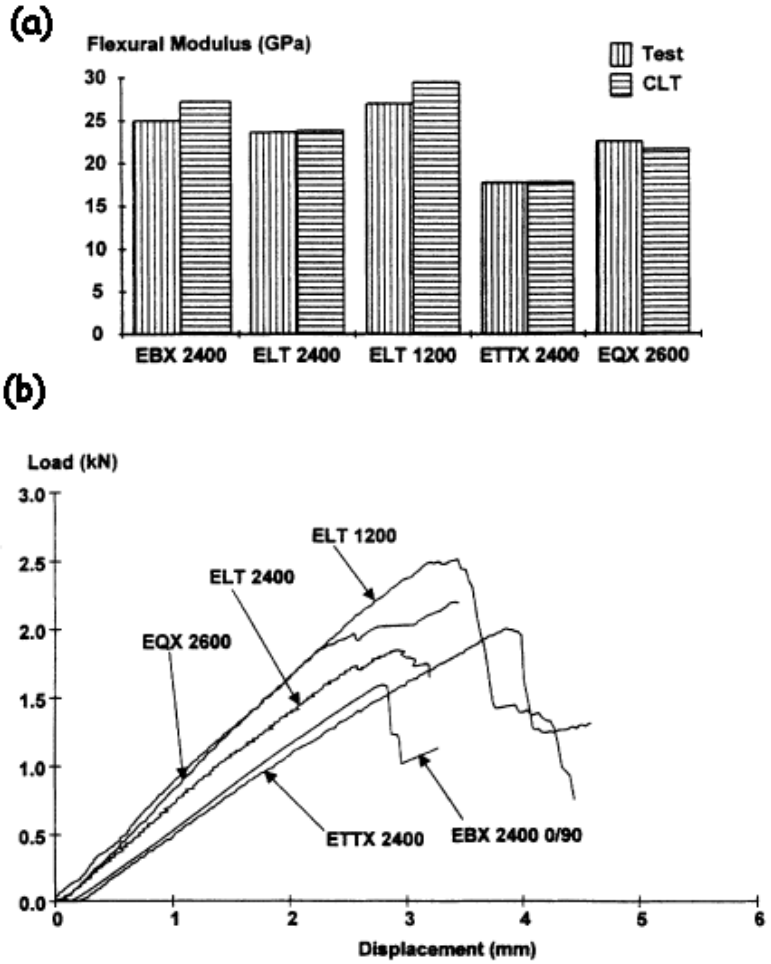

Figure 1.13. (a) Experiment results and CLT predictions on flexure modulus, (b) typical flexural load-displacement curves [11]

The test results and theoretical predictions on the tensile modulus are in reasonable agreement as seen in Figure 1.12 (a). The nonlinearity in tensile strain-stress response is observed in Figure 1.12 (b). Wang *et al* [11] observed the knee phenomenon due to the transverse and shear failure of 90^o and/or 45^o plies for almost all the laminates and explained this nonlinear effect as the result of progressive failures of multiple failure mechanisms. The failure mechanism was dependent on fiber direction and layups. For biaxial $0^o/90^o$ laminates, small transverse crack was first developed in the 90^o plies, followed by the delaminations between $0^o/90^o$ interfaces. The failure process was characterized by the failure of the outmost 0^o plies with subsequent inner plies. The $\pm 45^o$ laminates failed by edge delaminations at $\pm 45^o$ interfaces and multiple ply failure. On the other hand, for multidirectional laminates, delaminations, transverse cracks and fiber breaks were noticeable. Thus, they suggested that NCF laminates behave like their pre-

preg counterparts, hence the knowledge on pre-preg tape might be applicable to NCF laminates as well.

As illustrated in Figure 1.13 (a), there is a plausible agreement between CLT predictions and experimental modulus for the flexural modulus. Wang *et al* [11] noticed the brittle failure characteristic of the laminates as evident by the sharp drops in Figure 1.13 (b). They also observed in flexural testing that outer ply delamination preceded fiber failure and there was no visible damage to the compressive face at the point of loading while there were distinctive damage patterns on the tensile face of the specimens.

Wang [12] performed tensile tests on biaxial, triaxial and quadriaxial NCF fiberglass reinforced epoxy composites along the principal directions 0^o, 90^o and 45^o whose ply orientations, unit weights of the plies and fiber layups are listed in Table 1.6. Tensile test results are also illustrated in Figure 1.14 (a) through Figure 1.14 (c).

Table 1.6. Fabrics used in the studies of Wang [12]

Fabric	Areal Weight (g/m^2)	Plies	Layup
EBX 2400	820	45/-45	$[45/-45/-45/45]_3$
ETTX 2400	805	45/0/-45	$[45/90/-45/45/0/-45]_3$
EQX 2600	865	0/45/90/-45	$[90/-45/0/45/45/90/-45/0]_3$

The stress-strain curves for the EBX 2400 biaxial laminate are given in Figure 1.14 (a). Distinctive tensile stress–strain responses are observed along a 45^o direction and along the directions 0^o and 90^o, which concurs with findings of Hogg *et al* [6]. In the 45^o direction, the response is near linear, though gradual softening is evident as the load increases. Wang [12] pointed out that final failure is associated with delamination, especially along the longitudinal fiber bundles. When loaded in the 0^o and 90^o directions, significant nonlinearity in the stress–strain response starts at relatively low load, and the load remains near constant as the specimen extends before its final failure at a strain of about 9 per cent. He noted that the nonlinear effect was the result of progressive failure due to various interacting micro-failure modes, such as matrix shearing, cracking, fiber debonding, fiber pull-out and interply tearing.

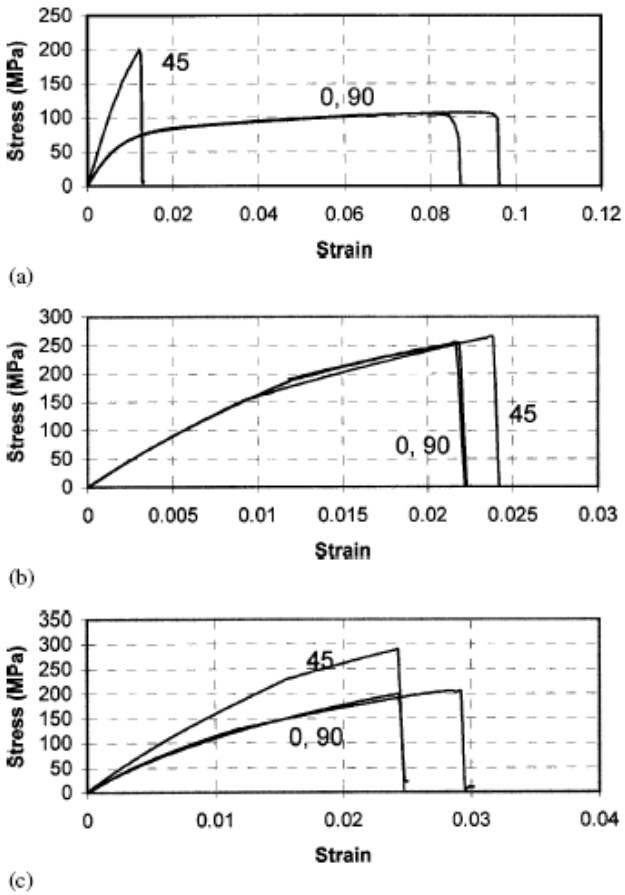

Figure 1.14. Typical tensile test curves for NCF composite laminates: (a) biaxial, (b) triaxial, and (c) quadriaxial [12]

Figure 1.14 (b) shows the tensile test curves for the ETTX 2400 triaxial laminate. Fibers in the laminate are distributed along the loading, perpendicular to the loading, and in the bias directions for all the tests along the three directions. Though similar stress–strain responses were observed by Wang [12] along the three directions, the laminate was stiffer in the 45^{o} direction since 33 per cent of fibers were in this direction whereas only 17 per cent of fibers were parallel to the 0^{o} or 90^{o} direction. The nonlinearity in the stress-strain responses was more pronounced in this triaxial laminate than in the biaxial laminates along a fiber direction. This was explained due to the fact that fewer fibers in the triaxial laminate were along the loading directions, and the cross and bias plies play a larger role.

As illustrated in Figure 1.14 (c), the tensile responses for the EQX 2600 quadriaxial laminate are nearly identical along the three test directions. Wang [12] pointed out that this was expected because the laminate had a quasi-isotropic layup and it should have the same

in-plane stiffness along any direction. The fiber distribution also remained unchanged with respect to three loading directions and thus similar strengths along them were expected. However, the strength along other directions would significantly different than along the three test directions. If the laminate had been tested along the 22.5^{o} direction, a lower strength and more pronounced stress–strain nonlinearity would be expected. In most cases, the final failure due to delamination was within a small region rather than throughout the entire gage length.

Edgren, Mattsson, Leif, Varna [7] tested cross-ply NCF laminates in tension and monitored intralaminar cracks caused in the 90^{o} fiber bundle layers and their effect on laminate mechanical properties. They explained the occurrence of novel type of cracks propagating in the load direction (longitudinal cracks) by a thorough FE analysis using an Representative Volume Element (RVE) approach, revealing stress concentrations caused by 0^{o} fiber bundle waviness. They observed damage in the form of cracks only in layers with 90^{o} orientation of fiber bundles. Then, they divided the observed cracks into four groups, depending on location and orientation with respect to the laminate mid-plane. The different crack types were named: longitudinal cracks; half cracks; whole cracks and double cracks. Specific features of these cracks are schematically illustrated in Figure 1.15.

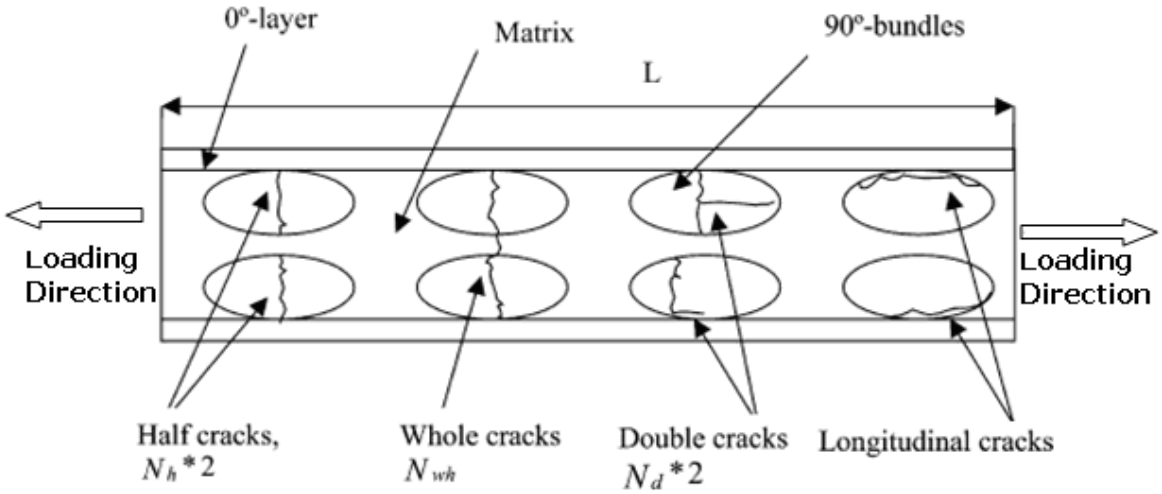

Figure 1.15. Schematic showing the four crack types observed in NCF cross-ply laminates; namely, half cracks, whole cracks, double cracks and longitudinal cracks [7]

Edgren *et al* [7] discovered in their studies that half cracks that were contained in a single 90^o fiber bundle and, hence, only extended through half the 90^o layer, occurred first (at a strain of approximately 0.4 per cent) and dominated over all other crack types. The other crack types initiated at slightly higher strains more than 0.5 per cent. Of these, longitudinal cracks occurring by them self in a single bundle or linked to a half crack forming a double crack were never observed in traditional pre-preg composites. Longitudinal cracks formed at stress concentrations caused by the forced straightening of the 0^o fiber bundles in tension. The effect of the fiber waviness was strongest for the analysed case where the upper and lower 0^o fiber bundles were extending out of phase.

Mattson, Joffe and Varna [13] investigated two cases ($[0/90]_{2s}$ and $[90/0]_{2s}$) cross-ply NCF composites in tensile loading and ended up with the result that much larger elastic modulus reduction was observed in former than in latter. Degradation of the elastic moduli for both lay-ups as a function of the applied strain and typical stress–strain curves for both laminates are presented in Figure 1.16 and Figure 1.17 respectively. Since transverse cracks in 90^o bundles may give modulus decrease about 5%, they ascribed the observed 40% stiffness reduction to failure and delamination of bundles oriented in the direction of the applied load.

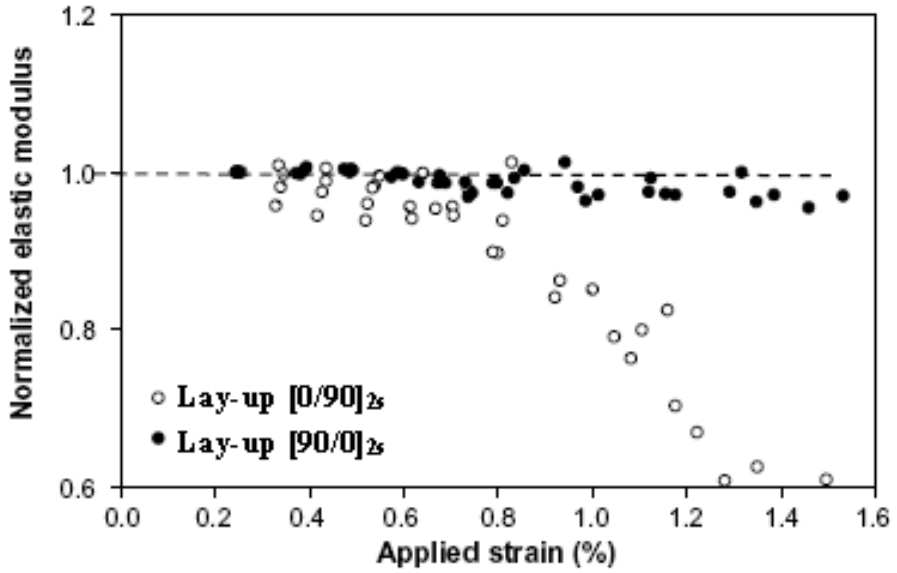

Figure 1.16. Elastic modulus for both lay-ups as a function of applied strain [13]

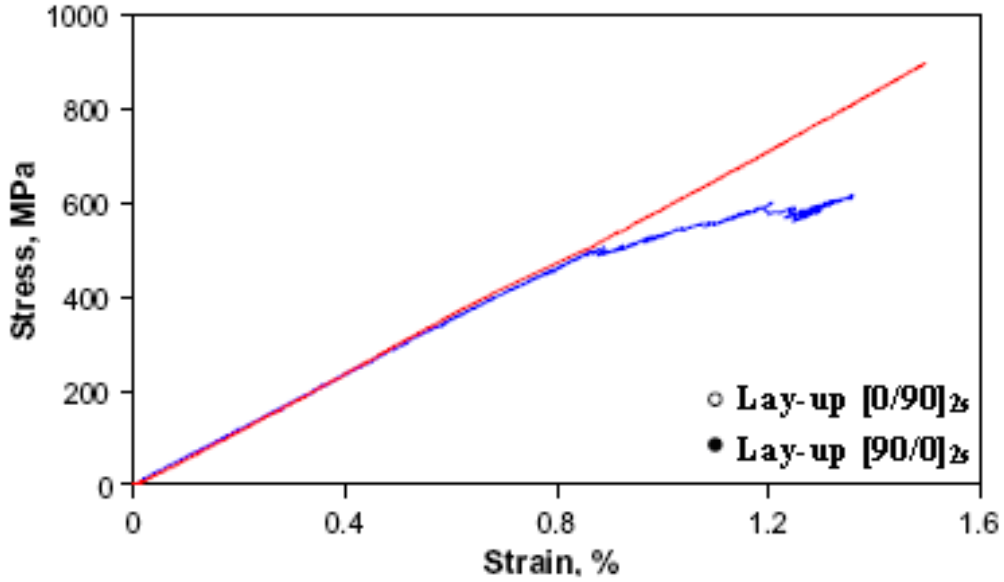

Figure 1.17. Typical strain-stress curves for both laminate cases [13]

Mattsson *et al* [13] suggested two reasons for higher stiffness reduction in the $[0/90]_{2s}$ case: (a) if two imperfect 0^o-bundle layers are separated by a 90^o-bundle layer their resistance to failure is lower than when they are situated next to each other; (b) the effect of each surface 0^o-bundle break on the composite stiffness is larger (due to less constraint from the surrounding material the opening of surface bundle breaks is much larger).

1.7. Objective of the Study

The objectives in this study are generally twofold. Firstly, mechanical properties of fiberglass – polyester resin composite materials are aimed to be investigated. In this respect, laminates of various number of plies, various stacking sequences (e.g., cross-ply and quasi-isotropic) are manufactured using vacuum infusion process and then subjected to tensile loads in 0^o, 45^o and 90^o directions.

Secondly, applicability of predictive theories for strength and stifness which are used for pre-preg composites, to NCF composites are investigated. In this regard, engineering values of each laminate type are predicted, obtained values are compared with experimental values and by the help of this comparison, a general reliability factor for fiberglass – polyester resin composite materials is also aimed to be obtained.

2. EXPERIMENTAL WORK

In this chapter, materials used in the manufacturing of the NCF fiberglass reinforced composites which have been tested during the whole work are presented and vacuum infusion process (VIP) via which composites have been produced is explained in detail. Procedures for tensile testing and fiber, resin and void volume fractions are also explained.

2.1. Materials

2.1.1. Fibers

Three different types of E-glass reinforcements procured from METYX Composites Company, Turkey were used in the manufacturing, two of them being biaxial and the other being quadriaxial. Biaxial means there are only two plies with different orientations that are perpendicular to each other whereas quadriaxial means there are four plies of distinct orientations. Properties of the NCF fibreglasses are listed in Table 2.1.

Table 2.1. Properties of the fibreglasses used [14]

Fiberglass		Biaxial						Quadriaxial				
Product		LT300 E10A E-Glass Fabric			LT300 E10B E-Glass Fabric			Q625 E10C Quadriaxial E-Glass Fabric				
Ply Orientation		Biaxial 0/90			Biaxial 0/90			Quadriaxial 0/-45/+45/90				
Ply		0	90	Stitch	0	90	Stitch	0	-45	+45	90	Stitch
Rein.	Type (TEX)	410	300	7,6	300/600	300	7,6	300/600	300	300	300	7,6
	Area Weight (g/m^2)	161	142	10	177	142	10	177	150	150	154	10
Area Weight	(g/m^2)	313 (± %3)			329 (± %3)			641 (± %3)				
Stitch Gauge		10 stitches/inch			10 stitches/inch			10 stitches/inch				
Stitch Type		Tricot			Tricot			Tricot				
Stitch Length		3 mm			3 mm			3 mm				

2.1.2. Resin Material

Resin material used is Scott Bader Cystic 703PA which is a pre-accelerated, closed mould DCBD (1,4-dichloro-2,3-butanediol) based polyester resin with low viscosity and controlled exothermic characteristic [15].

Polyester is a category of polymers which contain the ester functional group in their main chain. Although there are many polyesters, the term "polyester" as a specific material most commonly refers to polyethylene terephthalate (PET) for which the chemical structure is shown in Figure 2.1. Polyesters include naturally-occurring chemicals, such as in the cutin of plant cuticles and synthetics through step-growth polymerization such as polycarbonate and polybutyrate. The formulation for polyester resins can be adjusted to result in different toughness and modulus properties. Polyester resins have a relatively low viscosity, low cost, and have relatively fast cure times, but generally inferior properties compared with epoxies. The greatest disadvantage of polyester is the relatively high volumetric shrink rate when curing [16].

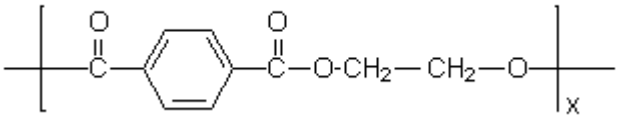

Figure 2.1. Chemical structure of PET

The catalyst used for Crystic 703PA is Butanox M60 from Akzo Nobel Polymer Chemicals Company, which was added at 1,5 per cent into the resin. Butanox M60 is a general purpose methyl ethyl ketone peroxide (MEKP) for the curing of unsaturated polyester resins that can be used both at room temperature and elevated temperature [17]. (Figure 2.2)

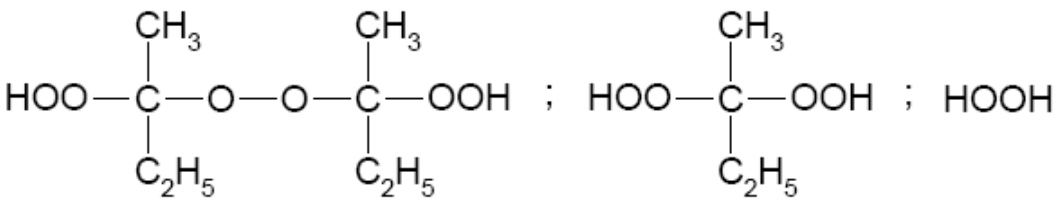

Figure 2.2. Chemical structure of Butanox M60 [17]

Table 2.2 and Table 2.3 list chemical and mechanical properties of Crystic 703PA and Butanox M60 successively.

Table 2.2. Mechanical and chemical properties of Crystic 703PA [15]

Property		Liquid Resin	
Appearance		Mauvish	
Viscosity at 25°C	poise	1,6	
Volatile Content	%	28	
Geltime with 1.5% Butanox M60	minutes	124	
Property		Cured – 24 hrs @ 20°C, 16 hrs @ 40°C	Cured – 24 hrs @ 20°C, 3 hrs @ 80°C
Barcol Hardness		42	43
Deflection Temperature Under Load (1.8 MPa)	°C	59	64
Water absorption	mg	-	11
Tensile Strength	MPa	49	38
Tensile Modulus	MPa	2758	3162
Poisson's Ratio		0,38	0,38
Elongation at Break	%	2,1	1,3

Table 2.3. Typical chemical properties of Butanox M60 [17]

Property		Data
Appearance		clear and colorless liquid
Density, 20°C	kg/m^3	1170
Viscosity, 20°C	mPa.s	25
Total active O_2	%	9,8 – 10,0
Balance		60% DMP, 4% MEK + water
Flash point		Above the Self Accelerating Decomposition Temperature (SADT)

Table 2.3. Typical chemical properties of Butanox M60 [17] (continued)

SADT	°C	60
Auto ignition Temperature	°C	220
Solubility		Insoluble in water, soluble in phthalates

2.2. Vacuum Infusion Process

VIP is a widely used moulding process for the manufacture of large composite structures. Its popularity is partly due to the low cost of the tooling and the environmental safety (the process eliminates more than 90 % of the volatile organic compound emitted by unsaturated polyester resins). In addition, low operator involvement increases the repeatability of the process compared to open mould techniques such as hand lay-up or spray-up and the components are of relatively high fiber content, up to 60 % by volume [18]. VIP is increasingly popular in the transportation, marine and wind power generation industries. Thick, single skin laminates and sandwich structures are produced using this method. Components are traditionally made of glass fiber and polyester resin, but now VI is also used for the manufacture of carbon fiber – epoxy components dedicated to aeronautic and aerospace sectors.

Vacuum infusion process presents similarities with resin transfer moulding (RTM). The most striking difference is that the fully enclosing, two-part rigid moulds used in RTM are replaced with a one-part rigid mould sealed with a vacuum bag (Figure 2.3).

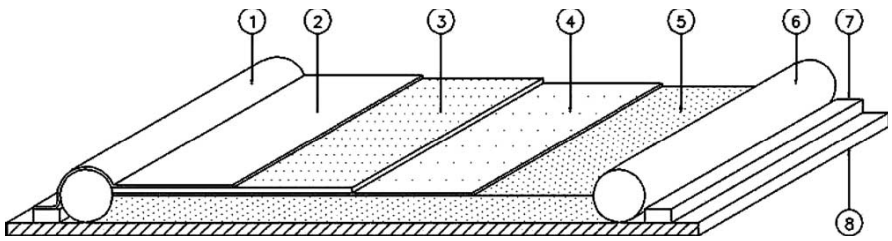

Figure 2.3. VIP mould assembly: 1-inlet, 2-vacuum bag, 3-distribution medium, 4-peel-ply, 5-reinforcement, 6-outlet, 7-vacuum seal, 8-glass mould [19]

Reinforcement is laid on the rigid mould with a layer of removable flow-enhancement medium, used to reduce fill time, along with peel ply to facilitate disposal. Inlets and outlets are placed and the vacuum bag is sealed to the rigid mould using a sealant tape as shown in Figure 2.3. Air is extracted from the cavity to compact the preform between the vacuum bag and the mould, and to subject resin to a pressure differential. As a result, resin flows through the compacted perform [19]. Figure 2.4 illustrates a generic view of sequence of events in VIP [20].

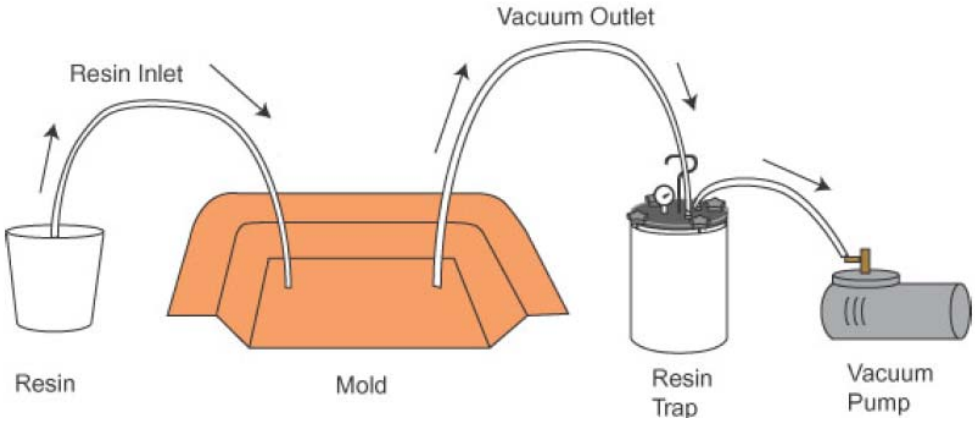

Figure 2.4. Sequence of events in a typical VIP

Vacuum infusion process is known under different acronyms, all describing methods based on the impregnation of a dry reinforcement by liquid thermoset resin driven under vacuum. VARTM (Vacuum Assisted Resin Transfer Moulding), SCRIMP (Seemann Composites Resin Infusion Moulding Process), VBRTM (Vacuum Bag Resin Transfer Moulding), VARI (Vacuum Assisted Resin Injection Process) and RIFT (Resin Injection under Flexible Tooling) are the most popular terms to describe vacuum infusion processes. All involve basically the same technology, with some patented to cover different elements of the process, and others generic names. SCRIMP focuses on the use of a flow enhancement medium to reduce infusion time for the moulding of skin and sandwiches structures. The RIFT method involves the use of a semi-flexible membrane, typically a glass - polyester composite shell, instead of a smooth vacuum bag as used in VBRTM. The latter is used as a generic name to describe the vacuum infusion process. VARI is not different from a general vacuum infusion process and the set-up includes a highly permeable layer on one side of the preform as for SCRIMP. Finally VARTM is described

as a variant of the RTM process but it is also used as a generic name to describe the vacuum infusion process (VIP) [18], [19].

2.2.1. Benefits of VIP

The main advantages of VIP, compared to other open mould and closed mould processes are manifold [18], [20]:

- higher fiber fraction volume and thus improvement of the laminate quality is achieved due to a better impregnation of the perform.

- operator involvement is less critical, leading to higher quality and consistency.

- less resin (hence less money) is wasted because resin usage is very predictable.

- there is no time constraint before the VIP can take place because the vacuum is applied while the fibers are still dry and in case any problem arises, it can be fixed before starting the infusion of the resin.

- it provides a cleaner, safer and friendlier work environment (though it is still important to work in a well ventilated area, wear respirator and other appropriate safety equipment)

- existing hand lay-up - spray-up moulds can be modified for use in VIP.

- there is no limitation in part dimensions and it is possible to produce components from 1 mm thick to more than 100 mm thick.

- the process reduces styrene emissions and capital costs (no injection machine is required), compared to other moulding techniques such as RTM. It reduces cycle times when compared to hand lay-up, and permits accurate placement of the reinforcement layers.

2.2.2. Potential Shortcomings of VIP

Like any laminating process, VIP is not without its drawbacks. The process is sensitive to leakage in the flexible membrane and a good surface finish is only available on one side of the part. Once the process has started, there is literally little that can be done to correct any errors or revert back. Thus, the process requires very careful planning. Complex geometries such as sharp edges and thickness variations can disturb the flow. When core inserts are included, they must be made of closed cells so as not to absorb resin which would increase the weight of the component. Fibers as well as chemicals used such as resin, catalyst, cleaners, waxes, releasing agents are hazardous to human body, so great care needs to be taken into consideration in the whole process. Finally disposable materials (tape, pipes, valves, distribution medium, bleed out fabric) produce waste and mould setup requires significant man-hours.

2.2.3. VIP Procedure

VIP procedure that was followed in the manufacturing of all NCF fiberglass reinforced composites used in this work that have distinct constituents and stacking sequences is presented in great detail and illustrated with appropriate pictures as follows:

1. Having selected a suitable rigid mould and having placed it on a straight surface, the mould is properly cleaned with a cleaning solvent so that high-gloss finish is achieved.

2. A tape is plastered on the borders of the mould as shown in Figure 2.5 so that sealant tape can be applied later on the mould after step 3.

3. Releasing agent is applied on the mould to make sure resulting composite can be removed off the mould once the process has been finished. In this work, CX500 type releasing agent from AXEL Plastics Company was used.

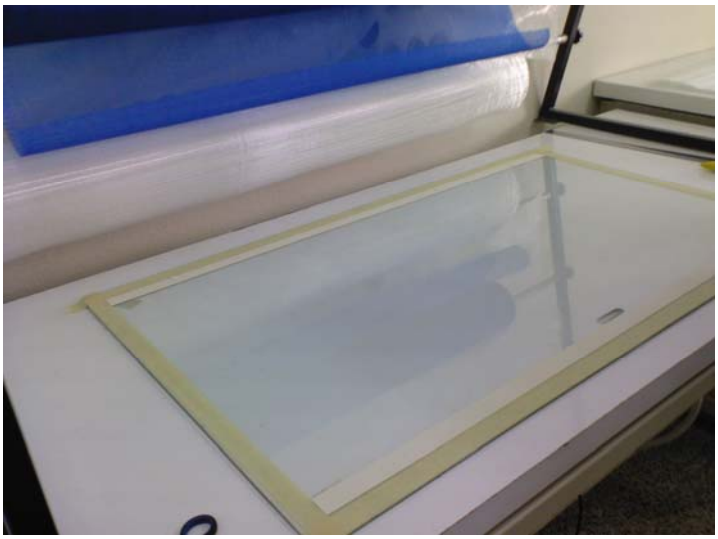

Figure 2.5. Tape plastered on the mould

4. Fiber lay-ups are stacked on top in the desired order, The tape is removed, sealant tape is applied around the fibers on the mould. (as illustrated in Figure 2.6)

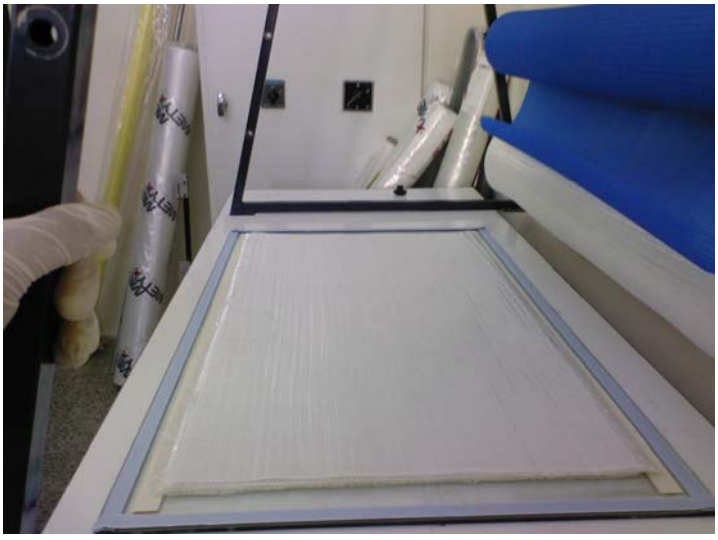

Figure 2.6. Fibers placed on the mould

5. Double sided tape is placed on both sides just between the sealant tape and the fibers and spiral tubings are stuck on the double sided tapes.

6. The peel-ply is placed onto the fibers in order that it gives a pattern to the fibers and any material (distribution media or spiral tubing) that will be removed later is not

infused into the part. (Figure 2.7). It should be ensured that spiral tubings are wrapped in peel-ply for easy removal.

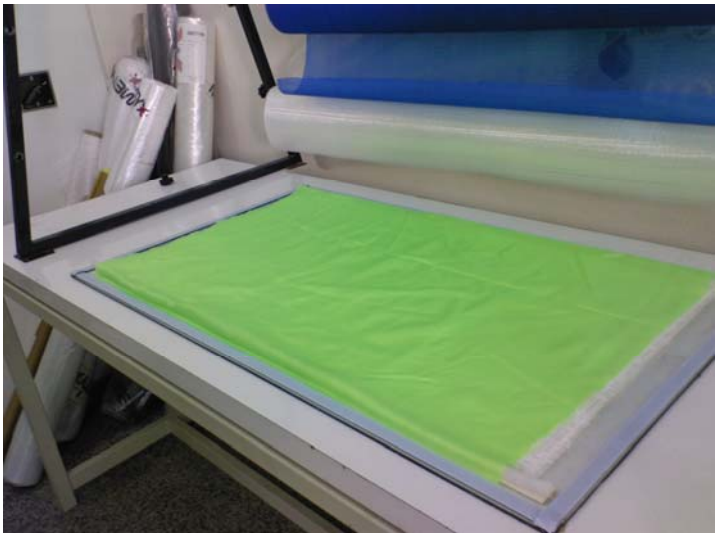

Figure 2.7. Peel-ply placed onto the fibers

7. The distribution media is placed on the peel ply so as to speed up the flow of the resin into the fibers as shown in Figure 2.8.

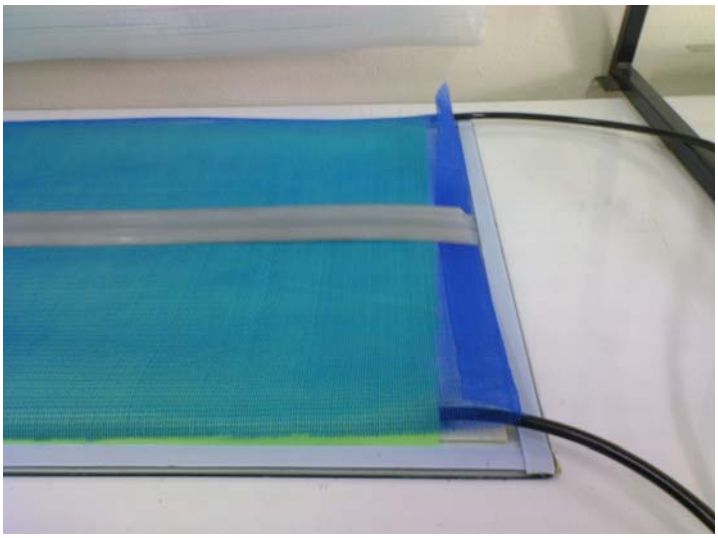

Figure 2.8. The distribution media laid on a peel ply together with vacuum outlet hose

8. Vacuum outlet hoses are bridged between distribution media and the resin trap which is connected to the vacuum pump.

9. Resin inlet hose is placed between the resin reservoir and the distribution media.

10. Papers of the sealant tapes are peeled off, vacuum bag is placed on the sealants, end of the resin inlet hose at the resin reservoir is bent or closed, then the vacuum pump is run to evacuate the air in the vacuum bag while keeping the end of the resin inlet hose closed so that no air enters in as shown in Figure 2.9. Leakages, if any, can be detected using an ultrasonic leak detector.

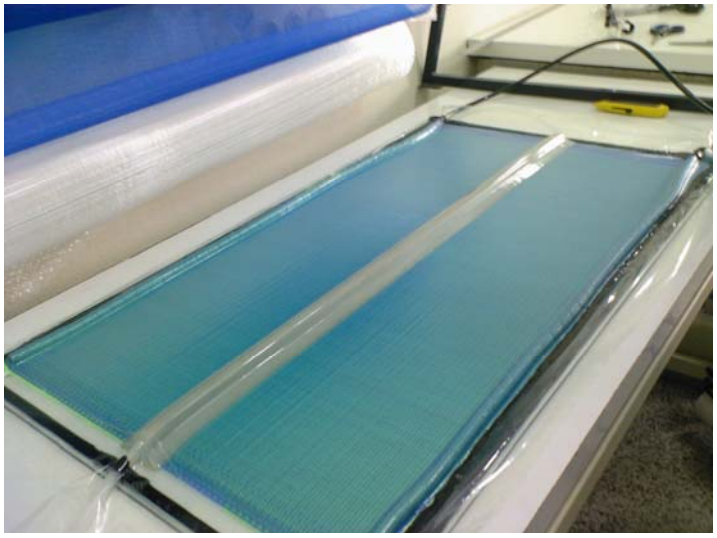

Figure 2.9. Full suction of initial air in the system is achieved

11. End of the resin inlet hose is placed in the resin reservoir into which resin prepared with the incorporation of catalyst (Crystic 703PA along with 1,5 per cent Butanox M60) has already been poured while the vacuum pump is still working (Figure 2.10)

12. Once the fibers are entirely wet, end of the resin inlet hose at the resin reservoir is clamped or bent off so that no air enters into the system (otherwise, the mechanical properties of the composite would be partly deteriorated or the composite material would get completely unusable in which cases the whole process would need to be carried out again).

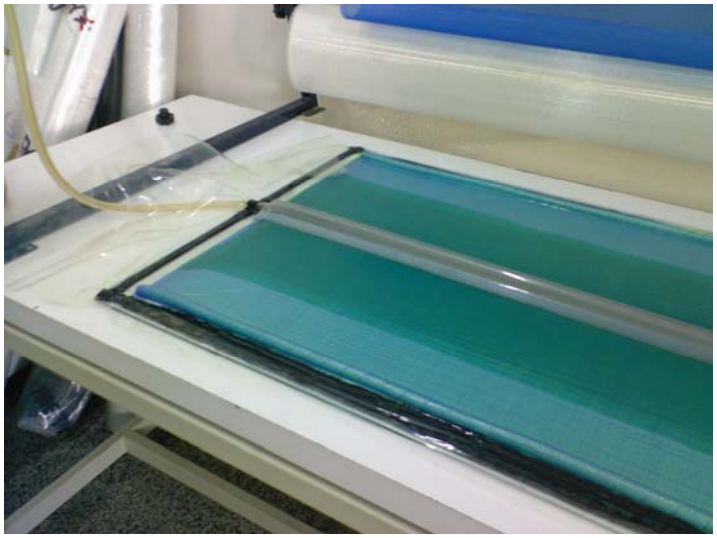

Figure 2.10. Resin is being sucked into the system

13. Until the resin turns into a jelly state and finally gets solidified, the vacuum pump is kept operating. In this work, the geltime (pot life) of the resin material was around 84 minutes. When the resin is fully in its solid state, the vacuum pump is shut off, the vacuum line is removed.

2.3. Post Curing and Specimen Preparation

After the vacuum infusion process got completed, the composite produced was allowed to cure for 24 hours at room temperature for optimum properties. Afterwards, all the materials on the composite (peel ply, strand mat, hoses, spiral tubings etc.) were removed and peeled off to end up with the final product as shown in Figure 2.11.

Later, lines that define rectangular shapes were drawn on the material in directions shown in Figure 2.12 so that for each fiber lay-up there are three stacking sequences where in one of them 0^o direction is along the longitudinal fibers, in another 0^o direction is along the transverse fibers and in the last one 0^o direction makes a 45^o with the longitudinal fibers. In the latter one, whether the 0^o direction makes $+45^o$ or -45^o with the axial fibers would not affect mechanical properties of the material if the areal weights of both fibers were equal to each other [11].

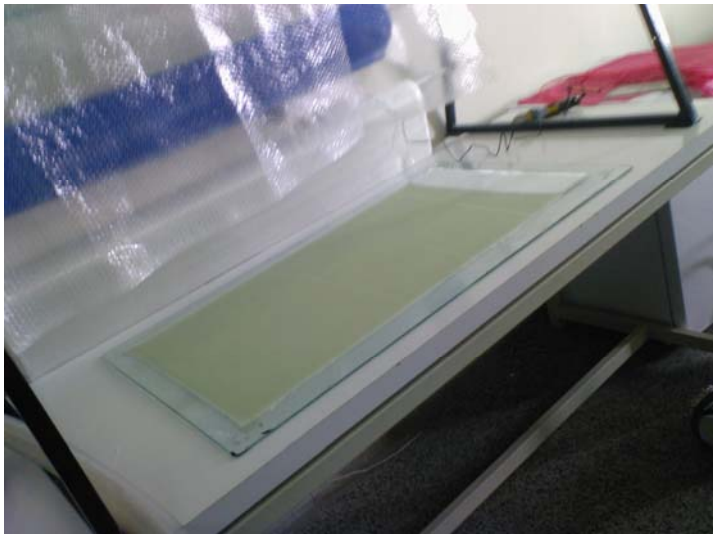

Figure 2.11. Final material after cure at room temperature

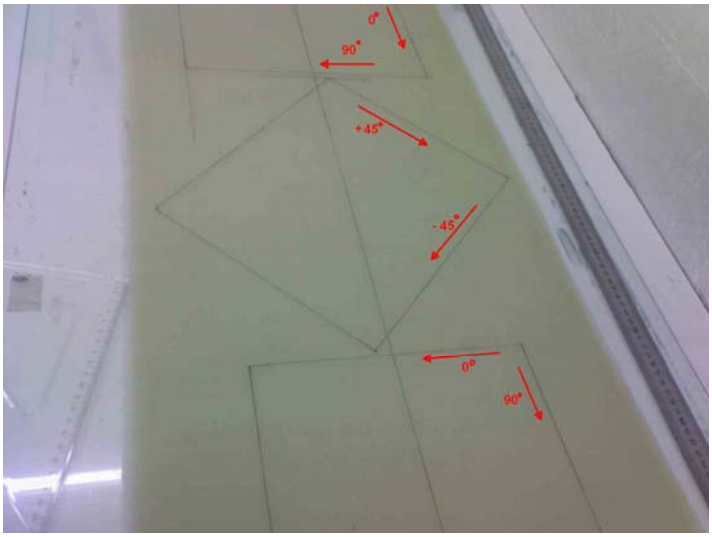

Figure 2.12. Lines are drawn on the material to get desired orientations

The rectangular shapes in Figure 2.12 were cut off the material by using a water cooled diamond blade and out of these rectangles, test specimens were then cut and hand sanded with coarse and fine emery papers in turn to remove fuzzy edges caused by the cutting operations and to reach dimensions as per the requirements of test method ISO 527-5 (Figure 2.13) [21].

The specimens were then oven cured for 16 hours at 40^{o}C where in the last hour vacuum pump was connected to the oven and vacuum was applied to the specimens inside

to release any remaining volatiles and moisture due to cutting within, after which the specimens became ready for use in mechanical testing.

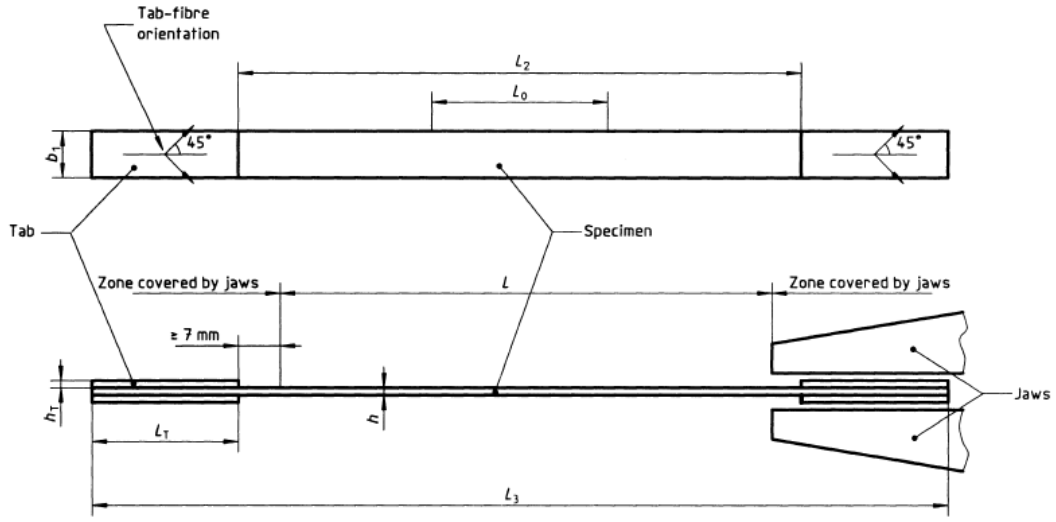

L_3	Overall length	250
L_2	Distance between end tabs	150 ± 1
b_1	Width	25 ± 0,5
h	Thickness	1 ± 0,2
L_0	Gauge length (recommended for extensometers)	50 ± 1
L	Initial distance between grips (nominal)	136
L_T	Length of end tabs	⩾ 50[a]
h_T	Thickness of end tabs	0,5 to 2

Figure 2.13. Dimensions of the specimens as per ISO 527-5 [21]

Laminates produced in this work are symmetric laminates. A symmetric laminate has both geometric and material property symmetry about the middle surface. The ply material, ply orientation and ply thickness at a positive distance z from the middle surface are identical to the corresponding values at an equal negative distance z from the middle surface. Figure 2.14 depicts symmetric angle-ply and cross-ply laminates. Advantage of using symmetric laminates is that bending-stretching coupling is not present in such laminates. Consequently, in-plane loads do not generate bending and twisting curvatures that cause out-of-plane warping, and bending or twisting moments do not produce an extension of the middle surface [1]. Symmetric laminates are symbolized with subscript *n*s where *n* is the number of layers of the repeating sequence in each side with respect to the middle surface and *s* stands for symmetry.

The laminate stacking sequences and the corresponding fiberglass types of the specimens manufactured via VIP explained above and used throughout the whole work is tabulated in Table 2.4.

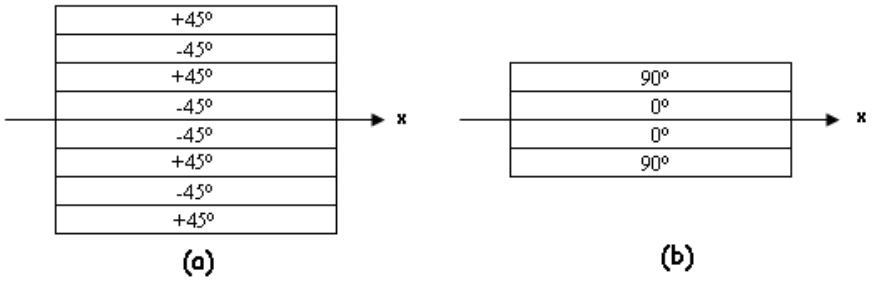

Figure 2.14. Examples of symmetric laminates; (a) symmetric angle-ply ($[+45/-45]_{2s}$), (b) symmetric cross-ply ($[90/0]_s$)

Table 2.4. The laminate stacking sequences and the fiberglass types of the specimens

Stacking Sequences			Fiberglass
Bi-axial	4 plies	$[0/90]_s$ in 0^o, 45^o and 90^o directions	LT300 E10A
	8 plies	$[0/90]_{2s}$ in 0^o, 45^o and 90^o directions	LT300 E10A
	16 plies	$[0/90]_{4s}$ in 0^o, 45^o and 90^o directions	LT300 E10B
Quadri-axial	8 plies	$[0/-45/+45/90]_s$ in 0^o, 45^o and 90^o directions	Q625 E10C
	16 plies	$[0/-45/+45/90]_{2s}$ in 0^o, 45^o and 90^o directions	Q625 E10C

2.4. Tensile Testing of the Composite Specimens

Mechanical tests were conducted according to ISO 527-5 Standard with a loading rate of 1 mm/min and were performed on an Instron 8801 servohydraulic testing machine (as shown in Figure 2.15) with 100 kN load cells and total actuator stroke of 75 mm integrated with an Instron 3520 hydraulic power unit having an operating pressure of 207 bar and motor size of 24.8 hp. During the tests, longitudinal strains were measured using an extensometer with a gauge length of 50 mm. Figure 2.16 shows a sketch of the experimental setup of the tensile testing.

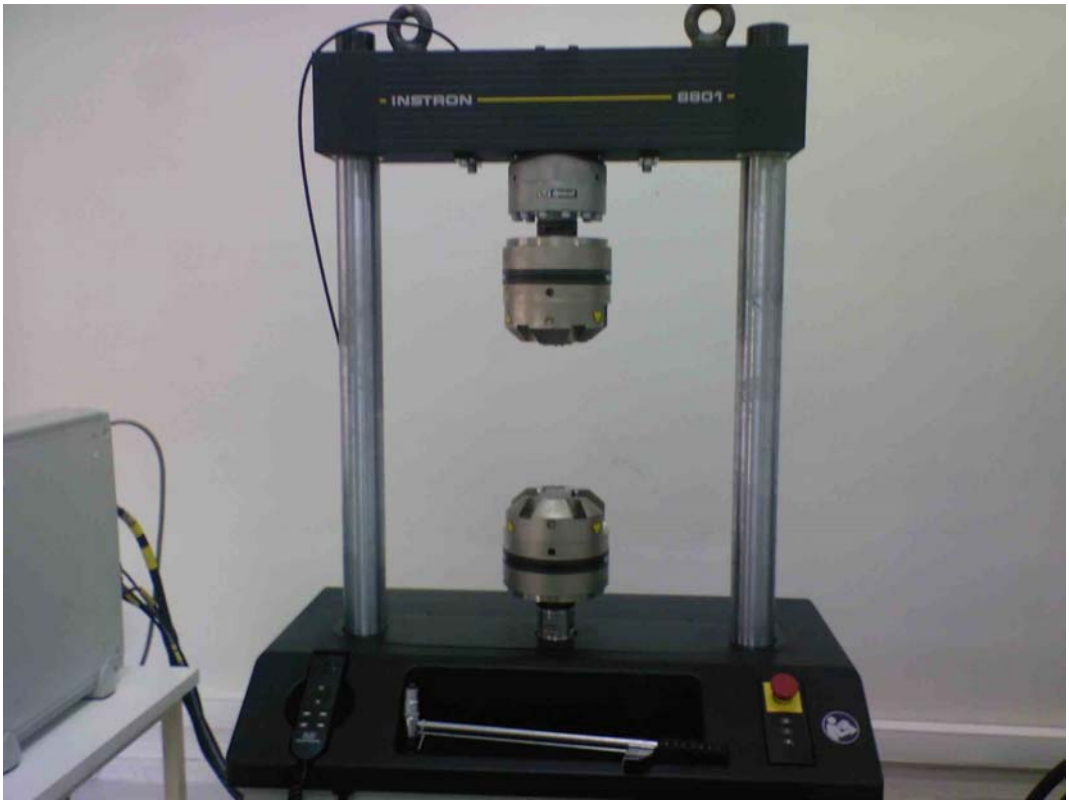

Figure 2.15. Instron 8801 servohydraulic testing machine

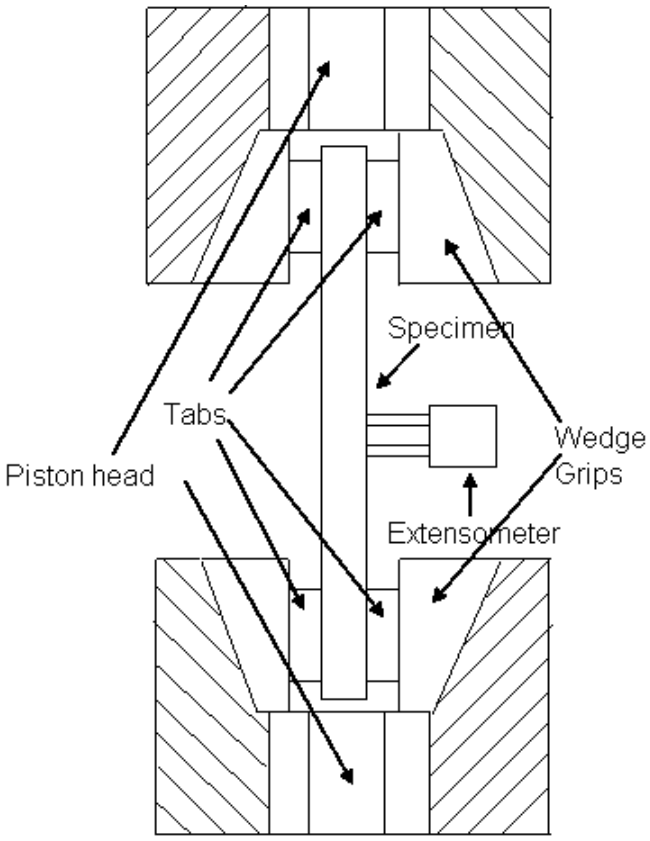

Figure 2.16. Sketch of the experimental setup of the tensile testing

2.4.1. Procedure for the Tensile Testing of the Composites

After edges of all specimens were ground with sand papers, thickness and width values of each specimen were measured on both ends and on the middle of the specimen where values found were averaged to determine the nominal values. These nominal values are then entered into Bluehill software that works in coordination with the testing equipment which computes the nominal areas of each specimen by multiplying the thickness and width. In all tensile testing, specimen to be tested was fitted to the grips of the testing machine with reinforcement of tabs made by wrapping coarse emery papers as testing standard points out. Later, extensometer was mounted on the specimen as presented in Figure 2.17.

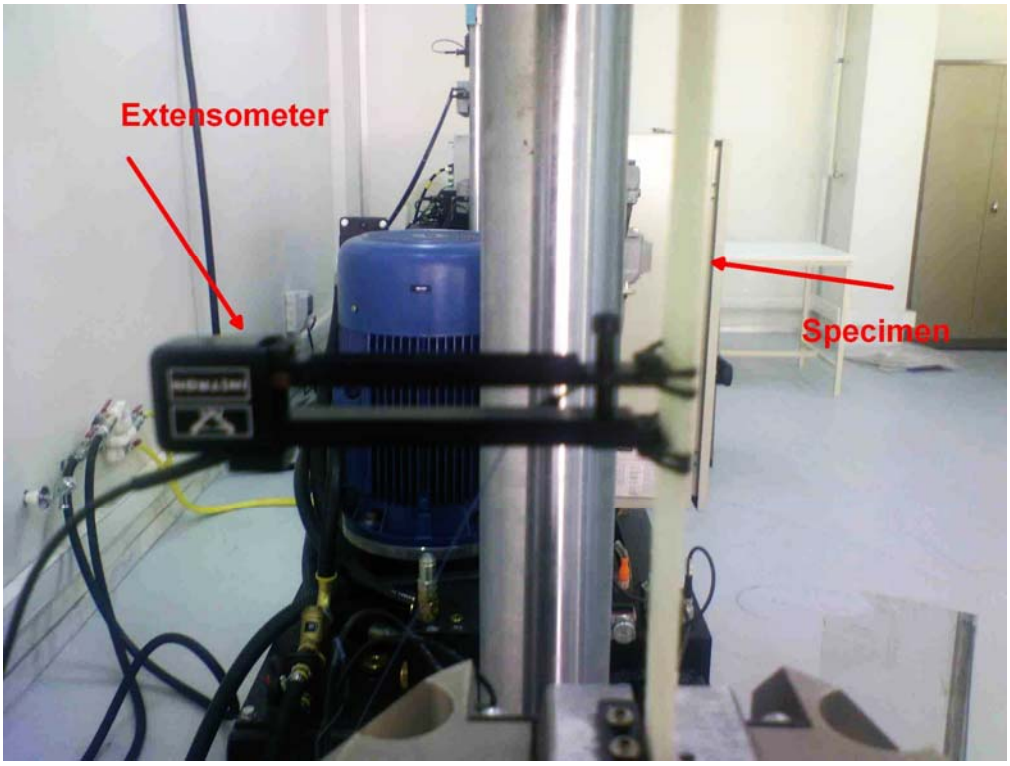

Figure 2.17. Extensometer mounted on the specimen

After the testing machine runs and the specimen breaks, Bluehill software writes the load, extension, axial strain, tensile stress values in terms of 0.1 s time intervals. All these data are later collated and used in the determination and the calculation of critical tensile strength, modulus and strain values, which will be discussed in the next chapter.

During all the tensile tests, a quiet popping sound was heard even at relatively low loads, which probably corresponds to micro-failures such as matrix cracking and fiber debonding. The final failure was accompanied by a single or multiple loud snapping sound. A failed specimen ($[\pm 45]_{2s}$) is presented in Figure 2.18.

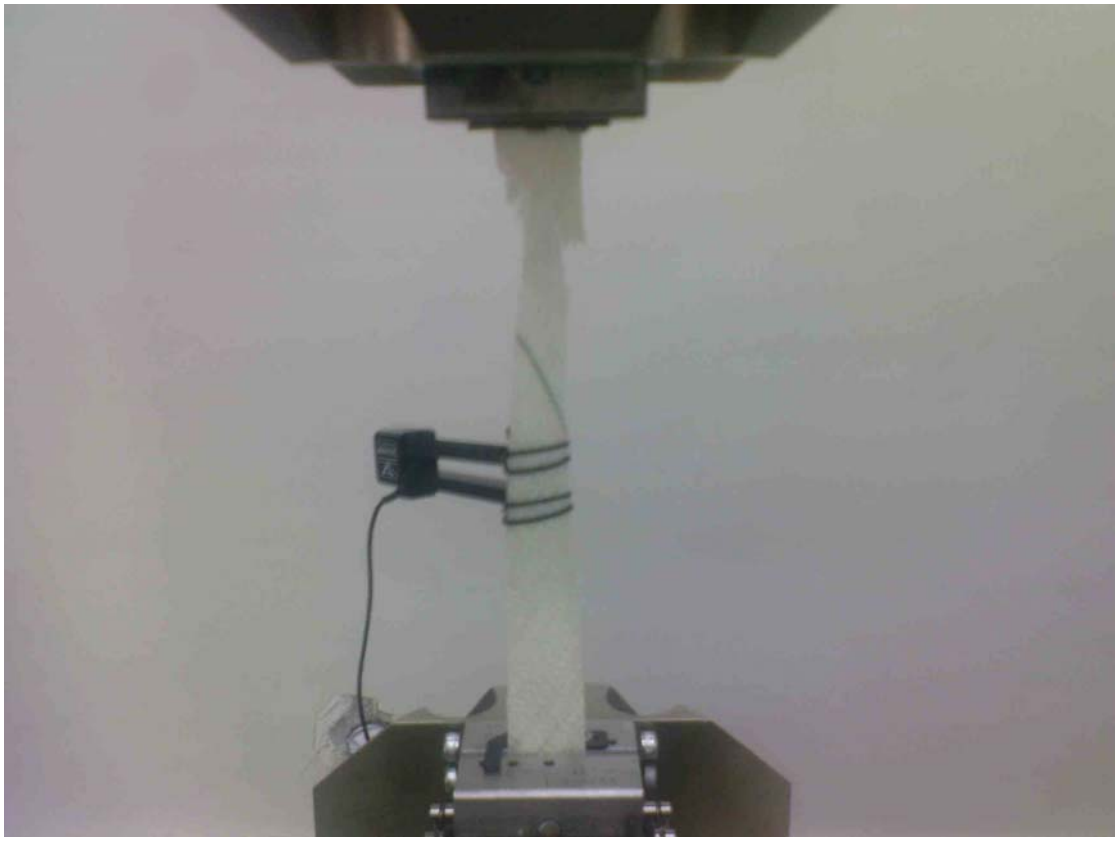

Figure 2.18. A failed specimen ($[0/90]_{2s}$ loaded in 45^{o} direction) after tensile test

Although NCF composites are more resistant to delamination than traditional woven fabric composites, delamination is still often observed in the failed specimens. Yarns in a woven fabric are crimped and follow out-of-plane undulations. Delamination occurs when the yarns are being straightened, forming a checkerboard pattern on the surface. The cause of delamination in NCF composites, on the other hand, is mainly interlaminar shear, similar to a pre-preg laminate [12].

At the end of the mechanical testing, a total number of 75 specimens were tested in tension where 5 specimens were used for each stacking sequence that was listed in Table 2.4, not taking into consideration those, if any, which were spoiled during the test and then disposed of. In addition to these, tensile failure modes and codes for the breakage type of

each specimen were noted down according to ASTM D 3039/D 3039M [22] which are shown in Figure 2.19.

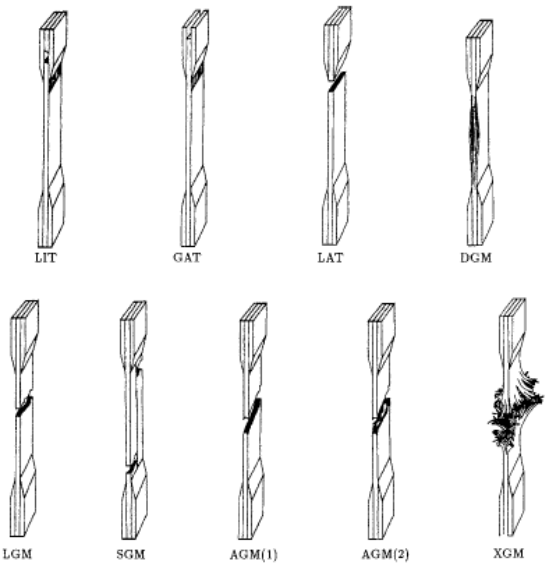

First Character

Failure Type	Code
Angled	A
edge Delamination	D
Grip/tab	G
Lateral	L
Multi-mode	M(xyz)
long. Splitting	S
eXplosive	X
Other	O

Second Character

Failure Area	Code
Inside grip/tab	I
At grip/tab	A
<1W from grip/tab	W
Gage	G
Multiple areas	M
Various	V
Unknown	U

Third Character

Failure Location	Code
Bottom	B
Top	T
Left	L
Right	R
Middle	M
Various	V
Unknown	U

Figure 2.19. Tensile test failure codes/typical modes [22]

2.5. Determination of the Volume Fractions of Fiber, Matrix and Void

Determination of the volume fractions of fiber, matrix and void in all five different thickness specimens (three of them with biaxial fabric – 2 plies, 4 plies and 8 plies, two of them with quadriaxial fabrics – 2 plies, 4 plies) was completed in Arçelik Çayırova facility as per ASTM D 3171 test method [23].

The specimen to be used in this method should have a mass of more than 1 g to obtain void content as well as fiber and matrix contents; two specimens were used for each thickness where average of the obtained values were calculated to end up with nominal values. Firstly, each specimen's density is calculated in accordance with Equation (2.1).

$$d_s = m_s / V_s \tag{2.1}$$

where d_s is the density of the specimen, m_s is the mass of the specimen found by weighing the specimen and V_s is the volume of the specimen which is found by immersing it just into a cup full of water and reading volume increase.

Later, each specimen is placed in distinct desiccated preweighed crucibles with a mass of m_c, which is cleaned in advance by heating to 500°C to 600°C in a muffle furnace and cooling in a desiccator before weighing. Then, crucibles are situated into a preheated furnace as seen in Figure 2.20 and are heated to 600°C and maintained at that temperature until the matrix completely burns off and only the fibers remain, as seen in Figure 2.21. Afterwards, crucible with specimen inside is placed in a desiccator and allowed to cool to room temperature.

Figure 2.20. Crucibles placed in the muffle furnace

Figure 2.21. Complete burn off of the matrix resulting in only fibers remaining

Then, the crucibles are placed in a desiccator and are allowed to cool down to room temperature. Afterwards, crucibles are weighed again to be able to calculate the mass of the fibers and the matrix which are then used to find volume fractions of fibers, matrix and void through the usage of the following equations:

$$m_m = m_s + m_c - m_{cf} \tag{2.2}$$

$$m_f = m_s - m_m \tag{2.3}$$

$$V_f = (m_f / m_s) \times 100 \times (d_s / d_f) \tag{2.4}$$

$$V_m = (m_r / m_s) \times 100 \times (d_s / d_m) \tag{2.5}$$

$$V_v = 100 - (V_f + V_m) \tag{2.6}$$

where m_s is the mass of specimen, m_c is the mass of crucible, m_{cf} is the mass of crucible with fibers inside after burn off, m_f is the mass of fibers, m_m is the mass of matrix, V_f is the volume fraction per cent of fibers, V_m is the volume fraction per cent of matrix, V_v is the volume fraction per cent of void, d_s is the density of the specimen, d_f is the density of the fiber, d_m is the density of the matrix.

2.6. Specimen Preparation for Micrograph Imaging

Firstly, specimens are cut off with water cooled diamond saw in desired dimensions. Then, mould into which specimen will be placed is waxed so that specimen does not adhere to the mould. Afterwards, specimen is placed into the mould and epoxy resin is poured into the mould. In this work, Buehler epo-thin resin 10 is used as the epoxy and Buehler epo-thin hardener 4 is used as the hardener. Upon awaiting 24 hours for the epoxy to completely solidify, mould is removed and specimen is ready for abrasion of its surface.

Later, 80, 180, 240, 400, 600 and 1200 grit emery papers are used in ascending order for at least 15 minutes each to grind the specimen surface. During this operation, water is applied to reduce friction. Afterwards, while keeping the specimen on a rotating turntable, Buehler metadi monocrystalline suspensions with 3 μm particles and 1 μm particles are applied on 8" microcloth PSA pad, each for 10 minutes. Later, this pad is removed, Buehler mastertex 8" pad is placed on the turntable and Buehler masterprop – polishing suspension with 0.05 μm is applied until all plies are completely visible under microscope.

Figure 2.22 through Figure 2.24 are micrographs depicting plies, matrix and voids in various laminates manufactured in this work.

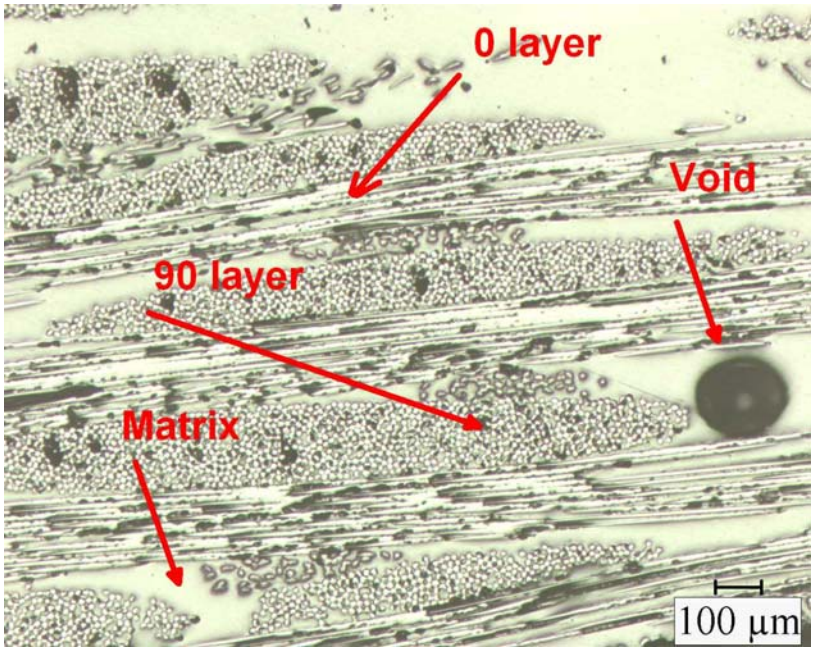

Figure 2.22 Micrograph of $[0/90]_{4s}$ specimen

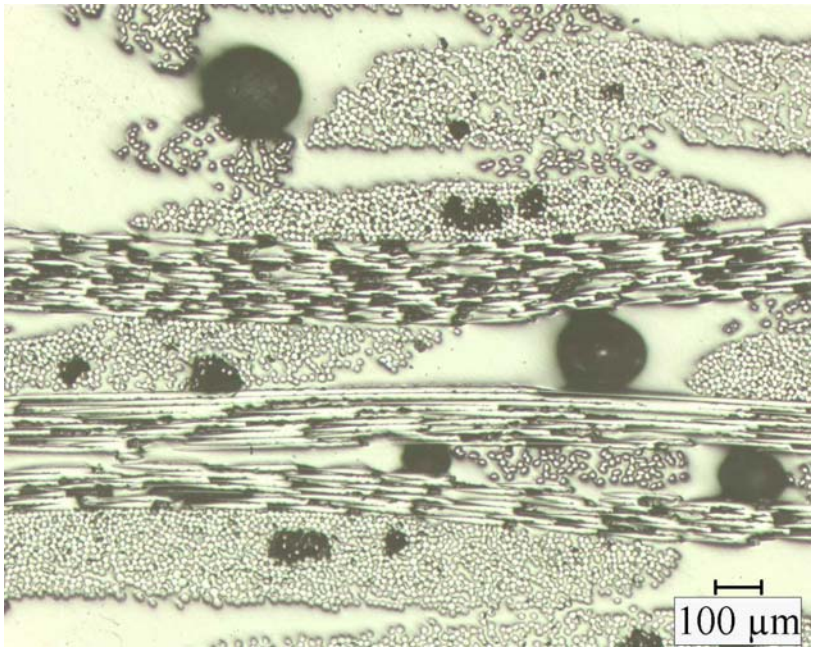

Figure 2.23. Micrograph of $[90/0]_{4s}$ specimen showing high fraction of void

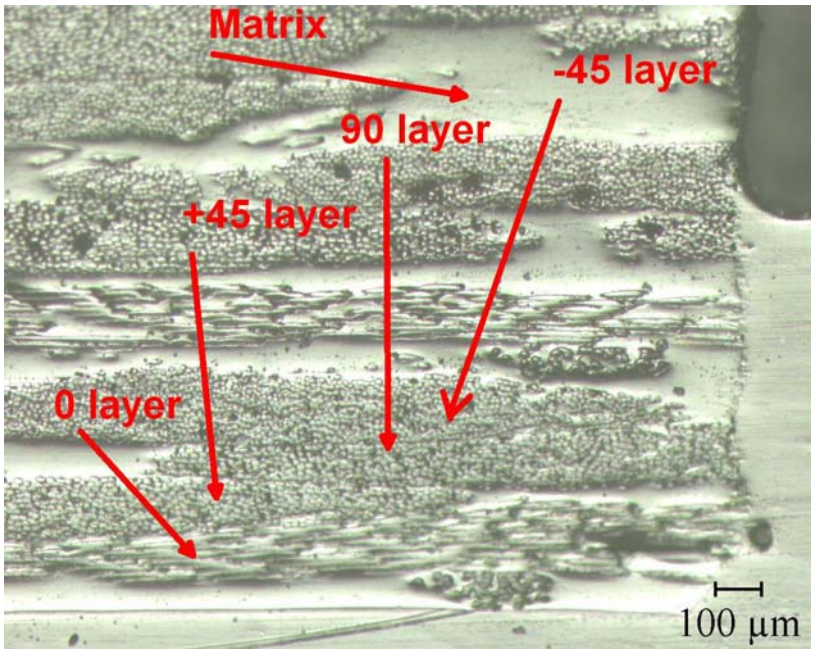

Figure 2.24. Micrograph of quadriaxial specimen

3. RESULTS AND DISCUSSION

In this chapter, results of the tensile tests on the specimens of distinct stacking sequences and fiber materials which were manufactured through VIP are presented. The comparison of the results with those predicted by micromechanical and macromechanical theories and calculation of reliability factor are also added. After tensile test of any specimen is finished, the resultant values are obtained with by the help of computer software and when the stress-strain curve is plotted accordingly, a typical graph is acquired as demonstrated in Figure 3.1.

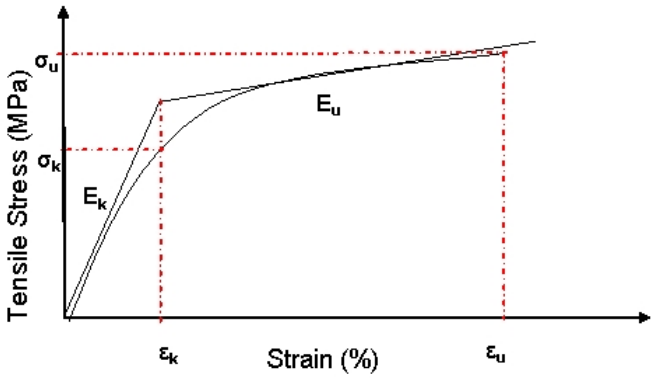

Figure 3.1. A typical stress-strain graph for the tensile test specimens

In Figure 3.1, σ_u, ε_u and E_k are automatically given by the software where E_k is the elastic modulus before knee point calculated using tangent modulus method where the instantaneous rate of change of stress as a function of strain is found, σ_u is the ultimate tensile stress which the software calculates by dividing the ultimate failure load by area of the specimen and ε_u is the ultimate tensile stress which the software notes when the complete failure occurs; σ_k, ε_k and E_u are calculated using linear regression analysis upon the resulting data where σ_k is the knee tensile stress, ε_k is the knee tensile strain, E_u is the Young's modulus after knee point till failure. Knee point is associated with the formation of well-defined transverse cracks [1] and characterizes a transient region between linear regions in the stress-strain curve due to cracking of different layers.

In this work, E_k, E_u, σ_k, σ_u, ε_k, ε_u and ultimate tensile load F_u for the tested specimens are theoretically predicted which will be explained later in this chapter

3.1. Calculated Fiber, Resin and Void Volume Fractions of the Laminates

Calculated average fractions and average values for fiber, resin and void volume fractions of the laminates to be used in prediction calculations are tabulated in Table 3.1.

Table 3.1. Volume fractions and average values

Fraction Calculation			1	2	Average
Biaxial	1s	$\mathbf{V_f}$	39.81	40	**39.90**
		$\mathbf{V_m}$	54.23	53.85	**54.04**
		$\mathbf{V_v}$	5.96	6.15	**6.06**
	2s	$\mathbf{V_f}$	41.81	41.97	**41.89**
		$\mathbf{V_m}$	52.49	52.17	**52.33**
		$\mathbf{V_v}$	5.70	5.86	**5.78**
	4s	$\mathbf{V_f}$	46.93	46.01	**46.47**
		$\mathbf{V_m}$	43.58	45.45	**44.51**
		$\mathbf{V_v}$	9.50	8.54	**9.02**
Quadriaxial	1s	$\mathbf{V_f}$	47.31	47.08	**47.20**
		$\mathbf{V_m}$	47.15	47.62	**47.38**
		$\mathbf{V_v}$	5.54	5.30	**5.42**
	2s	$\mathbf{V_f}$	46.88	47.53	**47.20**
		$\mathbf{V_m}$	46.48	45.16	**45.82**
		$\mathbf{V_v}$	6.64	7.31	**6.98**

These average fiber volume fractions are assumed to be average of volume fractions of fibers in lamina and effective fiber volume fraction of each lamina is directly proportional to area weights of fibers it contains.

Thus, for LT300 E10A fabric,

$$(V_f^{0} + V_f^{90})/2 = V_f \tag{3.1}$$

$$V_f^{0} = (161/142) * V_f^{90} \tag{3.2}$$

For LT300 E10B fabric,

$$(V_f^{0} + V_f^{90})/2 = V_f \tag{3.3}$$

$$V_f^0=(177/142)*V_f^{90} \tag{3.4}$$

For Q625 E10C fabric,

$$(V_f^0+ V_f^{+45}+ V_f^{90}+ V_f^{-45})/4 =V_f \tag{3.5}$$

$$\frac{V_f^0}{177}=\frac{V_f^{+45}}{150}=\frac{V_f^{90}}{154}=\frac{V_f^{-45}}{150} \tag{3.6}$$

where V_f^0 is the fiber volume fraction of laminae containing longitudinal fibers in each fabric, V_f^{90} is the fiber volume fraction of laminae containing transverse fibers in each fabric, V_f^{+45} is the fiber volume fraction of laminae containing fibers with $+45^o$ direction in each fabric, V_f^{-45} is the fiber volume fraction of laminae containing fibers with -45^o direction in each fabric and V_f is the fiber volume fraction for any given fabric.

After calculations are carried out, effective fiber volume fractions of each laminae are found as listed in Table 3.2.

Table 3.2. Effective fiber volume fractions of each laminae and laminate dimensions

Effective Vf (per cent) & dimensions (mm)								
Fabric	LT300 E10A				LT300 E10B			
Ply	0	90	t	w	0	90	t	w
1s	42.4	37.4	0.76	24.9	-	-	-	-
2s	44.5	39.3	1.36	25.1	-	-	-	-
4s	-	-	-		51.6	41.4	2.6	25.2
Fabric	Q625 E10C							
Ply	0	45	90	-45	t		w	
1s	53	44.9	46.1	44.9	1.27		24.79	
2s	53	44.9	46.1	44.9	2.42		24.84	

From now on, whenever V_f is involved in calculations, effective fiber volume fractions for each lamina tabulated in Table 3.2 will be used.

3.2. Elastic Modulus Prediction – Halpin - Tsai Model

Elastic moduli of each composite lamina will be predicted applying Halpin-Tsai model which contains the following equations.

$$E_x = E_f V_f + E_m V_m \tag{3.7}$$

$$\nu_{xy} = \nu_f V_f + \nu_m V_m \tag{3.8}$$

$$E_y = E_m \left(\frac{1 + \xi \eta_E V_f}{1 - \eta_E V_f} \right) \tag{3.9}$$

$$G_{xy} = G_m \left(\frac{1 + \xi \eta_G V_f}{1 - \eta_G V_f} \right) \tag{3.10}$$

where

$$\eta_E = \left(\frac{\frac{E_f}{E_m} - 1}{\frac{E_f}{E_m} + \xi} \right) \tag{3.11}$$

$$\eta_G = \left(\frac{\frac{G_f}{G_m} - 1}{\frac{G_f}{G_m} + \xi} \right) \tag{3.12}$$

in which E_x is the longitudinal modulus, E_y is transverse modulus, E_f is the fiber modulus, E_m is the matrix modulus, G_{xy} is the fiber shear modulus, G_f is the fiber shear modulus, G_m is the matrix shear modulus, ν_{xy} is Poisson's ratio for x-y direction, ν_f is fiber Poisson's ratio, ν_m is matrix Poisson's ratio and ξ is a measure of fiber reinforcement of the composite material that depends on the fiber geometry, regularity and loading.

ξ is taken as equal to 2 in calculation of the composite transverse modulus and taken as equal to 1 in calculation of the composite shear modulus for square arrays of circular fibers as is the case for the scope of this work. It is shown that when $\xi=\infty$, Equation (3.9) and Equation (3.10) reduce to Equation (3.7) type and when $\xi=0$, Equation (3.9) and Equation (3.10) reduce to the inverse rule of mixtures that are characterized by Equation (3.13) and Equation (3.14) [2].

$$\frac{1}{E_y} = \frac{V_f}{E_f} + \frac{V_m}{E_m} \tag{3.13}$$

$$\frac{1}{G_{xy}} = \frac{V_f}{G_f} + \frac{V_m}{G_m} \tag{3.14}$$

3.3. Classical Lamination Theory (CLT)

Classical lamination theory (CLT) is applied to find the relation between stresses and strains (hence the modulus, namely E_k, E_u in this work) acting on a laminate containing various laminae of distinct stacking sequences and distinct thicknesses. Using this theory, any type of laminates, whether symmetric or nonsymmetric, can be analyzed whose arbitrarily oriented plies may have various coupling effects which may lead to complex combinations of extensional, flexural and torsional deformations. The most important limitation of the CLT is that each ply is assumed to be in a state of plane stress and that interlaminar stresses are neglected.

Although the laminate is made up of multiple laminae, it is supposed that the individual laminae are perfectly bonded together so as to behave as a unitary, nonhomogeneous, anisotropic plate. Interfacial slip is not allowed and the interfacial bonds are not allowed to deform in shear, which means that displacements across lamina interfaces are assumed to be homogeneous.

Figure 3.2 defines the coordinate system to be used in developing CLT analysis. The *xyz* coordinate system is assumed to have its origin on the middle surface of the plate, so

that the middle surface lies in the *xy* plane. The displacements at a point in the *x*, *y*, *z* directions are *u*, *v*, *w*, respectively.

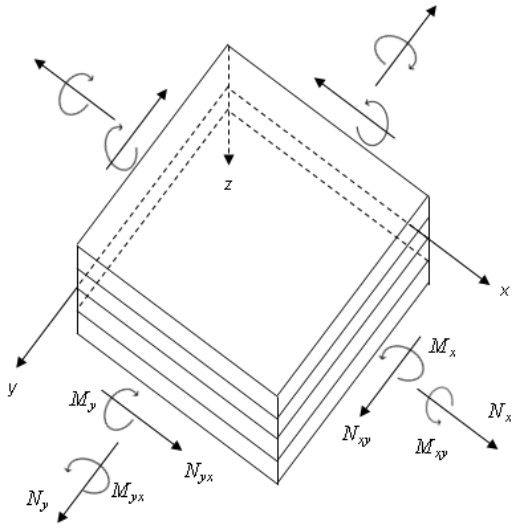

Figure 3.2. Coordinate system and stress resultants for a laminate in CLT

The basic assumptions relevant to CLT are listed below [1]:

1. The plate consists of orthotropic laminae bonded together, with the principal material axes of the orthotropic laminae oriented along arbitrary directions with respect to xy axes.

2. The thickness of the plate, *t*, is much smaller than the lengths along the plate edges, a and b.

3. The displacements *u*, *v*, and *w* are small compared with the plate thickness.

4. The in-plane strains ε_x, ε_y, γ_{xy} are small compared with unity.

5. Transverse shear strains γ_{xz} and γ_{yz} are negligible.

6. Tangential displacements *u* and *v* are linear functions of the *z* coordinate.

7. The transverse normal strain ε_k is negligible.

8. Each ply obeys Hookes's law.

9. The plate thickness t is constant.

10. Shear stresses τ_{xz} and τ_{yz} vanish on the plate surfaces defined by $z = \pm t/2$.

The stiffness matrix for a specially orthotropic lamina loaded in principal directions is given as follows:

$$\begin{bmatrix} \sigma_x \\ \sigma_y \\ \tau_{yx} \end{bmatrix} = \begin{bmatrix} Q_{11} & Q_{12} & 0 \\ Q_{21} & Q_{22} & 0 \\ 0 & 0 & Q_{66} \end{bmatrix} \begin{bmatrix} \varepsilon_x \\ \varepsilon_y \\ \gamma_{xy} \end{bmatrix} \tag{3.15}$$

where Q_{ij} are the components of the lamina stiffness matrix, which are related to the engineering constants by the following equations:

$$Q_{11} = \frac{E_x}{1 - \nu_{xy}\nu_{yx}} \tag{3.16}$$

$$Q_{12} = \frac{\nu_{xy}E_y}{1 - \nu_{xy}\nu_{yx}} = Q_{21} \tag{3.17}$$

$$Q_{22} = \frac{E_y}{1 - \nu_{xy}\nu_{yx}} \tag{3.18}$$

$$Q_{66} = \frac{1}{G_{xy}} \tag{3.19}$$

in which ν_{yx} is the Poisson's ratios for y-x direction found by the following equation:

$$\nu_{xy} = \frac{\nu_{xy}E_y}{E_x} \tag{3.20}$$

The stiffness matrix for a specially orthotropic lamina of an arbitrary orientation (shown in Figure 3.3) is as follows:

$$\begin{bmatrix} \sigma_x \\ \sigma_y \\ \tau_{yx} \end{bmatrix} = \begin{bmatrix} \overline{Q}_{11} & \overline{Q}_{12} & \overline{Q}_{16} \\ \overline{Q}_{12} & \overline{Q}_{22} & \overline{Q}_{26} \\ \overline{Q}_{16} & \overline{Q}_{26} & \overline{Q}_{66} \end{bmatrix} \begin{bmatrix} \varepsilon_x \\ \varepsilon_y \\ \gamma_{xy} \end{bmatrix} \tag{3.21}$$

where $\overline{Q}_{ij}$ are the components of the transformed lamina stiffness matrix, which are defined as in follow equations:

$$\overline{Q}_{11} = Q_{11}\cos^4\theta + Q_{22}\sin^4\theta + 2(Q_{12} + Q_{66})\sin^2\theta\cos^2\theta \tag{3.22}$$

$$\overline{Q}_{12} = (Q_{11} + Q_{22} - 4Q_{66})\sin^2\theta\cos^2\theta + Q_{12}(\cos^4\theta + \sin^4\theta) \tag{3.23}$$

$$\overline{Q}_{22} = Q_{11}\sin^4\theta + Q_{22}\cos^4\theta + 2(Q_{12} + Q_{66})\sin^2\theta\cos^2\theta \tag{3.24}$$

$$\overline{Q}_{16} = (Q_{11} - Q_{12} - 2Q_{66})\cos^3\theta\sin\theta - (Q_{22} - Q_{12} - 2Q_{66})\cos\theta\sin^3\theta) \tag{3.25}$$

$$\overline{Q}_{26} = (Q_{11} - Q_{12} - 2Q_{66})\cos\theta\sin^3\theta - (Q_{22} - Q_{12} - 2Q_{66})\cos^3\theta\sin\theta) \tag{3.26}$$

$$\overline{Q}_{66} = (Q_{11} + Q_{22} - 2Q_{12} - 2Q_{66})\sin^2\theta\cos^2\theta + Q_{66}(\cos^4\theta + \sin^4\theta) \tag{3.27}$$

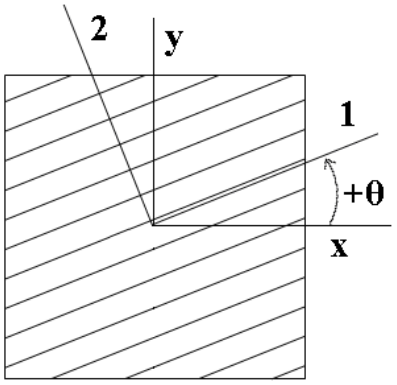

Figure 3.3. Sign convention for lamina orientation

From the stress-strain Equation (3.21), the stresses in the k[th] layer can be expressed in terms of the laminate middle-surface strains and curvatures as

$$\begin{bmatrix} \sigma_x \\ \sigma_y \\ \tau_{yx} \end{bmatrix}_k = \begin{bmatrix} \overline{Q}_{11} & \overline{Q}_{12} & \overline{Q}_{16} \\ \overline{Q}_{12} & \overline{Q}_{22} & \overline{Q}_{26} \\ \overline{Q}_{16} & \overline{Q}_{26} & \overline{Q}_{66} \end{bmatrix}_k \left[\begin{bmatrix} \varepsilon_x^o \\ \varepsilon_y^o \\ \gamma_{xy}^o \end{bmatrix} + z \begin{bmatrix} \kappa_x \\ \kappa_y \\ \kappa_z \end{bmatrix} \right] \tag{3.28}$$

where z is the distance of the k[th] layer from the middle surface, κ_x is a bending curvature associated with bending of the middle surface *xz*, κ_y is a bending curvature associated with bending of the middle surface in the *yz* plane, κ_{xy} is a twisting curvature associated with out-of-plane twisting of the middle surface, which lies in the *xy* plane before deformation all of which are characterized by the following equations:

$$\kappa_x = -\frac{\partial^2 w}{\partial x^2} \tag{3.29}$$

$$\kappa_x = -\frac{\partial^2 w}{\partial y^2} \tag{3.30}$$

$$\kappa_x = -2\frac{\partial^2 w}{\partial x \partial y} \tag{3.31}$$

and ε_x^o, ε_y^o and γ_{xy}^o are middle surface strains found by following equations:

$$\varepsilon_x^o = \frac{\partial u^o}{\partial x} \tag{3.32}$$

$$\varepsilon_y^o = \frac{\partial v^o}{\partial y} \tag{3.33}$$

$$\gamma_{xy}^o = \frac{\partial u^o}{\partial y} + \frac{\partial v^o}{\partial x} \tag{3.34}$$

where u^o and v^o are the tangential displacements of the middle surface along the *x*- and *y*-directions.

By using Equation (3.28) and definitions of N_x, the force per unit length, M_x, the moment per unit length which are characterised by the following equations:

$$N_x = \int_{-t/2}^{t/2} \sigma_x dz \tag{3.35}$$

$$M_x = \int_{-t/2}^{t/2} \sigma_x z dz \tag{3.36}$$

where t is the thickness of the laminate, which is measured prior to the tensile testing, the general expression of the CLT is obtained as follows:

$$\begin{Bmatrix} N_x \\ N_y \\ N_{xy} \\ M_x \\ M_y \\ M_{xy} \end{Bmatrix} = \begin{bmatrix} A_{11} & A_{12} & A_{16} & B_{11} & B_{12} & B_{16} \\ A_{12} & A_{22} & A_{26} & B_{12} & B_{22} & B_{26} \\ A_{16} & A_{26} & A_{66} & B_{16} & B_{26} & B_{66} \\ B_{11} & B_{12} & B_{16} & D_{11} & D_{12} & D_{16} \\ B_{12} & B_{22} & B_{26} & D_{12} & D_{22} & D_{26} \\ B_{16} & B_{26} & B_{66} & D_{16} & D_{26} & D_{66} \end{bmatrix} \begin{Bmatrix} \varepsilon_x^o \\ \varepsilon_y^o \\ \gamma_{xy}^o \\ \kappa_x^o \\ \kappa_y^o \\ \kappa_{xy}^o \end{Bmatrix} \tag{3.37}$$

or simply

$$\begin{Bmatrix} N \\ \hline M \end{Bmatrix} = \left[\begin{array}{c|c} A & B \\ \hline B & D \end{array}\right] \begin{Bmatrix} \varepsilon^o \\ \kappa \end{Bmatrix} \tag{3.38}$$

where

$$N = \begin{Bmatrix} N_x \\ N_y \\ N_{xy} \end{Bmatrix} \tag{3.39}$$

$$M = \begin{Bmatrix} M_x \\ M_y \\ M_{xy} \end{Bmatrix} \tag{3.40}$$

$$A = \begin{bmatrix} A_{11} & A_{12} & A_{16} \\ A_{12} & A_{22} & A_{26} \\ A_{16} & A_{26} & A_{66} \end{bmatrix} \tag{3.41}$$

$$B = \begin{bmatrix} B_{11} & B_{12} & B_{16} \\ B_{12} & B_{22} & B_{26} \\ B_{16} & B_{26} & B_{66} \end{bmatrix} \tag{3.42}$$

$$D = \begin{bmatrix} D_{11} & D_{12} & D_{16} \\ D_{12} & D_{22} & D_{26} \\ D_{16} & D_{26} & D_{66} \end{bmatrix} \tag{3.43}$$

$$\varepsilon^o = \begin{bmatrix} \varepsilon_x^o \\ \varepsilon_y^o \\ \varepsilon_{xy}^o \end{bmatrix} \tag{3.44}$$

$$\kappa = \begin{bmatrix} \kappa_x \\ \kappa_y \\ \kappa_{xy} \end{bmatrix} \tag{3.45}$$

where

$$A_{ij} = \int_{-t/2}^{t/2} (\overline{Q}_{ij}) dz \tag{3.46}$$

$$B_{ij} = \int_{-t/2}^{t/2} (\overline{Q}_{ij}) z dz \tag{3.47}$$

$$D_{ij} = \int_{-t/2}^{t/2} (\overline{Q}_{ij}) z^2 dz \tag{3.48}$$

Finally, in finding effective laminate engineering constants E_x and E_y of a specimen under uniaxial load, if A matrix is inverted to yield A' matrix which is defined as;

$$A' = A^{-1} = \begin{bmatrix} A'_{11} & A'_{12} & A'_{16} \\ A'_{12} & A'_{22} & A'_{26} \\ A'_{16} & A'_{26} & A'_{66} \end{bmatrix} \tag{3.49}$$

$$E_x = \frac{\sigma_x}{\varepsilon_x^o} = \frac{N_x / t}{A'_{11} N_x} = \frac{1}{t A'_{11}} \tag{3.50}$$

$$E_y = \frac{\sigma_y}{\varepsilon_y^o} = \frac{N_y / t}{A'_{11} N_y} = \frac{1}{t A'_{22}} \tag{3.51}$$

3.4. Strength and Strain Predictions of the Individual Laminae

Strength and the corresponding strains of the laminates using micromechanics will be theoretically predicted using micromechanics models for lamina strength in integration with maximum strain criterion, then applying first ply failure method and the ply-discount models in turn.

3.4.1. Micromechanics Models for Lamina Strength

3.4.1.1. Longitudinal Strength. For fiber failure modes which have typical stress-strain curves as illustrated in Figure 3.4 where $\varepsilon_m > \varepsilon_{f1}$ in which ε_m and ε_{f1} are the failure strains in uniaxial tension of the matrix and fiber respectively, strength of each lamina is calculated using Equation (3.52).

$$\sigma_L = \sigma_{f1} V_f + \sigma_{mf} (1 - V_f) \tag{3.52}$$

where σ_L is the ultimate longitudinal strength of lamina, σ_{f1} is the ultimate longitudinal strength of fibers, σ_{mf} is the strength of the matrix corresponding to ε_{f1}.

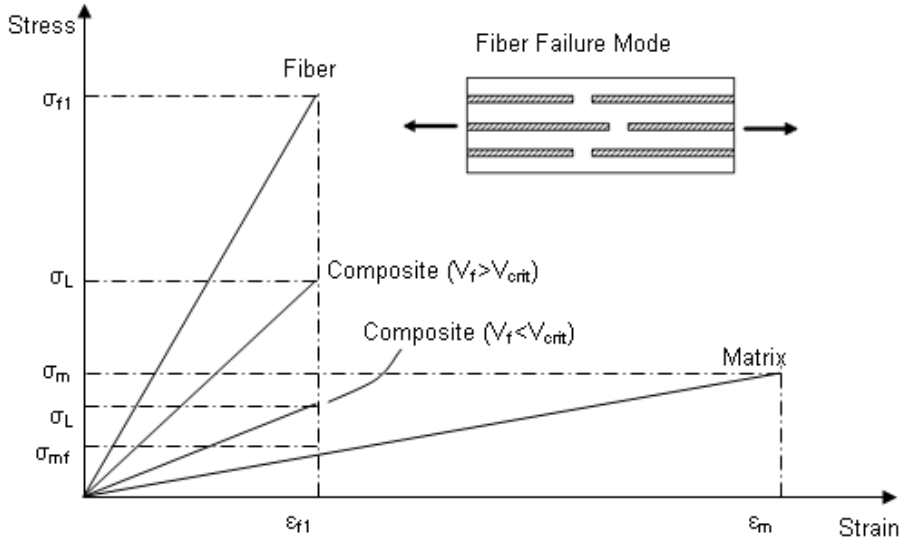

Figure 3.4. Representative stress-strain curves for typical fiber, matrix and composite materials in a fiber failure mode [1]

On the other hand, for matrix failure modes which have typical stress-strain curves as shown in Figure 3.5 where $\varepsilon_{f1}>\varepsilon_m$, strength of each lamina is found using Equation (3.53).

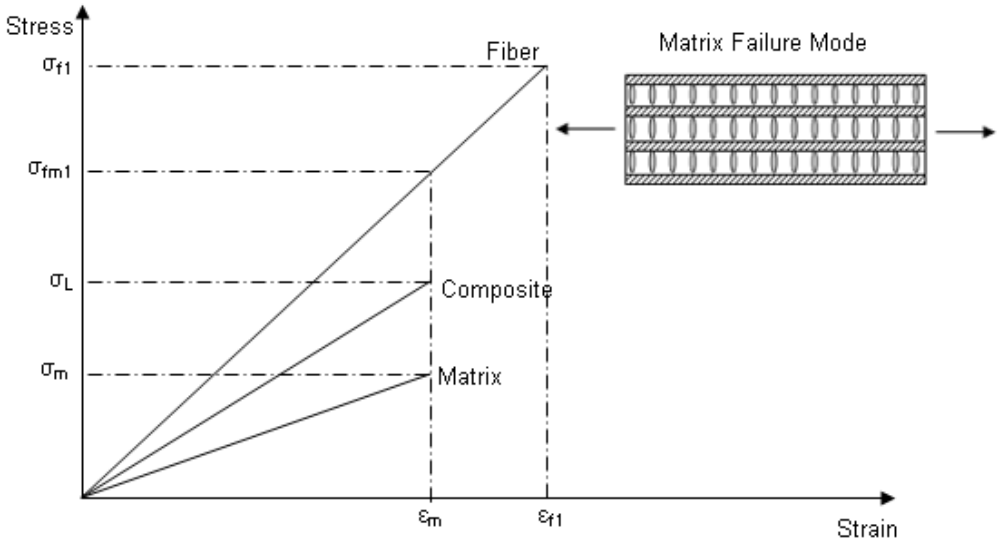

Figure 3.5. Representative stress-strain curves for typical fiber, matrix and composite materials in a matrix failure mode [1]

$$\sigma_L = \sigma_{f1} V_f \tag{3.53}$$

3.4.1.2. Transverse Strength. The transverse tensile strength of a lamina in which there is little or no interface bonding is determined by the strength of the matrix [3]. The predicted transverse strength, σ_T, provided that the matrix is not notch sensitive is given by the following equation.

$$\sigma_T = \frac{E_2 \sigma_m}{E_m F} \tag{3.54}$$

where σ_m is the ultimate strength of the matrix and F is a strain concentration factor related to the fiber volume fraction as shown in Figure 3.6 [1].

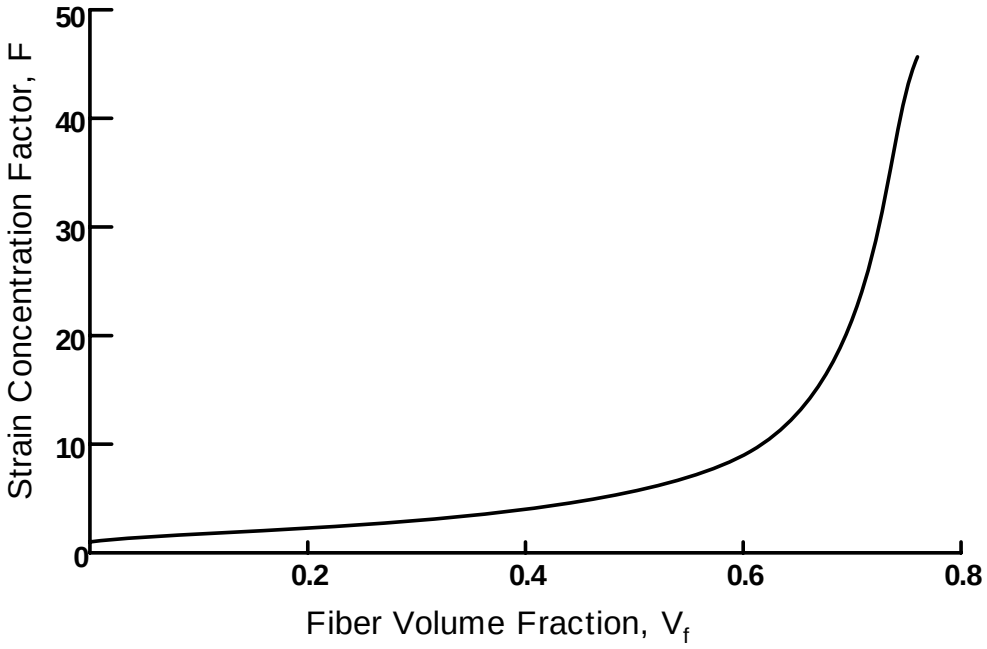

Figure 3.6. Variation of F with V_f

3.4.1.3. Shear Strength. The shear strength of a lamina is dominated by matrix properties because crack propagation can occur entirely by shear of the matrix without disturbing or fracturing the fibers. The predicted shear strength, τ_{LT} is given by the following equation:

$$\tau_{LT} = \tau_m \left[1 - 2(V_f / \pi)^{\frac{1}{2}} \right] \tag{3.55}$$

3.4.1.4 . Off-axis Uniaxial Tensile Loading . When uniaxial tensile stress, σ_x, is applied on a specimen having principal material axes as illustrated in Figure 3.3 (as in the angle-ply biaxial and quadriaxial specimens in this work), it produces the following equations for biaxial stress state:

$$\begin{aligned} \sigma_1 &= \sigma_x \cos^2\theta \\ \sigma_2 &= \sigma_x \sin^2\theta \\ \tau_{12} &= -\sigma_x \sin\theta\cos\theta \end{aligned} \tag{3.56}$$

where σ_1 is the transformed longitudinal strength, σ_2 is the transformed transverse strength, τ_{12} is the transformed shear strength.

Table 3.3 lists the elastic constants for fibers and matrix in each fabric which is used in the manufacturing of the laminates and calculated elastic constants for each lamina containing corresponding fibers accordingly.

Table 3.3 Elastic constants for fibers, matrix and laminae [1], [24], [25]

Fibers & Matrix	Biaxial E10A		Biaxial E10B		Quadriaxial Q625 E10C			
Layers	0	90	0	90	0	45	90	-45
Fiber Young's Modulus (GPa)	72.4	72.4	72.4	72.4	72.4	72.4	72.4	72.4
Fiber Shear Modulus (GPa)	26.2	26.2	26.2	26.2	26.2	26.2	26.2	26.2
Fiber Tensile Strength (GPa)	1.95	1.95	1.95	1.95	1.95	1.95	1.95	1.95
Fiber Ultimate Strain (%)	4.8	4.8	4.8	4.8	4.8	4.8	4.8	4.8
Fiber Poisson's Ratio	0.22	0.22	0.22	0.22	0.22	0.22	0.22	0.22
Matrix Young's Modulus (GPa)	3.5	3.5	3.5	3.5	3.5	3.5	3.5	3.5
Matrix Shear Modulus (GPa)	1.4	1.4	1.4	1.4	1.4	1.4	1.4	1.4
Matrix Tensile Strength (MPa)	49	49	49	49	49	49	49	49
Matrix Ultimate Strain (%)	2.0	2.0	2.0	2.0	2.0	2.0	2.0	2.0
Matrix Poisson's Ratio	0.38	0.38	0.38	0.38	0.38	0.38	0.38	0.38
Values for Laminae Made of Fibers and Matrix above								
Longitudinal Modulus (GPa)	32.6	28.9	38.9	31.5	40	34.1	35	34.1
Longitudinal Strength (MPa)	825	728	1004	805	1031	874	897	874
Transverse Modulus (GPa)	9.5	8.4	11.8	9.3	12.3	10.1	10.4	10.1
Transverse Strength (MPa)	161	165	158	163	183	157	160	157

3.4.2. Maximum Strain Criterion

Maximum strain criterion predicts failure when any principal material axis strain component exceeds the corresponding ultimate strain. In order to avoid failure according to this criterion, the following set of inequalities must be satisfied:

$$\begin{aligned} \varepsilon_x &< \varepsilon_L \\ \varepsilon_y &< \varepsilon_T \\ \left|\gamma_{xy}\right| &< \varepsilon_{LT} \end{aligned} \tag{3.57}$$

where ε_x, ε_y, γ_{xy} are the longitudinal, transverse and shear strains respectively and ε_L, ε_T and ε_{LT} are ultimate longitudinal, transverse and shear strains respectively which are found by the following equations:

$$\varepsilon_x = \frac{\sigma_x - \nu_{xy}\sigma_y}{E_x} \tag{3.58}$$

$$\varepsilon_y = \frac{\sigma_y - \nu_{yx}\sigma_x}{E_y} \tag{3.59}$$

$$\gamma_{xy} = \frac{\tau_{xy}}{G_{xy}} \tag{3.60}$$

$$\varepsilon_L = \sigma_L \big/ E_x \tag{3.61}$$

$$\varepsilon_T = \sigma_T \big/ E_y \tag{3.62}$$

$$e_{LT} = \tau_{LT} \big/ E_{xy} \tag{3.63}$$

where σ_x is the longitudinal strength, σ_y is the transverse strength, τ_{xy} is the shear strength.

3.4.3. First Ply Failure Prediction

First ply failure prediction is a straightforward application of the appropriate multiaxial lamina strength criterion in combination with the lamina stress analysis from the CLT. The loads corresponding to first ply failure are not necessarily the laminate failure loads, since a laminate generally has plies at several orientations [1]. There will usually be a sequence of ply failures at different loads culminating in ultimate laminate failure when all plies have failed. Thus, the ultimate load-carrying capacity of the laminate may be significantly higher than the first ply failure load, and prediction of laminate failure based on first ply failure may be too conservative.

In the analysis of first ply failure and subsequent ply failures methodology, the stiffness matrices for the failed plies and the corresponding laminate stiffness matrix obtained using CLT are modified after each ply failure to reflect the effects of those failures. Figure 3.7 represents a typical stress-strain curve of a biaxial $[0/90]_s$ laminate loaded in 45^o direction, showing the first ply failure and changing slopes (E_k and E_u) before and after ply failure occurs.

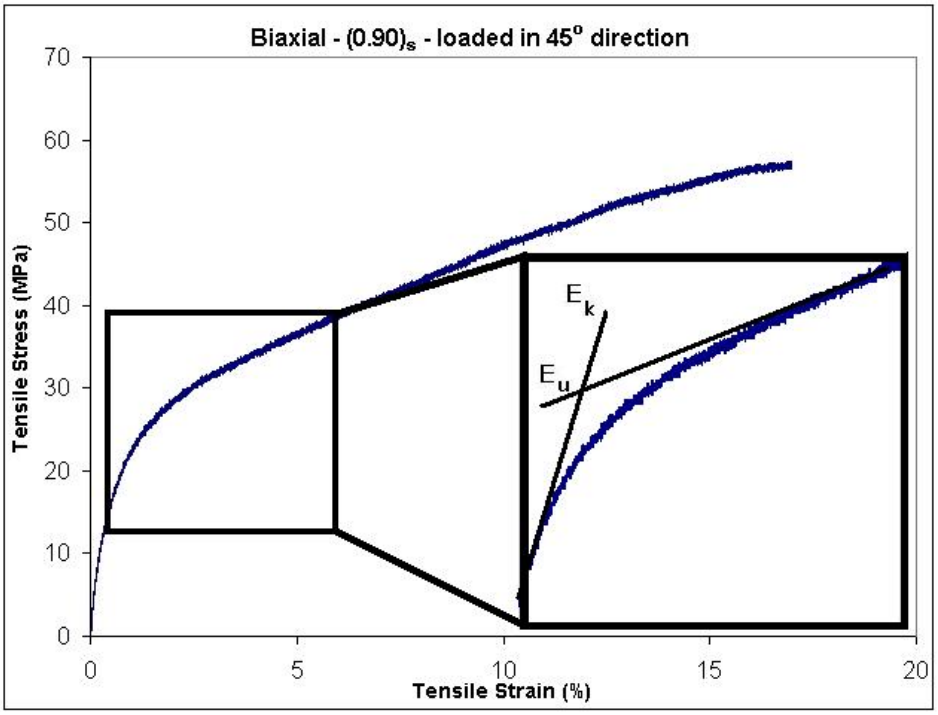

Figure 3.7. A typical stress-strain curve of a biaxial $[0/90]_s$ laminate loaded in 45^o direction, showing the first ply failure

The total forces and moments at th *k*th knee in the curve are related to the corresponding forces and moments for the *n*th section of such a curve (where $n \leq k$) by the summation

$$\begin{Bmatrix} N \\ M \end{Bmatrix}_{Total} = \sum_{n=1}^{k} \begin{Bmatrix} N^{(n)} \\ M^{(n)} \end{Bmatrix} \tag{3.64}$$

where the superscript (*n*) on a parameter denotes the particular value of that parameter associated with the *n*th section. The corresponding midplane strains and curvatures are given by

$$\begin{Bmatrix} \varepsilon^{o} \\ \kappa \end{Bmatrix}_{Total} = \sum_{n=1}^{k} \begin{Bmatrix} \varepsilon^{o(n)} \\ \kappa^{(n)} \end{Bmatrix} \tag{3.65}$$

Using the piecewise linear assumption, the load-deformation relationship for the *n*th can be approximated by modifying Equation (3.38)

$$\left\{\begin{array}{c} N^{(n)} \\ \hline M^{(n)} \end{array}\right\} = \left[\begin{array}{c|c} A^{(n)} & B^{(n)} \\ \hline B^{(n)} & D^{(n)} \end{array}\right] \begin{Bmatrix} \varepsilon^{o(n)} \\ \kappa^{(n)} \end{Bmatrix} \tag{3.66}$$

where the $[A^{(n)}]$, $[B^{(n)}]$ and $[D^{(n)}]$ are the modified stiffness matrices after the *(n-1)*th ply failure [1].

3.4.4. The Ply Discount Model

The ply discount model is based on the assumption that failed ply loses all its stiffnesses, thus stiffnesses are assigned values very close to zero. The laminate with reduced stifness is then again analyzed for stresses and strains by applying CLT, first ply failure and maximum strain criterion [26].

3.5. General Methodology for Obtaining Theoretical Predictions

The general methodology for obtaining the theoretical strength, stiffness and strain predictions of the tested specimens are listed in order in what follows:

- By using fiber and matrix elastic constants (ultimate tensile strengths, Young's moduli, shear moduli, Poisson's ratios) together with effective fiber volume fractions, matrix volume fractions and thicknesses and then by applying Halpin-Tsai equations, elastic constants of each lamina are calculated.

- After calculating components of Q matrix for each lamina, through application of CLT, components of A matrix are calculated. Then, inverse of A matrix is calculated and Ek is found by using Equation (3.50).

- By applying micromechanics models for lamina strengths, longitudinal and transverse strengths are calculated and then by applying maximum strain criterion for laminae, εk, εu and laminate failure load until knee point are found.

- By making use of the ply discount model assuming the failed ply having zero stiffness, adjusted A matrix is found, then inverse adjusted A matrix is found and then Eu is calculated.

- Then, laminate load until failure are determined, and using this value together with laminate failure load until knee point, σu and σk are found by dividing the calculated load values by the thickness of the laminate.

- By multiplying σu with measured thickness and width values of laminates, predicted ultimate load Fu is calculated.

Flowchart of the general methodology for obtaining the thoretical predictions are given in Figure 3.8.

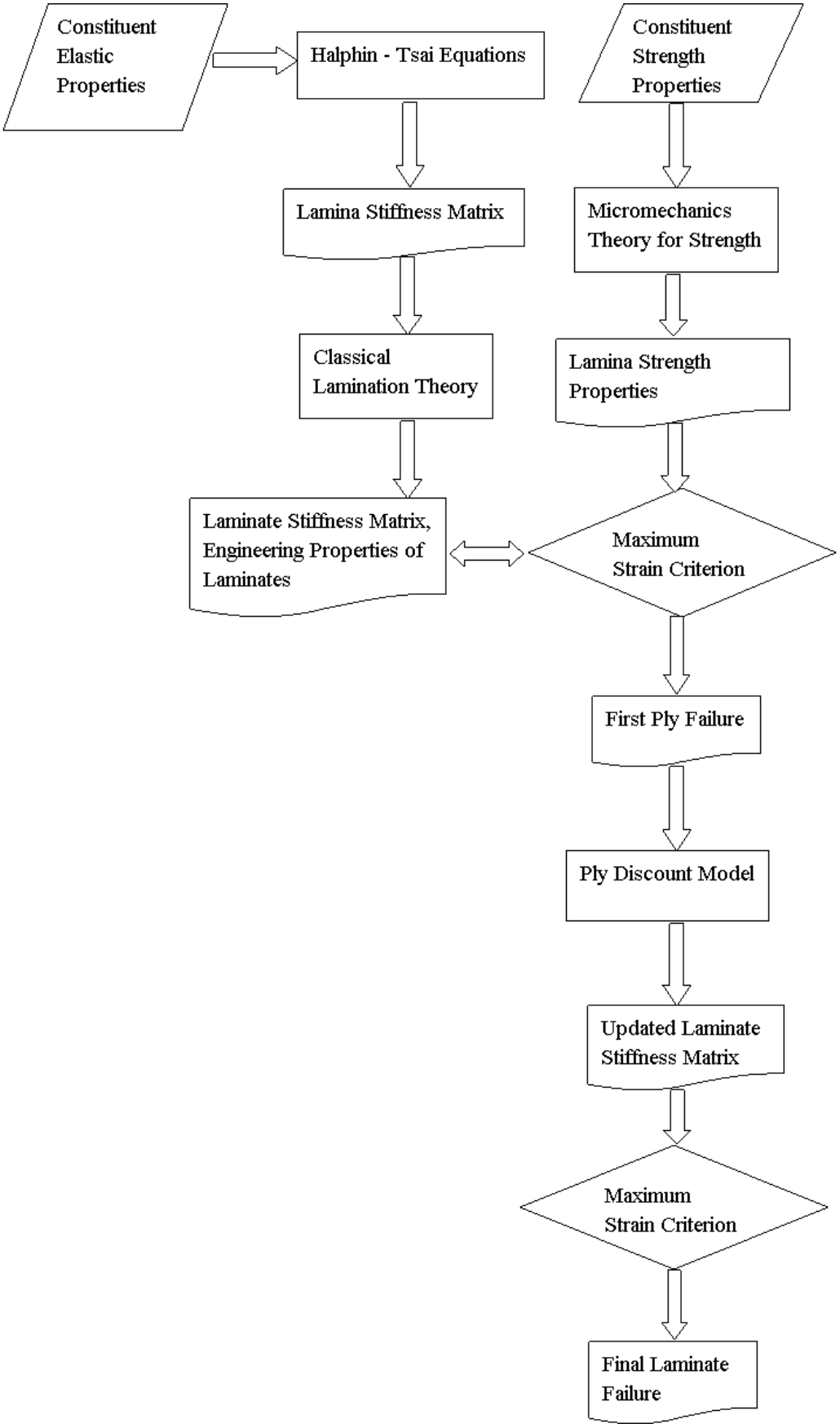

Figure 3.8. Flowchart of the general methodology for obtaining the thoretical predictions

3.6. Experimental Values vs. Theoretical Predictions

In this section, experimental statistics obtained by tensile testing of the laminates, theoretically predicted values and difference percentages are listed in Table 3.4 to Table 3.8, experimental values are graphed in Figure 3.9 to Figure 3.13 and comparison between experimental values and theoretical predictions are given in Figure 3.14 to Figure 3.20.

Table 3.4. Experimental data vs. theoretical values for 4-ply biaxial laminates

Biaxial 4-plies $[0/90]_s$								
Direction	Engineering Values	Experimental Statistics					Prediction	Difference (%)
		Avg.	Min	Max.	SD	CV (%)		
0^o – direction	σ_u(MPa)	302.63	280.38	318.31	15.00	4.96	358.68	18.52
	σ_k(MPa)	89.36	87.64	91.30	1.48	1.66	104.39	16.82
	ε_u(%)	2.49	2.33	2.62	0.14	5.81	2.54	1.97
	ε_k(%)	0.65	0.63	0.67	0.02	2.41	0.57	-12.17
	E_u(GPa)	11.96	11.59	12.23	0.24	2.02	13.88	16.04
	E_k(GPa)	14.13	13.81	14.59	0.31	2.22	16.94	19.89
	Load(kN)	5.74	5.24	6.26	0.37	6.53	6.79	18.46
45^o – direction	σ_u(MPa)	56.09	53.62	57.52	1.50	2.68	67.77	20.81
	σ_k(MPa)	18.68	18.33	19.13	0.34	1.83	22.03	17.93
	ε_u(%)	15.40	13.61	16.98	1.25	8.11	16.32	6.00
	ε_k(%)	0.71	0.66	0.74	0.03	4.40	0.61	-13.48
	E_u(GPa)	0.22	0.20	0.24	0.01	6.82	0.26	21.37
	E_k(GPa)	4.13	3.79	4.50	0.25	6.14	5.05	22.22
	Load(kN)	1.06	1.06	1.07	0.00	0.31	1.27	19.59
90^o – direction	σ_u(MPa)	214.75	202.44	221.15	7.17	3.34	246.82	14.93
	σ_k(MPa)	63.05	59.64	67.09	3.48	5.51	74.91	18.81
	ε_u(%)	2.02	1.86	2.13	0.12	5.80	2.52	24.52
	ε_k(%)	0.52	0.47	0.55	0.03	5.57	0.51	-2.79
	E_u(GPa)	10.19	9.67	10.86	0.48	4.68	11.31	10.95
	E_k(GPa)	12.88	12.27	13.25	0.40	3.09	15.08	17.10
	Load(kN)	4.11	3.86	4.20	0.14	3.36	4.73	15.15

Table 3.5. Experimental data vs. theoretical values for 8-ply biaxial laminates

Biaxial 8-plies $[0/90]_{2s}$								
Direction	Engineering Values	Experimental Statistics					Prediction	Difference (%)
		Avg.	Min	Max.	SD	CV (%)		
0^o – direction	σ_u(MPa)	356.98	344.81	368.40	10.17	2.85	418.95	17.36
	σ_k(MPa)	98.72	96.17	101.06	2.06	2.09	118.13	19.66
	ε_u(%)	2.77	2.52	3.03	0.20	7.05	2.55	-8.11
	ε_k(%)	0.65	0.63	0.69	0.02	3.50	0.55	-16.34
	E_u(GPa)	12.72	11.98	13.23	0.49	3.89	14.34	12.78
	E_k(GPa)	15.52	15.00	16.21	0.57	3.67	17.89	15.30
	Load(kN)	12.30	11.81	12.67	0.35	2.88	14.45	17.43
45^o – direction	σ_u(MPa)	70.98	68.76	72.11	1.41	1.99	83.55	17.72
	σ_k(MPa)	25.15	23.57	26.71	1.20	4.77	29.50	17.31
	ε_u(%)	17.39	15.93	18.16	0.87	4.99	16.62	-4.44
	ε_k(%)	0.61	0.59	0.64	0.02	3.29	0.60	-2.41
	E_u(GPa)	0.26	0.25	0.28	0.01	4.52	0.31	19.49
	E_k(GPa)	6.34	5.93	7.24	0.53	8.29	7.64	20.41
	Load(kN)	2.43	2.38	2.45	0.03	1.22	2.85	17.61
90^o – direction	σ_u(MPa)	268.33	250.88	276.39	10.38	3.87	319.04	18.90
	σ_k(MPa)	78.47	72.94	84.35	4.85	6.18	90.04	14.74
	ε_u(%)	2.24	2.12	2.31	0.07	3.32	2.53	13.04
	ε_k(%)	0.58	0.55	0.59	0.02	3.45	0.47	-17.65
	E_u(GPa)	11.48	11.16	11.82	0.29	2.56	13.22	15.16
	E_k(GPa)	14.08	13.50	14.68	0.49	3.48	16.61	17.96
	Load(kN)	9.17	8.82	9.45	0.23	2.54	10.82	18.08

Table 3.6. Experimental data vs. theoretical values for 16-ply biaxial laminates

Biaxial 16-plies $[0/90]_{4s}$								
Direction	Engineering Values	Experimental Statistics					Prediction	Difference (%)
		Avg.	Min	Max.	SD	CV (%)		
0^o – direction	σ_u(MPa)	331.86	326.37	335.19	3.50	1.06	389.96	17.51
	σ_k(MPa)	110.90	105.18	114.75	3.51	3.17	129.22	16.52
	ε_u(%)	2.09	2.03	2.14	0.04	1.98	2.58	23.70
	ε_k(%)	0.61	0.60	0.62	0.01	1.50	0.52	-15.58
	E_u(GPa)	15.31	14.72	15.82	0.49	3.18	17.63	15.17
	E_k(GPa)	19.57	18.53	20.67	0.84	4.28	22.79	16.48
	Load(kN)	21.96	21.69	22.33	0.30	1.36	25.87	17.83
45^o – direction	σ_u(MPa)	90.81	90.41	91.55	0.44	0.49	104.30	14.86
	σ_k(MPa)	34.38	33.04	35.09	0.79	2.30	40.84	18.76
	ε_u(%)	13.96	12.81	15.89	1.16	8.31	15.57	11.50
	ε_k(%)	0.59	0.58	0.60	0.01	1.30	0.53	-11.01
	E_u(GPa)	0.37	0.35	0.39	0.02	5.39	0.43	17.42
	E_k(GPa)	8.50	7.60	9.16	0.62	7.34	9.96	17.14
	Load(kN)	6.04	5.95	6.09	0.05	0.87	6.94	14.88
90^o – direction	σ_u(MPa)	362.86	356.79	371.81	5.90	1.63	416.73	14.85
	σ_k(MPa)	98.95	94.91	101.45	2.90	2.93	118.71	19.97
	ε_u(%)	2.83	2.73	2.97	0.10	3.62	2.56	-9.77
	ε_k(%)	0.61	0.59	0.62	0.01	2.41	0.41	-33.39
	E_u(GPa)	11.94	11.32	12.25	0.37	3.13	13.49	13.02
	E_k(GPa)	17.08	16.57	17.94	0.52	3.03	19.23	12.59
	Load(kN)	24.03	23.62	24.51	0.38	1.59	27.69	15.21

Table 3.7. Experimental data vs. theoretical values for 8-ply quadriaxial laminates

Quadriaxial 8-plies $[0/-45/+45/90]_s$								
Direction	Engineering Values	Experimental Statistics					Prediction	Difference (%)
		Avg.	Min	Max.	SD	CV (%)		
0^o – direction	σ_u(MPa)	246.10	233.37	255.93	10.37	4.21	283.58	15.23
	σ_k(MPa)	77.05	74.11	80.56	2.37	3.08	90.62	17.61
	ε_u(%)	2.54	2.35	2.80	0.18	7.05	2.58	1.62
	ε_k(%)	0.61	0.59	0.63	0.01	2.01	0.46	-24.93
	E_u(GPa)	9.56	9.20	9.89	0.30	3.18	11.55	20.78
	E_k(GPa)	13.26	12.77	13.61	0.34	2.57	16.03	20.85
	Load(kN)	7.74	7.39	7.95	0.24	3.10	8.93	15.35
45^o – direction	σ_u(MPa)	212.87	208.30	218.05	4.28	2.01	257.66	21.04
	σ_k(MPa)	67.95	63.69	70.92	2.93	4.32	81.00	19.20
	ε_u(%)	2.05	1.95	2.17	0.08	4.12	2.56	24.79
	ε_k(%)	0.52	0.51	0.53	0.01	1.46	0.47	-9.04
	E_u(GPa)	9.49	9.22	9.86	0.24	2.58	11.49	21.10
	E_k(GPa)	14.07	12.96	15.19	0.95	6.78	15.56	10.62
	Load(kN)	6.73	6.51	6.99	0.23	3.39	8.14	20.95
90^o – direction	σ_u(MPa)	230.49	218.77	243.83	9.75	4.23	269.25	16.82
	σ_k(MPa)	75.22	73.13	76.32	1.25	1.66	89.12	18.47
	ε_u(%)	2.16	2.03	2.39	0.15	6.89	2.56	18.48
	ε_k(%)	0.56	0.53	0.58	0.02	3.97	0.44	-21.67
	E_u(GPa)	9.84	9.36	10.33	0.41	4.18	11.50	16.78
	E_k(GPa)	13.86	13.10	14.66	0.62	4.44	16.12	16.28
	Load(kN)	7.32	6.87	7.81	0.34	4.67	8.56	16.93

Table 3.8. Experimental data vs. theoretical values for 16-ply quadriaxial laminates

Quadriaxial 16-plies $[0/-45/+45/90]_{2s}$								
Direction	Engineering Values	Experimental Statistics					Prediction	Difference (%)
		Avg.	Min	Max.	SD	CV (%)		
0^o – direction	σ_u(MPa)	253.41	236.84	268.96	13.42	5.29	299.86	18.33
	σ_k(MPa)	73.98	70.86	77.13	2.83	3.83	88.93	20.22
	ε_u(%)	2.43	2.14	2.70	0.22	9.12	2.58	6.43
	ε_k(%)	0.57	0.56	0.58	0.01	1.15	0.46	-19.65
	E_u(GPa)	9.79	9.60	9.95	0.13	1.31	11.08	13.16
	E_k(GPa)	13.68	13.35	14.16	0.42	3.04	15.82	15.63
	Load(kN)	15.26	14.19	16.11	0.83	5.41	18.06	18.36
45^o – direction	σ_u(MPa)	230.05	222.74	242.62	9.91	4.31	275.39	19.71
	σ_k(MPa)	72.78	69.97	74.57	1.85	2.54	88.84	22.06
	ε_u(%)	2.15	1.98	2.28	0.13	6.10	2.56	19.36
	ε_k(%)	0.55	0.54	0.56	0.01	1.88	0.47	-14.22
	E_u(GPa)	9.69	9.45	9.96	0.20	2.09	11.71	20.86
	E_k(GPa)	14.12	13.55	14.64	0.41	2.88	16.54	17.13
	Load(kN)	13.89	13.48	14.36	0.39	2.79	16.66	19.93
90^o – direction	σ_u(MPa)	270.29	257.68	283.30	9.81	3.63	317.18	17.35
	σ_k(MPa)	79.35	77.54	81.14	1.30	1.64	87.34	10.07
	ε_u(%)	2.38	2.37	2.40	0.01	0.58	2.57	7.72
	ε_k(%)	0.56	0.53	0.59	0.02	4.18	0.44	-21.23
	E_u(GPa)	10.90	10.27	11.23	0.39	3.55	12.72	16.71
	E_k(GPa)	15.05	14.22	15.82	0.60	4.00	17.61	16.99
	Load(kN)	16.24	15.45	16.97	0.64	3.92	19.01	17.06

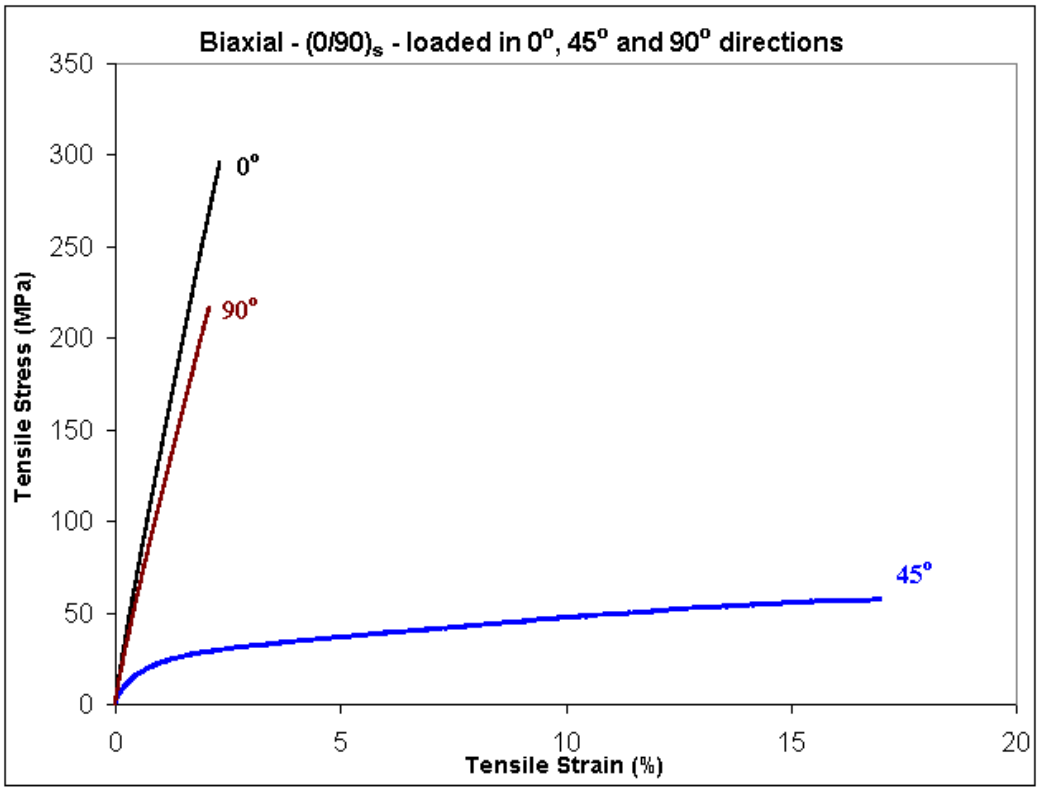

Figure 3.9. Typical stress-strain curves of biaxial $[0/90]_s$ laminates tested

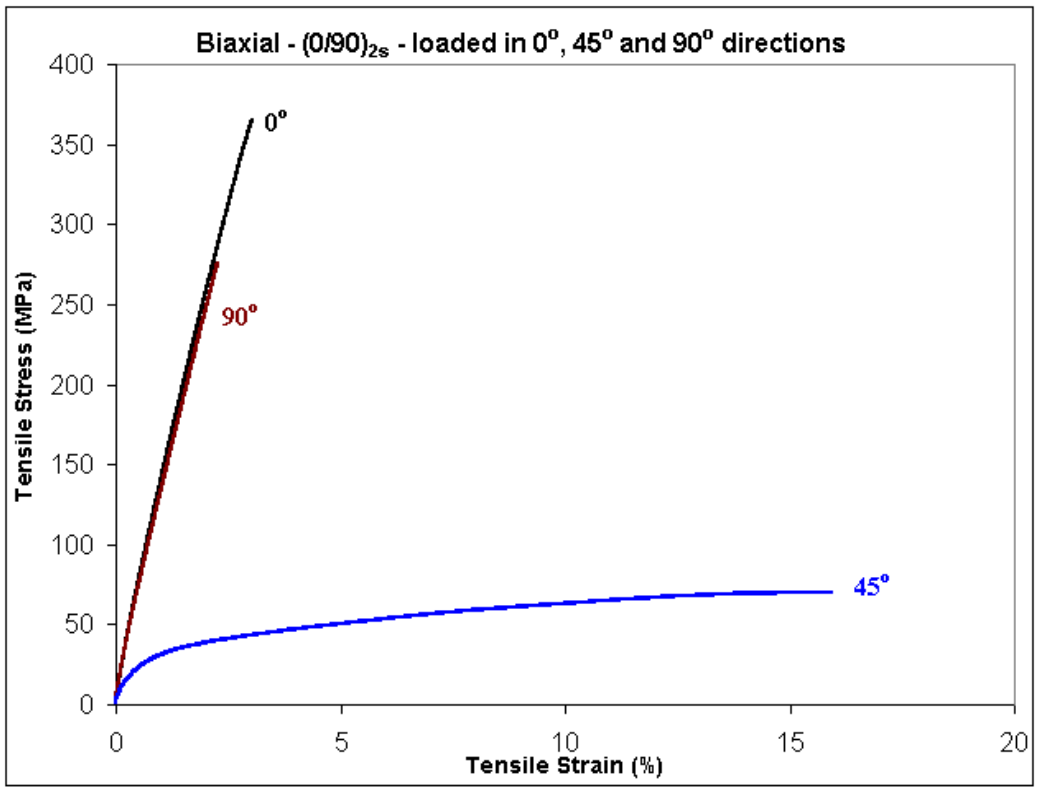

Figure 3.10. Typical stress-strain curves of biaxial $[0/90]_{2s}$ laminates tested

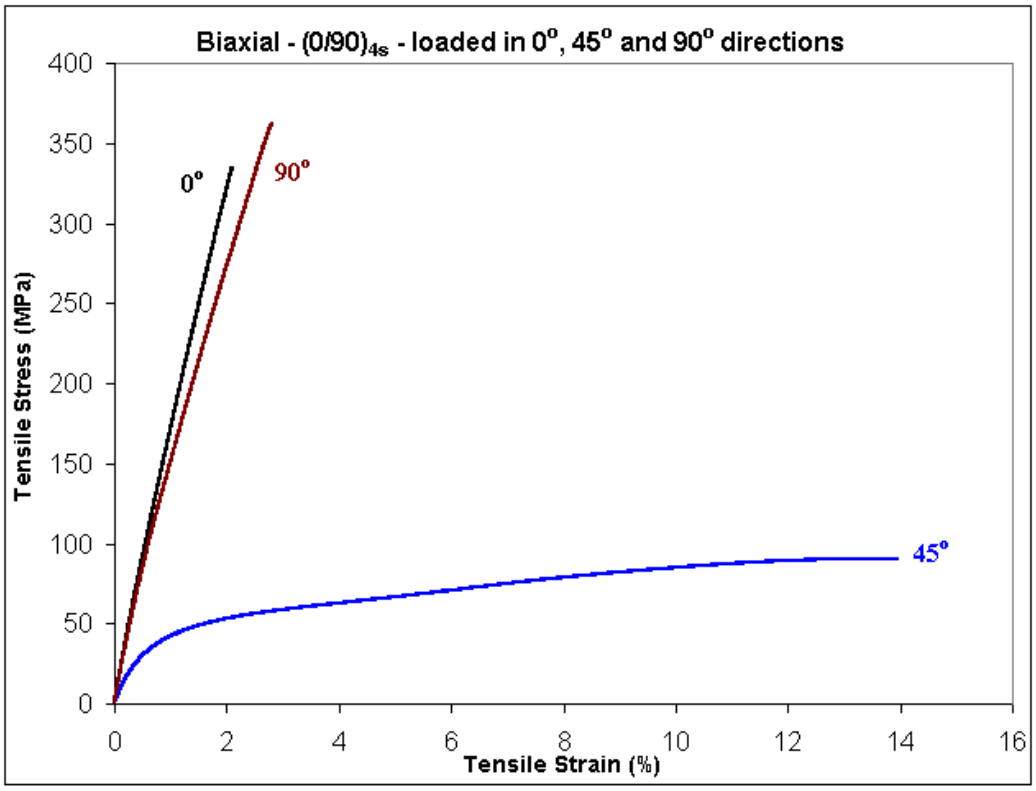

Figure 3.11. Typical stress-strain curves of biaxial $[0/90]_{4s}$ laminates tested

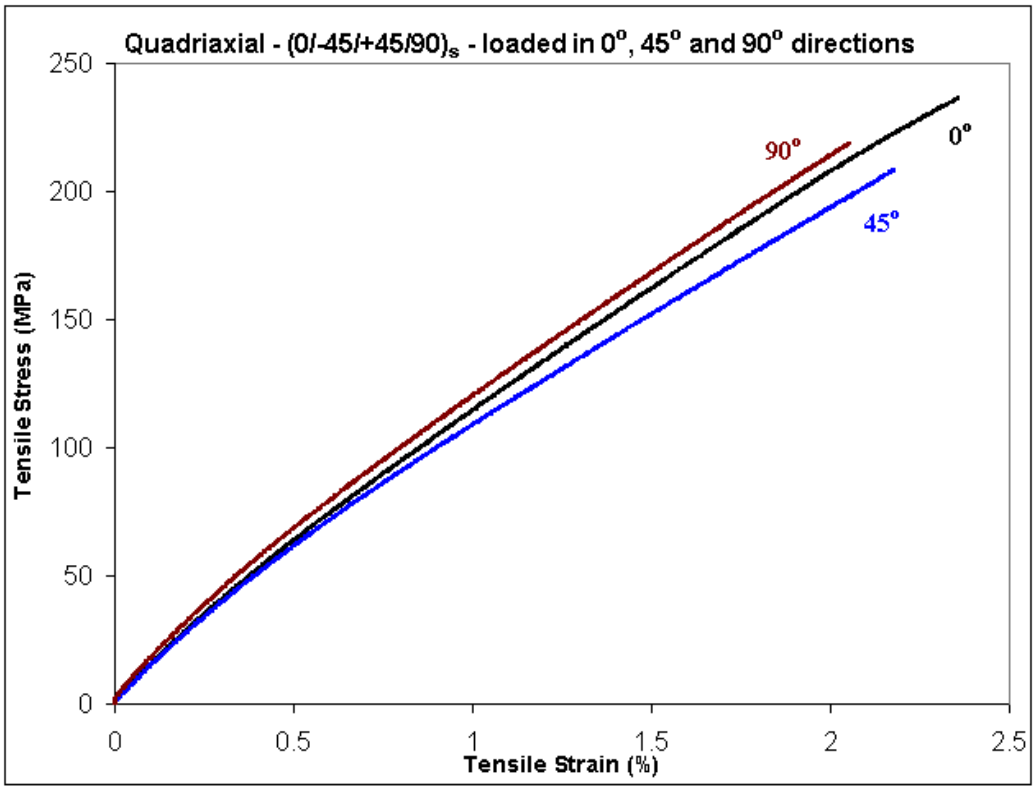

Figure 3.12. Typical stress-strain curves of quadriaxial $[0/-45/+45/90]_s$ laminates tested

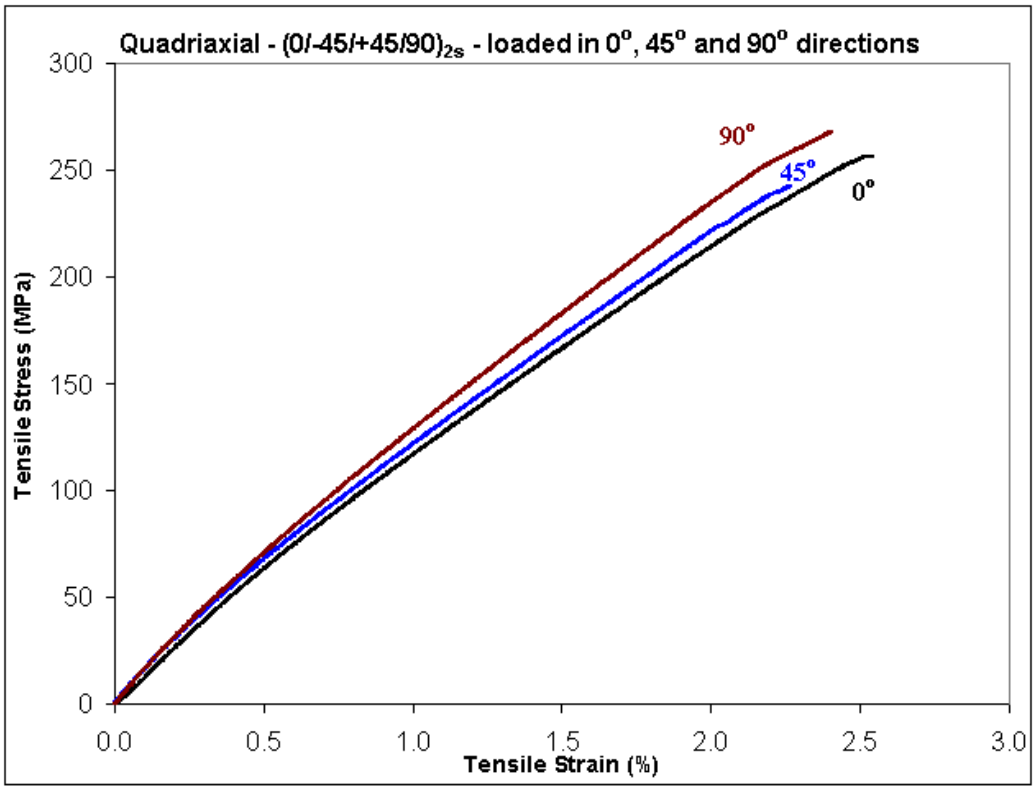

Figure 3.13. Typical stress-strain curves of quadriaxial $[0/-45/+45/90]_{2s}$ laminates tested

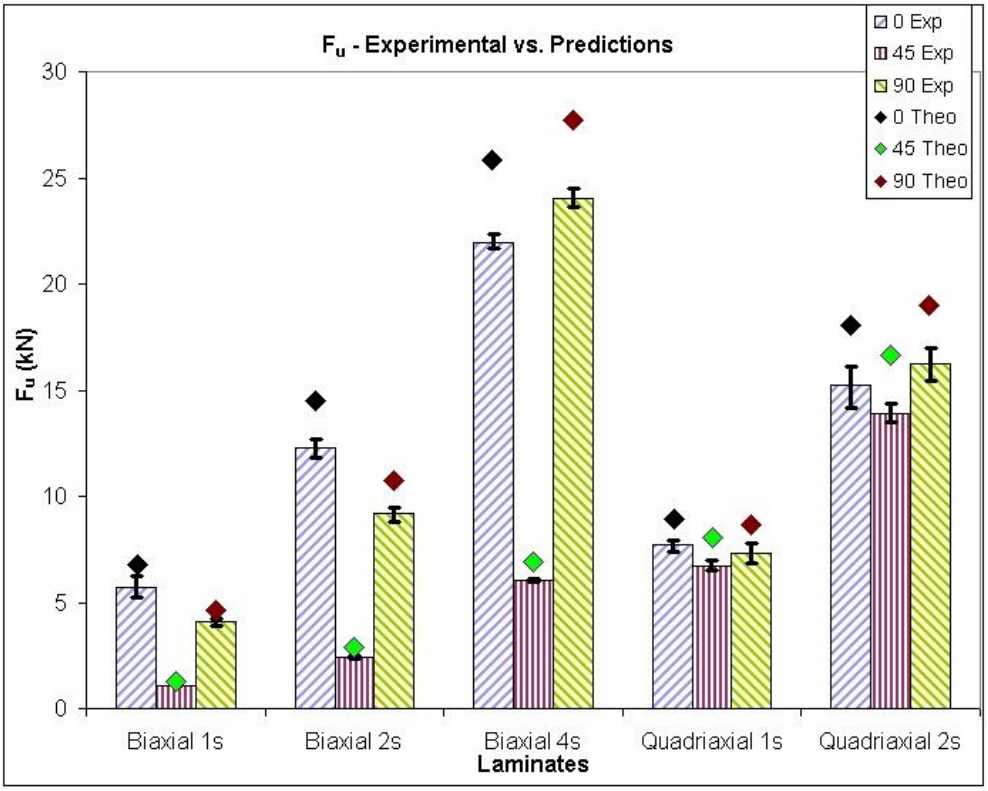

Figure 3.14. Experimental data vs. theoretical values for F_u

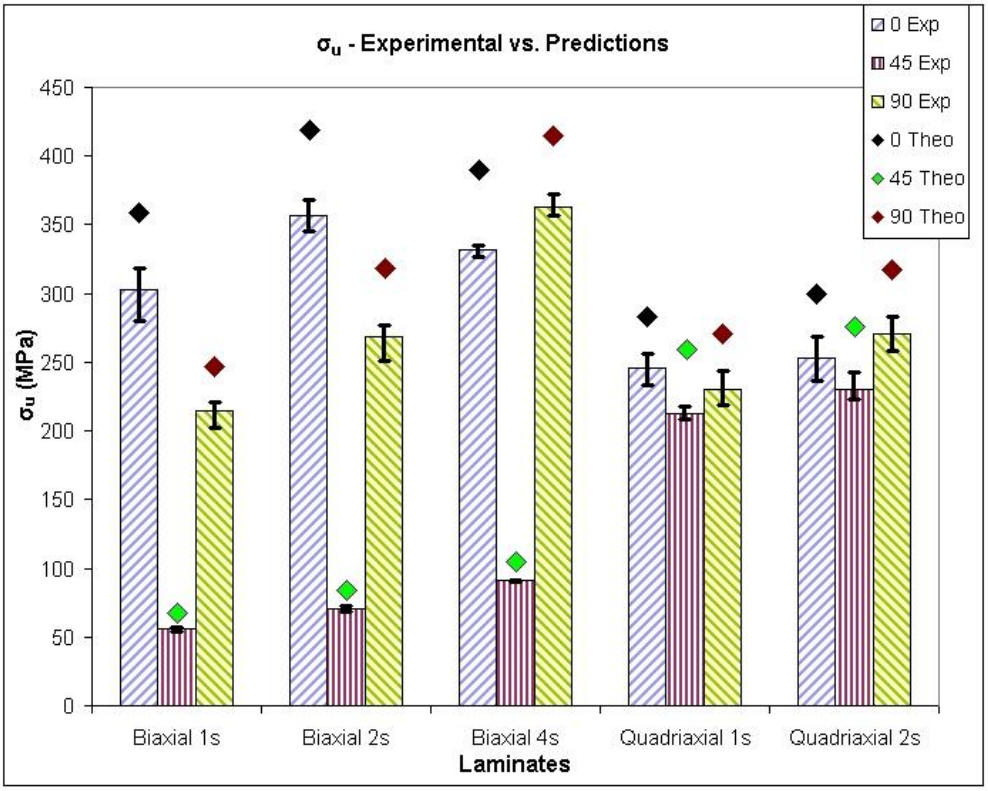

Figure 3.15. Experimental data vs. theoretical values for σ_u

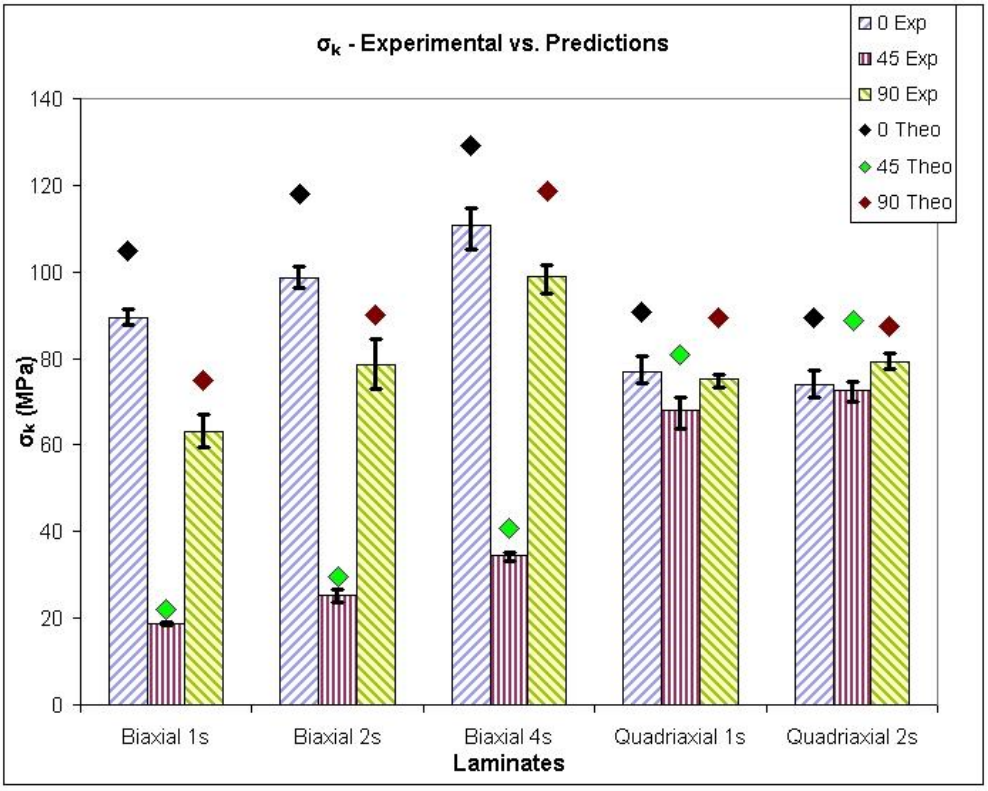

Figure 3.16. Experimental data vs. theoretical values for σ_k

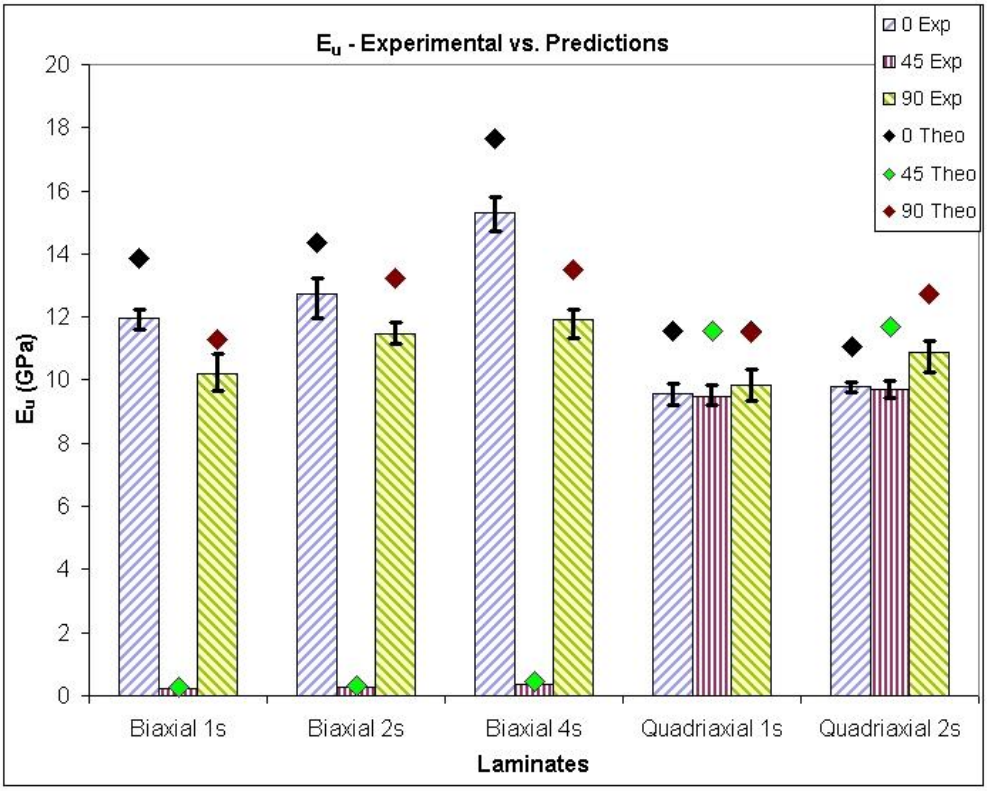

Figure 3.17. Experimental data vs. theoretical values for E_u

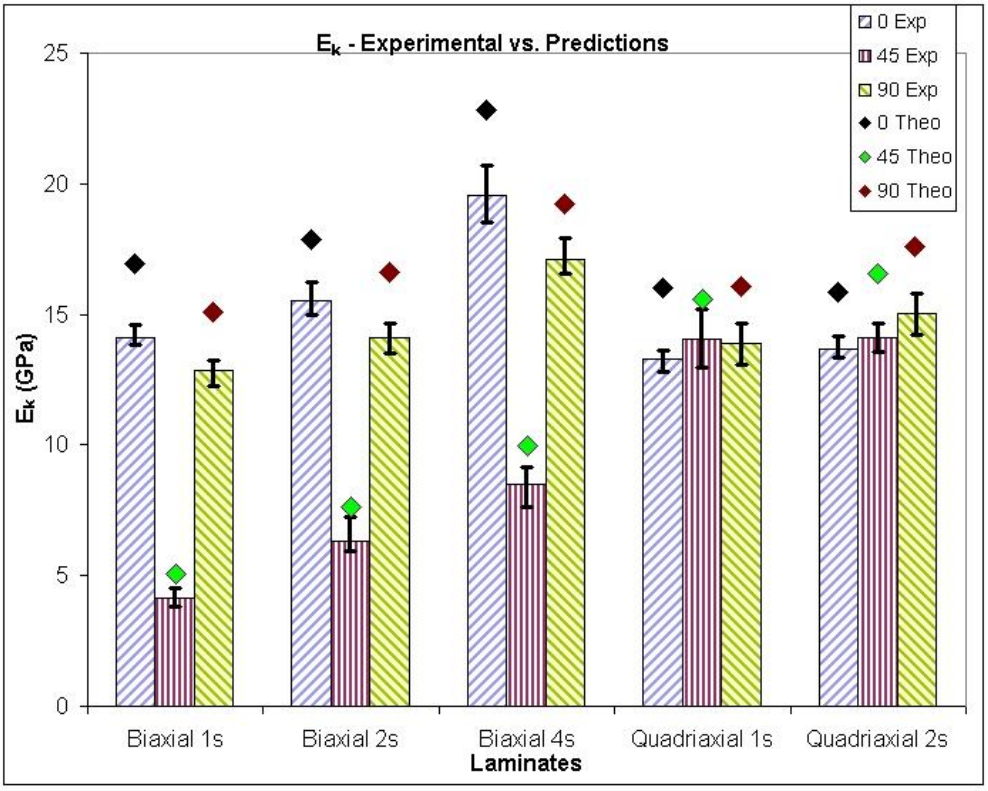

Figure 3.18. Experimental data vs. theoretical values for E_k

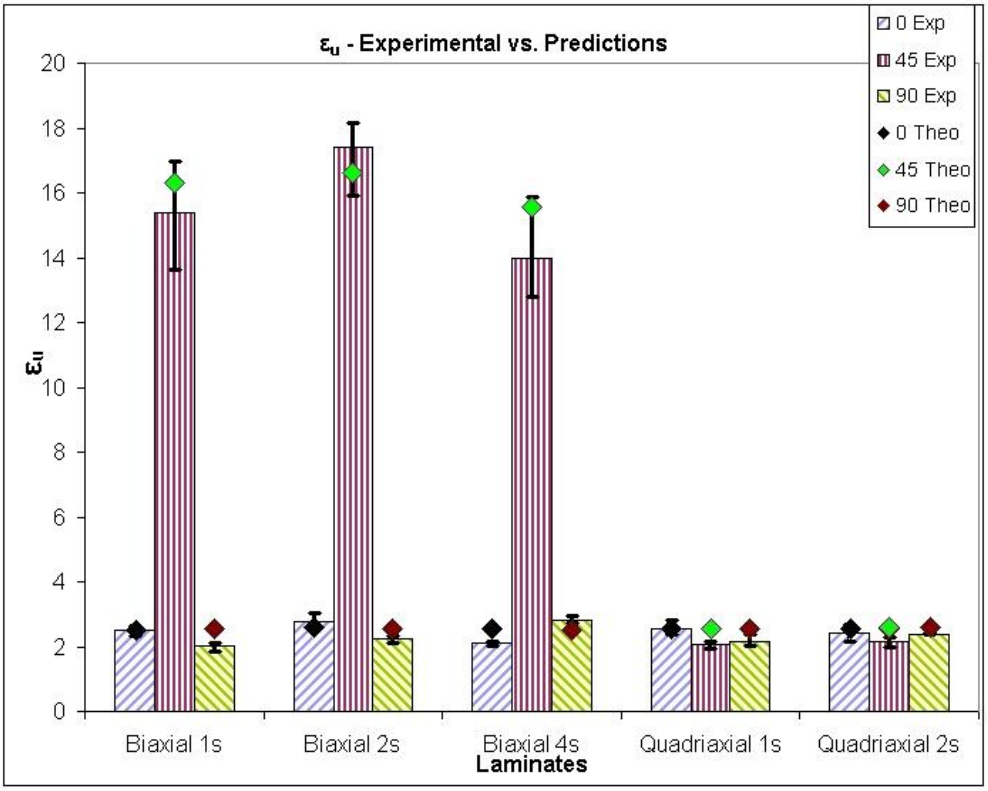

Figure 3.19. Experimental data vs. theoretical values for ε_u

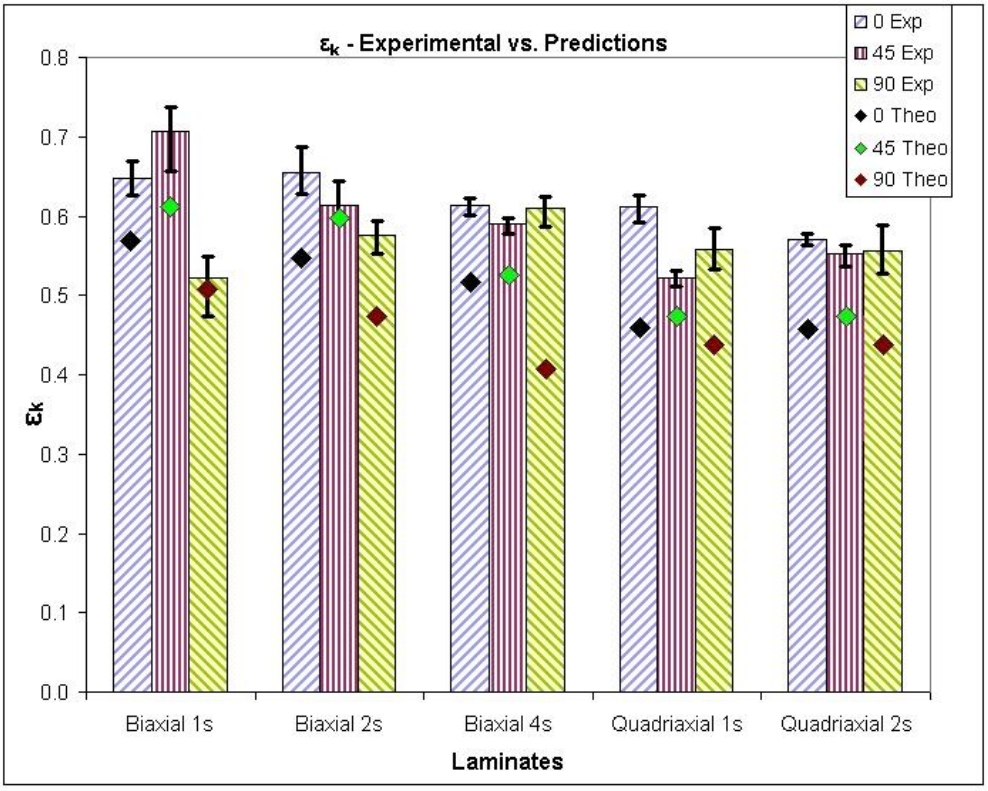

Figure 3.20. Experimental data vs. theoretical values for ε_k

3.7. Discussion of the Results

3.7.1. Experimental Results

Figure 3.9 to Figure 3.11 show that for all kind of biaxial laminates, regardless of whether cross-ply or angle-ply type, all the experimental values increase as the number of plies used, thus the laminate thickness, increases except for the σ_u, ε_u and ε_k of $[0/90]_{4s}$ loaded in 0^o direction and ε_u and ε_k of $[0/90]_{4s}$ loaded in 45^o direction where these values are less than those of their 2s case counterparts. 4s case (16-plies), when analyzed, has the highest V_v (9.02 per cent) of all three types of biaxial laminates (others 2s and 4s) which leads to stress concentration effects, thus resulting in lower strength and strains.

For all the biaxial cross-ply laminates, it is noticed that the knees in the stress-strain curves of 90^o loading cases are more pronounced than those of 0^o loading cases, i.e. E_k/E_u is smaller, which points out that once the transverse plies (90^o) are broken, their residues contribute less to the overall strength in 90^o loading cases than in 0^o loading cases.

In biaxial cross-ply laminates, as pointed out by Edgren *et al* [7], when longitudinal loads are applied, intralaminar (transverse) cracks are encountered in the 90^o fibers which propagate along the thickness direction in transverse fibers. Transverse cracking that cannot pass beyond the 0^o – 90^o interface when it comes across the interface, then results in the redistribution of the load and an increase in the stress on the longitudinal fibers. This imposition along with the increased tensile load causes delamination especially along the longitudinal fibers which eventually culminates in complete failure of the laminate in the form of fiber pull-out. The resulting damage is demonstrated in Figure 3.21, delaminations that take place are illustrated in Figure 3.22 [13] and fiber pull-out of the failed $[0/90]_s$ specimen tested in this work is shown in Figure 3.23.

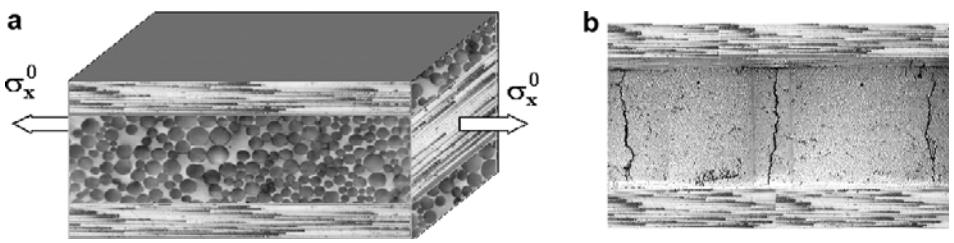

Figure 3.21. Cross-ply laminate (a) under uniaxial loading and (b) resulting damage [13]

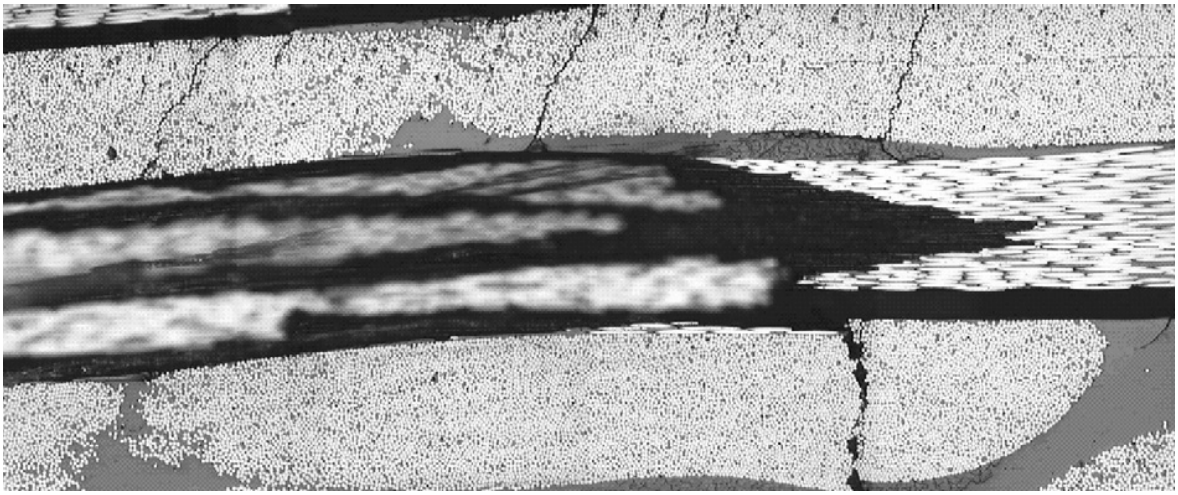

Figure 3.22. Micrograph of $[0/90]_{2s}$ composite showing extensive delaminations and failure of the 0^o bundles at high strains [13]

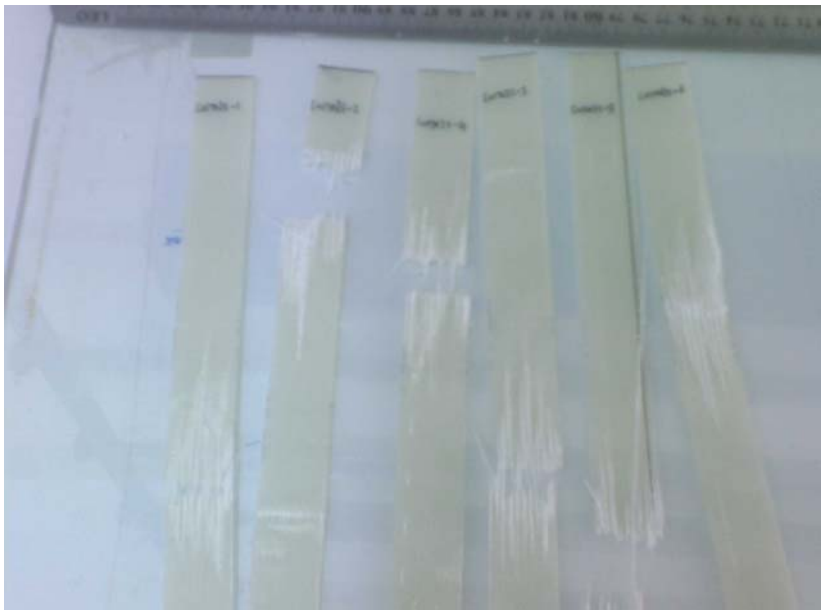

Figure 3.23. Fiber pull-out of the failed $[0/90]_s$ specimens

In biaxial angle-ply laminates, situation is far different and more complicated compared to that in cross-ply laminates. E_u is far less than E_k and ε_k is far less than ε_u this time. Also, angle-ply laminates bear loads lower than those of cross-ply laminates and during the tensile tests it was observed that it took much higher strain for them to fail than it took for the cross-ply laminates to fail.

This situation observed in tensile testing of angle-ply laminates concurs with findings of Rotem and Hashin [27] who worked on failure modes of angle-ply laminates. They

pointed out that the onset of failure in ±45^{o} laminates is not due to interlaminar shear, but to lamina cracking, starting just before the knee point. The specimen does not fail but continues to sustain the load. Cracking occurs progressively in various domains, criss-crossing the whole specimen. The number of cracks increases with continued elongation of the specimen. After a certain elongation, interlaminar yielding starts. This yielding causes bundles of fibers to move and change orientation with the stretching, and thus increases the applied load necessary to continue the elongation until complete failure occurs. Figure 3.24 shows $[\pm 45]_{4s}$ specimens failed after tensile tests where interlaminar yielding can be seen.

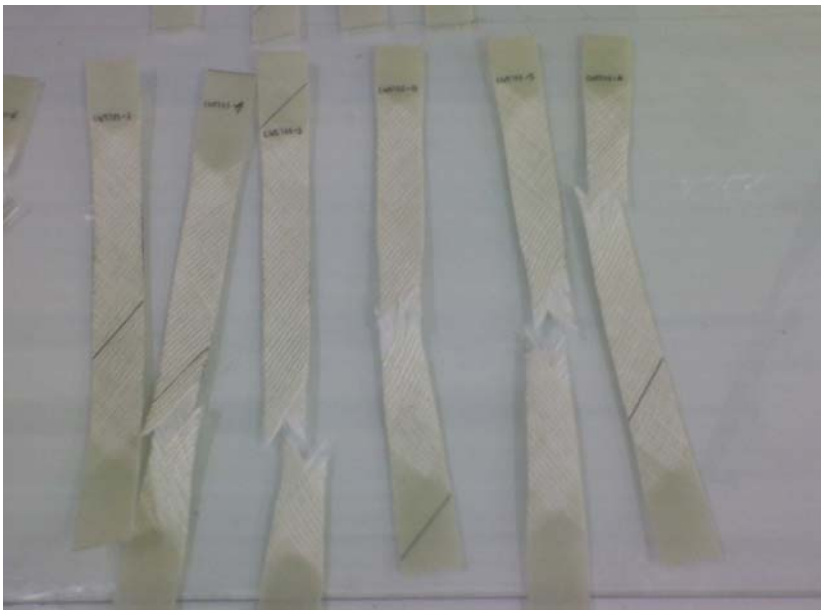

Figure 3.24. Failure of $[0/90]_{4s}$ specimens loaded in 45^{o} direction

Quadriaxial laminates yield almost the same experimental data (within 15 per cent at most) irrespective of the loading direction and number of plies (as shown in Figure 3.12 and Figure 3.13) which agrees with findings of Hogg *et al* [6]. Values of engineering stiffnesses, strains and strengths slightly increase as the number of plies increase and the load the laminates bear almost double as the number of plies are doubled.

Failure mode of the quadriaxial laminates resemble those of biaxial cross-ply laminates as presented in Figure 3.23. The stress-strain curves for quadriaxial laminates has two knees; the first one at the strain corresponding to failure of the 90^{o} plies and the second one at the strain corresponding to failure of the ±45^{o} plies. The knee for the ±45^{o} ply failure is more distinct than the one for the 90^{o} ply failure because the laminates have

twice as many ±45^o plies as it does 90^o plies. Ultimate laminate failure occurs at the longitudinal failure strain for the 0^o plies.

When scatters in the ultimate tensile strengths obtained from tensile tests of both biaxial and quadriaxial laminates are analyzed as listed in Table 3.4 through Table 3.8, it is noticed that coefficient of variation (CV) of σ_u is between 1 per cent to 5.5 per cent. Taking into consideration the findings of Oya and Hamada [28] who observed in their studies that in longitudinal tensile testing of pre-preg type fiber reinforced composites, CV for ultimate tensile strength is usually around 3.0 per cent to 11 per cent and in their transverse tensile testing, CV varies from 5 per cent 35 per cent, it can be concluded that scatters in NCF composites are quiet comparable with and generally lower than in pre-preg composites.

3.7.2. Theoretical Predictions

As it can be seen in Figure 3.14 to Figure 3.18, when calculated values of biaxial cross-ply and angle-ply and quadriaxial laminates are analyzed, predicted strength, stiffness and ultimate load values are around 15 to 20 per cent higher than their experimental counterparts where it is observed that the gap between the predictions and experimental data does not depend on the number of plies of laminates.

On the other hand, strain values has high variation in the range from -25 per cent to 25 per cent for all three kind of laminates as shown in Figure 3.19 and Figure 3.20. This might indicate that for strain predictions of biaxial cross-ply and angle-ply and quadriaxial laminates, there might be an extra factor that is some measure of thickness that needs to be taken into consideration.

The key parameters that define the gap between theoretical values and experimental values are voids, fiber waviness, stitching of the bundles, knitting yarns, misalignment and damage induced in the fibers during manufacturing.

Voids arise from two main causes: firstly, incomplete wetting out of the fibers by the resin; this results in entrapment of air and is more likely in systems where the dry fibers are closely spaced and the viscosity of the resin is high; secondly the volatiles produced during

the cure cycle in thermosetting resins and during the melt processing operations in thermoplastic polymers [3]. Voids deteriorate the strength of composite materials by reducing the effective amount of fibers and causing stress concentrations. Figure 3.25 presents a micrograph of $[0/+45/90/-45]_{2s}$ specimen showing voids.

Fiber waviness leads to local bending stresses which then cause imperfections in the longitudinal fibers and delaminations in the $0^o - 90^o$ interface [13]. Waviness is forced to straighten in tension, thus it contributes less to the weakening of the laminate properties in tension than in compression or flexure. In their studies, Tessitore and Riccio [29] found out that for $[0/90]_s$ the exclusion of the fiber waviness can lead to an error in the tension stiffness prediction of about 4.8 per cent with respect to experimental results.

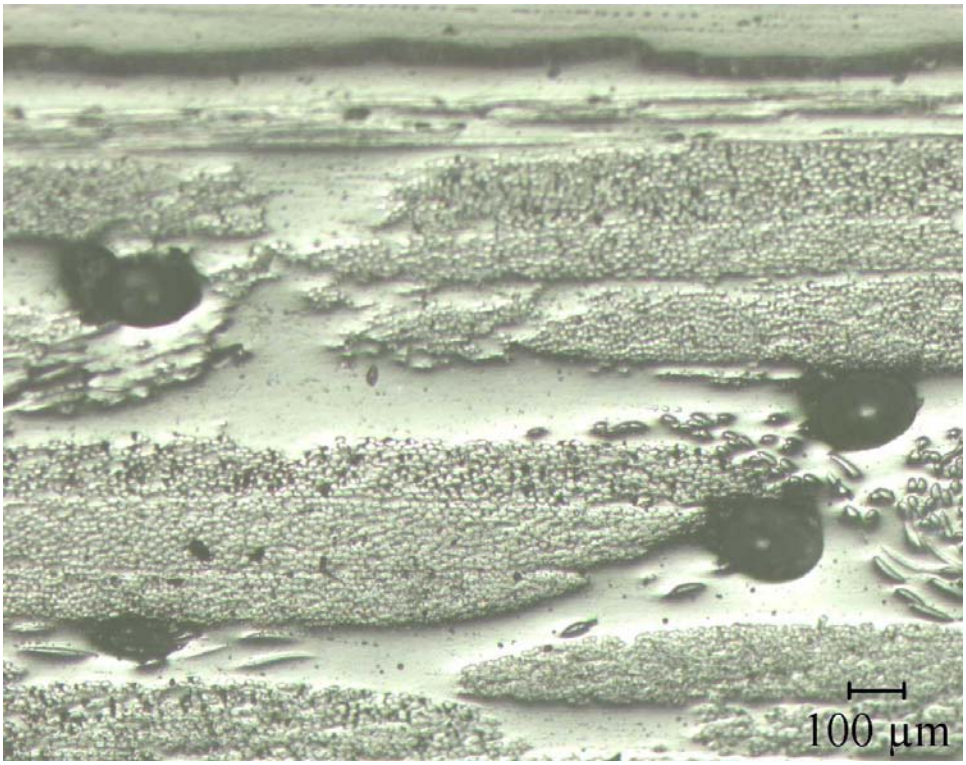

Figure 3.25. Micrograph of $[0/+45/-45/90]_{2s}$ specimen

The introduction of stitching has strong drawbacks as it induces heterogeneity at the scale of the tows. Imperfections are introduced such as resin pockets forming between tows or fiber breakage induced by the penetration of needles into the tows [9]. For NCF composites with plies of the perform formed as a continuous layer of parallel fibers, piercing a fibrous ply by a needle and forming of the stitching loop results in a certain

disturbance of the uniform and parallel placement of the fibers. More precisely, the stitching causes deviations of the fibers in a ply from their uniform direction. These deviations produce fiber-free resin-rich zones near the stitching locations which may cause stress concentration and cracks initiation [30]. For $[0/90]_s$, the lack of stitching leads to a 1.9 per cent error in prediction of the tension stiffness [29]. Figure 3.26 shows local crimping and buckling caused by the insertion of a stitch through a tow in a biaxial non-crimp fabric [31].

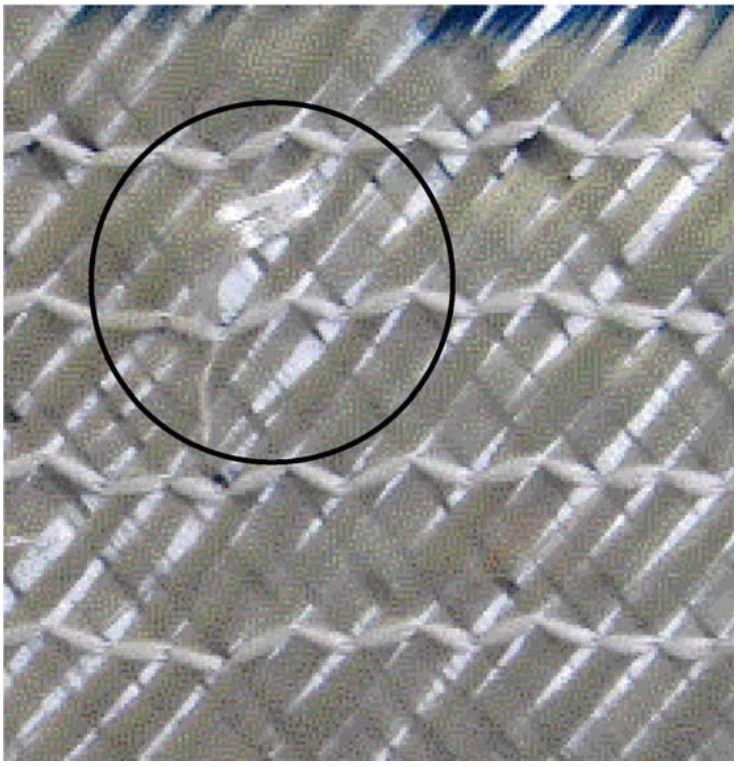

Figure 3.26. Local crimping and buckling caused by the insertion of a stitch through a tow in a biaxial non-crimp fabric [31]

Although knitting yarns usually make up 1 per cent of the total weight in fibers, when laying up multi-axial NCF fabrics, the stitching yarns at the fabric surface create gaps between the layers consisting of several stitched plies. These cause resin-rich regions in the composites, affecting their mechanical performance [30]. The amount of crimp present in the fiber yarns, although increases the integrity of the fabric, can cause a reduction of the in-plane material properties and can induce dangerous failure mechanisms such as delaminations and kink-band formations.

Misalignment and damage induced in the fibers during both manufacturing of the fiber performs and laminate production is also another key parameter that creates local stress concentrations where the damage is present. Dexter and Hasko [32] studied tensile strengths of NCF laminates and pre-preg laminates, observed that average tensile strengths of NCF laminates are 20 per cent lower than their pre-preg counterparts and commented that this difference is due to fiber misalignment and damage to the fiber tows.

3.8. Reliability Factor

In calculation of the reliability factor for fiberglass – polyester resin composites produced in this work, firstly the difference between experimental value and predicted value of ultimate tensile strength for each lamina is found. Then, average and standard deviation of these differences are calculated, the differences are graphed to get their distribution and finally reliability factor for multiples of standard deviation are calculated. Figure 3.27 shows the graph of the calculated reliability and Table 3.9 lists the reliabilities that correspond to the multiples of standard deviation.

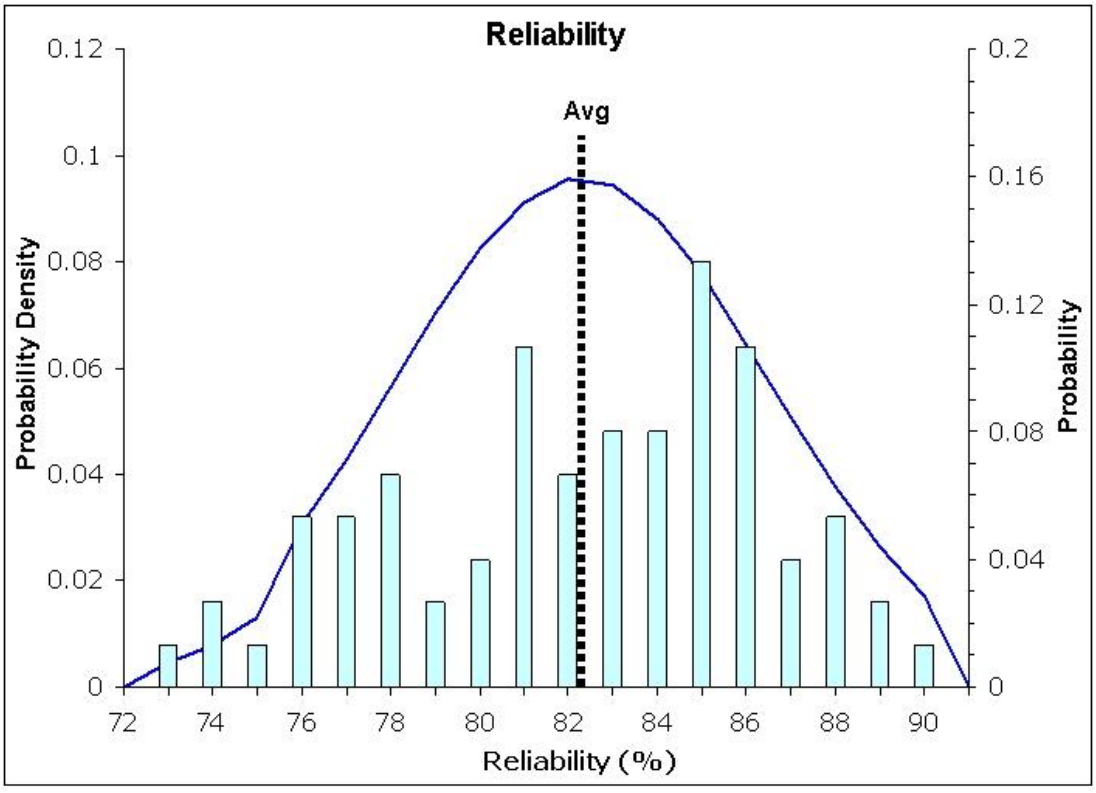

Figure 3.27. Reliability graph

Table 3.9. Reliabilities corresponding to multiples of standard deviation

Accuracy	Reliability (%)
Average	82.3
Average - SD	78.1
Average - 2*SD	74
Average - 3*SD	69.8

4. CONCLUSIONS AND FUTURE WORK

In this study, mechanical properties of non-crimp fabric (NCF) fiberglass reinforced composite materials are investigated. For this intent, tensile testing of laminates made of NCF E-glass fiber reinforced polyester resin is carried out where the vacuum infusion process (VIP) is used as the manufacturing technique.

As a result of the laminate manufacturing process, 4-ply, 8-ply and 16-ply cross-ply and angle-ply biaxial laminates and 8-ply, 16-ply quadriaxial laminates are produced. Fiber, matrix and void volume fractions of the laminates are determined by making use of ASTM D3171 Standard. Results show that 16-ply biaxial laminates has the highest void content (around 9 per cent) of all biaxial laminates where fiber volume fractions of biaxial laminates are around 40 per cent and both type of quadriaxial laminates have nearly the same amount of fiber (around 47 percent) and void content (6 per cent).

5 specimens for each stacking sequence are tested during tension experiments as per ISO 527-5 by making use of Instron 8801 servohydraulic testing machine which overall total up to testing of 75 specimens (5 specimens x 5 type of laminates x 3 stacking sequences) -not taking into account those, if any, which were spoiled during the test and then disposed of- and the resulting data for each tests are recorded by using computer software. Engineering values σ_u, ε_u, E_k and failure load are automatically given by the software and σ_k, ε_k and E_u are calculated using linear regression analysis on the results.

Theoretical predictions of these engineering constants are obtained by making use of Halpin - Tsai method, classical lamination theory (CLT), micromechanics models for laminated composite materials, maximum strain criterion, first ply failure prediction and the ply discount model.

When calculated values of biaxial cross-ply and angle-ply and quadriaxial laminates are analyzed, predicted strength and stiffness values are around 15 to 20 per cent higher than their experimental counterparts where it is observed that the gap between the predictions and experimental data does not depend on the number of plies of laminates.

On the other hand, strain values has high variation in the range from -25 per cent to 25 per cent for all three kind of laminates. This might indicate that for strain predictions of biaxial cross-ply and angle-ply and quadriaxial laminates, there might be an extra factor that is some measure of thickness that needs to be taken into consideration.

One significant point on the quadriaxial laminates is that they behave in a quasi-isotropic manner as expected which means they have the same in-plane stiffnesses, strengths and strains along any direction.

When scatters in the ultimate tensile strengths obtained from tensile tests of both biaxial and quadriaxial laminates are analyzed, it is noticed that coefficient of variation (CV) of σ_u is between 1 per cent to 5.5 per cent. Taking into consideration that coefficient of variation (CV) in pre-preg type fiber reinforced composites can vary between 3.0 per cent to 35 per cent it can be concluded that scatters in NCF composites are quiet comparable with and generally lower than in pre-preg composites.

The loss in accuracy and the discrepancies between the theoretically predicted values and the experimentally obtained results are attributed to voids, fiber waviness, stitching of the bundles, knitting yarns, misalignment and damage induced in the fibers during manufacturing.

A general reliability factor for fiberglass – polyester resin composite materials is also aimed to be obtained. In this respect, both experimental results and predicted values of ultimate tensile strengths are used. Average reliability factor is found to be 82.3 per cent.

For future work, different types of fibers (carbon, organic or mixed) and resin materials (epoxy) might be used. Besides, stacking sequences can also be differentiated to give distinct laminates such as antisymmetric laminates, e.g., $[0/90/45]_2$ or $[0/45]_3$ to cover a wider variety of possibilities. Additionally, stitching and knitting yarn effects might also be taken into account in theoretical predictions to yield more accurate results.

REFERENCES

1. Gibson R.F., *Principles of Composite Materials Mechanics*, McGraw- Hill, Inc., Singapore, 1994.

2. Jones R.M., *Mechanics of Composite Materials*, Taylor & Francis, Philadelphia, 1999.

3. Hull D., *An Introduction to Composite Materials*, Cambridge University Press, New York, 1981.

4. Matsson D., "*Mechanical Performance of NCF Composites*", PhD Thesis, Luleå University of Technology, 2005.

5. Johnson, A. F., *Engineering Design Properties of GRP*, British Plastics Federation, London, 1979.

6. Hogg P. J., A. Ahmadnia and F. J. Guild, "The Mechanical Properties of Non-crimped Fabric-based Composites", *Composites*, 24(5), pp. 423-432, 1993

7. Edgren F., D. Mattsson, L. E. Asp and J. Varna, "Formation of Damage and Its Effects On Non-crimp Fabric Reinforced Composites Loaded In Tension", *Composites Science and Technology*, 64, pp. 675–692, 2004.

8. Bibo G. A., P. J. Hogg and M. Kemp, "Mechanical Characterisation of Glass- and Carbon-fibre Reinforced Composites Made With Non-crimp Fabrics", *Composites Science and Technology*, 57, pp. 1221-1241, 1997.

9. Drapier M., M. R. Wisnom, "Finite-element investigation of the compressive strength of non-crimp-fabric-based composites", *Composites Science and Technology,* 59*,* pp. 1287-1297, 1999.

10. Drapier M., M. R. Wisnom, “A Finite-element Investigation of the Interlaminar Shear Behaviour of Non-crimp-fabric-based Composites”, *Composites Science and Technology*, 59, pp. 2351-2362, 1999.

11. Wang Y., J. Li and P. B. Do, “Properties of Composite Laminates Reinforced with E-Glass Multiaxial Non-Crimp Fabrics", *Journal of Composite Materials*, 29, pp. 2317-2333, 1995.

12. Wang Y., “Mechanical Properties of Stitched Multiaxial Fabric Reinforced Composites From Mannual Layup Process”, *Applied Composite Materials,* 9, pp. 81–97, 2002.

13. Mattsson D., R. Joffe and J. Varna, “Damage in NCF composites under tension: Effect of layer stacking sequence”, *Engineering Fracture Mechanics,* 75, pp. 2666–2682, 2008.

14. METYX Composites Company – Reinforcements Technical Datasheets.

15. Scott Bader – Crystic 703PA Technical Datasheet.

16. Larsen E. B., “Pressure Bag Molding: Manufacturing, Mechanical Testing, Non-Destructive Evaluation, and Analysis”, SAND2006-7855P, 2007.

17. Akzo Nobel – Butanox M60 Technical Datasheet.

18. Ragondet A., “Experimental Characterisation of the Vacuum Infusion Process”, PhD Thesis, University of Nothingham, 2005.

19. Correiaa N.C., F. Robitaillea, A.C. Longa, C.D. Rudda, P. Simacek and S.G. Advani, “Analysis of the vacuum infusion moulding process: I. Analytical formulation”, *Composites: Part A*, 35 pp. 1645–1656, 2005.

20. Vacuum Infusion - The Equipment and Process of Resin Infusion, http://www.fibreglast.com/documents/361.pdf, accessed on 15/08/2009.

21. ISO 527-5 Plastics – Determination of Tensile Properties – Test Conditions For Unidirectional Fibre-reinforced Plastic Composites.

22. ASTM D 3039/D 3039M Standard Test Method for Tensile Properties of Polymer Matrix Composite Materials.

23. ASTM D 3171 Standard Test Methods for Constituent Content of Composite Materials.

24. Mechanical Properties of Selected Engineering Materials, http://ocw.mit.edu/NR/rdonlyres/Materials-Science-and-Engineering/3-11Mechanics-of-MaterialsFall1999/Modules/props.pdf , accessed on 07/11/2009.

25. Malvar L.J., "Unidirectional Core-Shell Hybrids For Concrete Reinforcement – A Preliminary Study", Office of Naval Research, February 1994.

26. Hult J, F.G. Rammerstorfer, "*Engineering Mechanics of Fibre Reinforced Polymers and Composite Structures*, Springer-Verlag, Udine, 1994.

27. Rotem A., Z. Hashin, "Failure Modes of Angle Ply Laminates", *Journal of Composite Materials*, Vol.9 pp.191-206, 1975.

28. Oya N., H. Hamada, "Mechanical properties and failure mechanisms of carbon fibre reinforced thermoplastic laminates", *Composites: Part A* 28A pp. 823-832, 1997.

29. Tessitore N., A. Riccio,"A novel FEM Model For Biaxial Non-crimp Fabric Composite Materials Under Tension", *Computers and Structures* 84 pp. 1200–1207, 2006.

30. Mikhaluk D.S., T.C. Truong, A.I. Borovkov, S.V. Lomov and I. Verpoest, ”Experimental Observations and Finite Element Modelling of Damage Initiation and Evolution in Carbon/Epoxy Non-crimp Fabric Composites”, *Engineering Fracture Mechanics,* 75, pp. 2751–2766, 2008.

31. Kong H., A.P. Mouritz and R. Paton, “Tensile Extension Properties and Deformation Mechanisms of Multiaxial Non-crimp Fabrics”, *Composite Structures*, 66, pp. 249–259, 2004.

32. Dexter H.B., G.H. Hasko, “Mechanical Properties and Damage Tolerance of Multiaxial Warp-Knit Composites”, *Composites Science and Technology* 56, pp. 367-380, 1996.